Czech Technical University in Prague
Faculty of Nuclear Sciences and Physical Engineering

DOCTORAL THESIS

Measurement of top quark polarization in top-antitop lepton+jets final states at DØ

Prague 2016

Kamil Augsten

Bibliographic Entry

Author:
Ing. Kamil Augsten
Czech Technical University in Prague
Faculty of Nuclear Sciences and Physical Engineering
Department of Dosimetry and Application of Ionizing Radiation

Title of Dissertation:
Measurement of top quark polarization in top-antitop lepton+jets final states at DØ

Degree Programme:
Application of Natural Sciences

Field of Study:
Nuclear Engineering

Supervisor:
prof. RNDr. Vladislav Šimák, DrSc.
Czech Technical University in Prague
Faculty of Nuclear Sciences and Physical Engineering
Department of Mathematic

Academic Year:
2015/2016

Number of Pages:
128

Keywords:
top quark, polarization, Standard Model

Bibliografický záznam

Autor:
Ing. Kamil Augsten
České vysoké učení technické v Praze
Fakulta jaderná a fyzikálně inženýrská
Katedra dozimetrie a aplikace ionizujícího záření

Název práce:
Měření polarizace top kvarku v top-antitop lepton+jets konečném stavu na DØ

Studijní program:
Aplikace přírodních věd

Studijní obor:
Jaderné inženýrství

Zaměření:
prof. RNDr. Vladislav Šimák, DrSc.
České vysoké učení technické v Praze
Fakulta jaderná a fyzikálně inženýrská
Katedra matematiky

Akademický rok:
2015/2016

Počet stran:
128

Klíčová slova:
top kvark, polarizace, Standard Model

Acknowledgements

I would like to dedicate this thesis to my daughter Sofie Ella, she was born somewhere between Chapters 3 and 4 and she was so kind to let me finish my work. Being with her, when I was not writing, was a wonderful time. My infinite gratitude belong to my wife Zuzana for all her support during my graduate career. Without you I would be lost in the world.

I would like to thank my supervisor prof. Šimák for introducing me to the world of particle physics and to the top quark. I am most grateful for the opportunity to work on this measurement and for the possibility of joining the DØ experiment.

I would like to thank all the people I have met in the DØ collaboration, especially the Czech group - Zdeněk, Petr, Jirka, Saša. You have been good friends and colleagues to me, very helpful with everything. It was fun to hang out in the Dog House. I would like to thank all the people involved in the DØ top quark group, Andy, Slava, and Boris to name a few.

I would also like to thank all my colleagues and friends at the Department of Dosimetry and Application of Ionizing Radiation. You are the best co-workers and you made the department a second home for me.

Last but not least, I would like to thank my parents and my family for supporting me all my life and for trying to understand what it is I have been doing.

Declaration

I hereby declare that I worked on this thesis on my own and I used only the sources which are listed in the Bibliography. All co-authors have agreed to included the results of our co-operation.

Kamil Augsten

In Prague, September 2016

Abstract

This thesis presents a measurement of the top quark polarization in the $t\bar{t}$ events produced in $p\bar{p}$ collisions at $\sqrt{s} = 1.96$ TeV using data corresponding to $9.7\,\mathrm{fb}^{-1}$ of integrated luminosity collected with the DØ detector at the Fermilab Tevatron Collider. The final states used in the measurement contain one lepton and at least three jets. The polarization is measured using the angular distribution of leptons along three different axes: the beam axis, the helicity axis, and the transverse axis normal to the $t\bar{t}$ production plane. This is the first measurement of top quark polarization at the Tevatron Collider in lepton+jets final states, and the first measurement of transverse polarization in $t\bar{t}$ production. The polarization along the beam axis is combined with the previous result in the dilepton final states by the DØ experiment. The observed distributions are consistent with the Standard Model of nearly no polarization and no indication for beyond Standard Model physics is observed. The measurement offers legacy result from unique Tevatron Collider data and provides more information about the top quark production and decays, about the properties of the heaviest elementary particle.

Abstrakt

Tato dizertace popisuje měření polarizace top kvarku v produkci párů top-antitop pocházejích z $p\bar{p}$ srážek na urychlovači Tevatron ve Fermilabu. Analyzovaná data z detektoru DØ odpovídají integrované luminositě $9.7\,\mathrm{fb}^{-1}$ a měření se provádí v koncových stavech s jedním leptonem a alespoň třemi jety. Polarizace se studuje v úhlovém rozložení leptonů vzhledem ke třem různým osám: ose svazku protonů, ose helicitní a ose kolmé k produkční rovině párů top-antitop. Jedná se o první měření polarizace top kvarku na urychlovači Tevatron v koncových stavech s jedním lepton a jety a vůbec první měření polarizace vzhledem k ose kolmé k produkční rovině. Výsledek polarizace vzhledem k ose svazku protonů je zkombinován s předchozím výsledek z experimentu DØ v koncových stavech se dvěma leptony. Pozorované rozdělení a naměřené polarizace jsou v souladu s předpovědí ze Standardního modelu, tedy s téměř nulovou polarizací párů top kvarků. Neobjevil se žádný náznak nové fyziky mimo Standardní model. Výsledky měření jsou konečná z unikátních dat z urychlovače Tevatron, který svoji činnost ukončil v roce 2011. Význam tohoto měření je poskytnout více informací o vlastnostech, produkci a rozpadu top kvarku, nejtěžší známé elementární částice.

Contents

Foreword 1

1 Introduction 3

1.1 Standard Model 6
1.2 Top Quark 9
1.2.1 Top Quark Production . . . 10
1.2.2 Top Quark Decay 11
1.3 Author notes 15

2 Experimental Apparatus 17

2.1 Tevatron Collider 17
2.2 DØ Detector 20
2.2.1 Coordinate System 21
2.2.2 Tracking System 23
2.2.3 Calorimeter 25
2.2.4 Muon System 29
2.2.5 Luminosity Monitor 31
2.2.6 Trigger System 32
2.3 Author notes 34

3 Object Reconstruction and Identification 35

3.1 Tracks 35
3.2 Vertex Reconstruction 36
3.3 Electrons 37
3.4 Muons 39
3.5 Imbalance in Transverse Momentum 41
3.6 Jets 42
3.6.1 Jet Reconstruction 42
3.6.2 Jet Identification 43
3.6.3 Identification of b quark jets 44
3.7 Jet Energy Calibration 46
3.7.1 Flavor Dependent Correction 51
3.8 Author notes 57

4 Data, Simulations, and Selection 59

4.1 Data 59
4.2 Monte Carlo Simulations 61
4.2.1 Signal modeling 62
4.2.2 Physics background 62
4.2.3 Instrumental background . 63
4.2.4 Beyond Standard Model processes 64
4.3 Selection 64
4.4 Author notes 66

5 Measurement of Top Quark Polarization 67

5.1 Top Quark Polarization 67
5.2 Previous Measurements 69
5.3 Measurement 70
5.3.1 $t\bar{t}$ Reconstruction 71
5.3.2 Sample Composition 72
5.3.3 Correction to W+jets Background 78
5.3.4 Template Fit 82
5.3.5 Verification of the Method 84
5.4 Systematic Uncertainties 89
5.5 Author Notes 94

6 Results 97

6.1 Combination with Dilepton Measurement 98
6.2 Final Results 99
6.3 Author Notes 99

7 Conclusion 103

Bibliography 105

A Control Plots 113

B Journal Paper 119

Figures

1.1 Feynman diagrams for top quark pair production at the Tevatron. 11
1.2 Feynman diagrams of single top quark production at the Tevatron. 12
1.3 Final states signatures for the $t\bar{t}$ pairs. 14
1.4 Feynman diagram for the top quark pair decay to the lepton+jets final state. 14

2.1 The Fermilab accelerator complex. 18
2.2 Tevatron Run II integrated luminosity. 21
2.3 Cut view of the upgraded DØ detector. 22
2.4 Cross-sectional view of the central tracking system. 23
2.5 Schematic view of the DØ central tracking system. . . . 24
2.6 Photo of the DØ SMT barrel. 25
2.7 The arrangement of the DØ Silicon Microstrip Tracker. . 25
2.8 The arrangement of the layers in DØ Central Fiber Tracker. 26
2.9 Schematic view of the DØ Liquid Argon Calorimeter. . . 27
2.10 Cross section of one quarter of the calorimeter. 28
2.11 Schematic diagram of individual calorimeter cell. 28
2.12 Schematic view of the DØ muon drift tube system. . . . 30
2.13 Schematic view of the DØ muon scintillation system. . 30
2.14 Schematic view of the left part of the DØ muon system. 31
2.15 Schematic drawing of the DØ luminosity monitors. 32
2.16 Overview of the DØ trigger system. 33

3.1 BDT method output of the electron identification. 40
3.2 The jet evolution in the DØ detector. 44
3.3 The efficiency for selecting a b jet and the light jet misidentification in the MVA_{bl}. 46
3.4 Illustration of MPF correction in γ+jet events at the particle level and detector level [62]. . . . 49
3.5 The absolute response of the calorimeter as a function of E'. 50
3.6 Jet energy scale corrections for jets with $R_{\mathrm{cone}} = 0.5$. 52
3.7 Jet energy scale corrections for jets with $R_{\mathrm{cone}} = 0.7$. 52
3.8 Number of particles in particle jets produced by quarks or gluons in γ+jet MC samples. 54
3.9 Single pion responses in DØ detector from Run IIb MC. 55
3.10 Ratio between the reconstructed jet energy and the jet energy calculated from the MC single particle responses. 56
3.11 Tuning of single particle responses in data and MC. 57
3.12 The Flavor Dependent Correction factor F_{corr}. 58

4.1 The integrated luminosity for Run II of the DØ experiment. . 60

5.1 Control distributions of input variables for the e+3 jets kinematic discriminant. 75
5.2 Control distributions of input variables for the μ+3 jets kinematic discriminant. 76
5.3 Control distributions of input variables for the $e+\geq 4$ jets kinematic discriminant. 77

5.4 Control distributions of input variables for the $\mu+ \geq 4$ jets kinematic discriminant. 78
5.5 The e+jets likelihood discriminant distributions. 79
5.6 The μ+jets likelihood discriminant distributions. 80
5.7 Corrections to the W+jets background in the e+jets control sample with 3 jets and 0 b-tagged jets. 82
5.8 Corrections to the W+jets background in the μ+jets control sample with 3 jets and 0 b-tagged jets. 83
5.9 The ℓ+jets $\cos\theta$ distributions for data, expected backgrounds, and signal templates. 85
5.10 The pseudo-experiments with five 1,000 ensembles for different top quark polarization. 86
5.11 Closure test for the template method to measure polarization along the beam axis. 89
5.12 Closure test for the template method to measure polarization along the helicity axis. 90
5.13 Transverse momentum of the $t\bar{t}$ pair. 93

6.1 Two dimensional visualization of the longitudinal top quark polarizations in the ℓ+jets final state. 101

A.1 Distributions of input variables the likelihood discriminant in the $e + 3$ jets channel. 114
A.2 Distributions of input variables the likelihood discriminant in the $e+ \geq 4$ jets channel. 115
A.3 Distributions of input variables the likelihood discriminant in the $e+ \geq 4$ jets channel. 116
A.4 The likelihood discriminant distributions in the $e + 3$ jets and $\mu + 3$jets channels 117
A.5 The likelihood discriminant distributions in the $e+ \geq 4$ jets and $\mu+ \geq 4$ jets channels 118

Tables

1.1 The elementary particles and force carriers in SM. 7
1.2 The SM fermions, gauge bosons, and Higgs boson and their basic properties. 8

4.1 Integrated luminosities for data with data quality requirements using un-prescaled triggers. 61

5.1 Overview of previous results for the top quark polarization along beam axis. 69
5.2 Overview of previous results for the top quark polarization along helicity axis. 70
5.3 The sample composition scale factors. 81
5.4 Sample composition and event yields. 81
5.5 The pseudo-experiment results for polarization along helicity axis. 87
5.6 The pseudo-experiment results for polarization along beam axis. 87
5.7 The pseudo-experiment results for polarization along transverse axis. 87
5.8 Parameters of the generated BSM models. 88
5.9 Comparison of generated and measured values of the polarization along beam axis. . . 88
5.10 Comparison of generated and measured values of the polarization along helicity axis. . 91
5.11 Uncertainties in the top quark polarization measurement along the three axes. 95

6.1 Measured top quark polarizations according to the lepton flavor. 97
6.2 Measured top quark polarizations according to the lepton charge. 98
6.3 Measured top quark polarizations according to the number of hets. 98
6.4 Uncertainties and correlations for the combination of top quark polarization along beam axis. . . 99
6.5 Measured top quark polarizations along the beam, helicity, and transverse axes. . . 100

Foreword

This thesis describes analysis of the DØ data, an effort in conjunction with the entire DØ collaboration. I did not build the DØ detector, nor did I create all the algorithms and methods necessary for the identification, reconstruction and analysis of the data recorded by the DØ detector. I participated in data acquisition by taking shifts in the control room, in the correction of the reconstructed jets as a part of the Jet Energy Scale group, and in the Top quark group in the selection of the lepton+jets final states and in the measurement of the top quark mass and polarization.

In total, I have been the main author, or one of the main authors, of six DØ Notes that are internal DØ documents describing techniques and analyses in various parts of the DØ framework and physics program. Three of them are about the Sample Dependent Correction that is an important part of the Jet Energy Scale. This was my main service task at the experiment. One of the notes describes the selection of the top quark decay channel called lepton+jets, which is essential for the measurement of top quark polarization as the analysis was done in this particular channel. The last two notes describe the measurement of the top quark polarization itself, the first is the Analysis Note, a detailed description of the measurement for the collaboration, and the second is the Conference Note that describes the measurement in form of a short paper for the first public revelation of the results.

The results have been presented at 2015 and 2016 International Workshop on Top Quark Physics [102] with Proceedings in Ref. [18].

I have been also recognized as one of the main authors of three DØ papers: Jet energy scale determination in the D0 experiment [64], Precision measurement of the top-quark mass in lepton+jets final states [40], and Measurement of top quark polarization in $t\bar{t}$ lepton+jets final states [84].

The original work of the author is described in the Section 3.7.1 and in the Chapters 5 and 6.

Chapter 1

Introduction

In the field of particle physics, we seek answers to the questions how world around us works, on what principles the Universe is based, and what things looked like in the early times just after the Big Bang. This is based on the belief that we can describe it by understanding the fundamental pieces and how their interactions work. This is the way the Standard Model of particle physics (SM) is built and how we recognize the elementary particles and their interactions. SM has become a very powerful and successful theory. It will be briefly described in Section 1.1. Experimental physicists use many expensive tools, like enormous particle accelerators and large detectors, and spend decades to bring this theory to trial. As scientists we have to cross-check everything to discover the world of elementary particles step by step, to see how the interactions work and how matter around us is built.

This thesis is focused on one of the elementary particles known as the top quark. This particle is very popular in the particle physics community and not only because the name top quark sounds eminently (one can imagine an analogy to pop-culture names as Top Gun, Top Gear etc.), but mainly because of its unique properties that allow us not only to test the SM theory, but also to have a possibility to see processes that are not described by this theory. On March 2nd, 1995, the discovery of the top quark was officially announced by the CDF and the DØ collaborations at the Fermi National Accelerator Laboratory (Fermilab), USA [1, 2]. This date sets it as one of the most recent discoveries in particle physics, prior to the well-known discoveries of Higgs boson in the year 2012 [3] and tau neutrino in the year 2000 [4]. Both the experimental and theory physicists have spent those 21 years since the top quark discovery extremely productively and there are thousands of journal papers and books written on topics related to the top quark and its properties.

Top quark, or rather the third generation of quarks, was predicted in 1973 [5] and the hunt for the top quark discovery was over 20 years long. This is due to the fact that top quark is very heavy and its mass is a free parameter in SM. The top quark is the heaviest elementary particle currently known to us, with mass of approximately 190 protons, which can be compared to an atom of Tungsten[1]. Note

[1]Some authors refer top quark to nuclei of Gold, although Tungsten is more accurate. This is perhaps due to the possibility of comparison between the price of gold and the price for the

that each proton is composed of three quarks, two up quarks and one down quark, that belong to the first generation of quarks.

Measurements involving top quarks have been extremely difficult in the first decade after the discovery. And still are, although we now know many top quark properties and parameters with great precision. But at the time when the top quark was discovered, there was only one place where we could 'observe' the top quark - it was the Tevatron Collider, where both experiments, the CDF and the DØ, were based.

In the beginning, only few candidate events for the top quark production and decay were detected by both detectors. For example, the observation paper by the DØ collaboration [1] stated only 17 events, while 3.8 events was the expected background, and measured the basic parameters like mass and cross-section with huge uncertainties of 15% and 34%, respectively. Many more top quarks have been observed since then, but the important date was the year 2009, when the Large Hadron Collider (LHC) has started its operation. LHC might be called the top quark factory, as the number of top quarks produced is very large compared to the Tevatron collider. For an experimental physicist it was also a unique possibility how to confirm results from the Tevatron collider as LHC is the only other place where we are able to produce top quarks and observe them using detectors built around the collision points.

Many properties and parameters of the top quark have been measured with great precision. Many people and resources have been devoted because of the uniqueness of top quark among elementary particles, for example the fact that top quark decay for hadronization and as the only quark does not form bound states [2]. Top quark is in the spot light for many experimental and theory physicists. Many studies performed in the past confirmed the SM predictions made about top quark, which is a great success for the theory. Some parameters are free in the theory, but are important to be measured because of the interplay with other processes and particles, like the Higgs boson. Such measurements are great trials for our understanding of data from the detectors and for our analyzing techniques that some might call looking for a needle in a haystack. And all the results are an important input for work of many theoretical physicists interested in the top quark sector.

This thesis describes the measurement of one of the top quark properties, the top quark polarization. In the case of the top quark decay, the polarization is carried by the decay products and therefore, we are able to measure the top quark polarization by looking at the angular distribution of the final decay products. Such measurement was interesting for the theory even before the top quark was discovered [6, 7, 8, 9]. The top quark polarization in the top quark pairs ($t\bar{t}$) is predicted in SM to be zero or

discovery of top quark, calculated as the mass of produced top quarks versus the price to build the accelerator and the detectors in gold.

[2]The $t\bar{t}$ bound state would be called toponium. This hypothetical meson formed from a top quark and its antiquark was initially the object looked for in the hunt for the discovery of top quark as all the other quarks have been observed in bound states. Toponium was never confirmed.

more precisely nearly zero as small polarization is generated by the parity-violating weak interactions [10], while many processes beyond the Standard Model associated with top quark production and decay induce a finite top quark polarization. On the other hand, it was clear that such measurement, to be feasible, needs large statistics and precise reconstruction of the top quark decay from the detected final state particles. The interest in this measurement started to be eminent when the so-called top quark forward-backward asymmetry results were published by both Tevatron experiments, DØ and CDF [11, 12], showing quite strong disagreement with SM calculations. The first measurement of the top quark polarization was however carried by the LHC experiments - both CMS and ATLAS showed agreement with the SM with first results in 2013 [13, 14]. The year after, the forward-backward asymmetry disagreement was resolved by better theory calculation at the next-to-next-to leading order (NNLO) and by a new measurement with the full Tevatron dataset. Still, the measurement of the top quark polarization from the Tevatron was missing and there was strong motivation for it [15, 16]:

- It is a missing piece that is important for the Standard Model confirmation or beyond Standard Model searches in the top quark sector.
- The initial state is different to the LHC and polarizations along some quantization axes from the $p\overline{p}$ collisions are expected to be larger than those for pp collisions [9, 10], therefore offering greater sensitivity than the LHC.
- Top quark polarization was never measured before at the Tevatron and most likely, there will be no other $p\overline{p}$ collider in the future, thus it is a legacy measurement with unique data.

As of now, there has been already one measurement of the top quark polarization at the Tevatron, it was a simultaneous measurement of the forward-backward asymmetry and the top quark polarization in dilepton final states by the DØ, published in 2015 [17]. The same year, results from measurement described in this thesis were made public at the TOP2015 workshop [18] and in the form of Conference Note [19].

This thesis is the first measurement of the top quark polarization in lepton+jets final states at the Tevatron, the first measurement of the transverse polarization in $t\bar{t}$ production and the combination with the dilepton result for the top quark polarization along the beam axis. The transverse polarization and the different quantization axes are defined in the Section 5.1.

This thesis is organized as follows. In this introductory chapter, Section 1.1 describes the Standard Model and Section 1.2 speaks about top quark physics. Following Chapter 2 provides the description of the experimental apparatus, that is the Tevatron accelerator and the DØ detector. In the Chapter 3, the object identification and Jet Energy Scale are discussed. The data and simulation samples, together with selection requirements are described in the Chapter 4. In the next Chapter 5, main part of this thesis, the measurement techniques for the top quark

polarization are described. The final results are presented in the Chapter 6 and the conclusion and short discussion is in the Chapter 7. Additional materials are attached as Appendix: Control plots in Section A and the journal paper B that is the output of this measurement.

1.1 Standard Model

In the current state of our understanding, the Standard Model of particle physics describes the interactions between particles. It has been extremely successful at modeling these interactions from low energies of a few electronvolts (eV) up to the highest energies that have been probed by experiments, several TeV (LHC is designed for 14 TeV). However, despite its success, there are some missing pieces. The gravitational interaction is not considered. While the SM very precisely describes the interactions of matter and antimatter, the vast majority of the universe consists of dark matter and dark energy not contained in the SM. Therefore, we consider SM to be an effective theory, well describing phenomena below a certain energy threshold. For the present high-energy physics experiments, the effect of standard gravity is negligible and we have been using the SM successfully over the years and trialing the theory by performing measurements.

The SM evolved during the 20th century as we started to discover microcosm and the world of particles around us. The important part of the history were 1950's and 1960's, when many physicists were confused by "particle zoo" with dozens of hadrons being discovered with no possibility of easy and systematical cataloging. The Quantum Electrodynamics (QED) had been a very strong theory by that time and the Quantum Chromodynamics (QCD) was built as an analogy to it using its the extension towards the non-abelian theories (Yang-Mills) providing theoretical background for the SM. Important factor was also deep inelastic scattering as experiments at SLAC showed there is proton structure. The SM is a very successful theory confirmed by many measurements and with all particles predicted being now confirmed by experiments, including the Higgs boson. The importance is in reducing the number of elementary particles (as compared to the situation in the early 1960's) and in identification of basic dynamical principles of interactions in the microcosm.

According to the SM, all matter consists of elementary particles, twelve fermions, each of which has an antimatter equivalent[3]. There are two types of fermions: quarks and leptons. The twelve fermions are arranged into three families as shown in Table 1.1. The quarks and leptons are grouped in three generations and particles in the same generation have relatively similar mass and related quantum properties. The particles in the first generation rarely decay and all ordinary matter is comprised of such particles. On the other hand, the particles in the higher generations are

[3]Antimatter equivalents are antiparticles and are denoted by placing bars above the particle symbols.

unstable, can only be produced at very high energies, and eventually decay into particles made out of the first generation (or belonging to the first generation).

	Fermions			Bosons
Leptons	$\begin{pmatrix} e \\ \nu_e \end{pmatrix}$	$\begin{pmatrix} \mu \\ \nu_\mu \end{pmatrix}$	$\begin{pmatrix} \tau \\ \nu_\tau \end{pmatrix}$	$\gamma, W^{\pm}, Z,$
Quarks	$\begin{pmatrix} u \\ d \end{pmatrix}$	$\begin{pmatrix} s \\ c \end{pmatrix}$	$\begin{pmatrix} b \\ t \end{pmatrix}$	g, H

Table 1.1: The elementary particles and force carriers in SM.

Among the leptons (ℓ), the lightest and most familiar is the electron (e), while more massive muon (μ) and tau leptons (τ) represent the second and third generation, respectively. The charged leptons interact via the electromagnetic and weak forces. The neutral leptons are called neutrinos, and are expected to be massless in the SM, but experimental results show they have small but finite mass [20]. Neutrinos interact only via the weak force, and are therefore hard to detect. For high-energy experiments, such as DØ, they are completely invisible in the detector and their presence is denoted by an imbalance in the transverse momentum in a measured event.

Quarks interact via electromagnetic, weak, and strong interactions. In addition to fractional electric charges, quarks carry QCD "color charges" of the strong interaction. Unlike leptons, quarks other than the top quark do not exist as free particles, but are always bound to one another, forming color-neutral particles (hadrons).

The basic properties of leptons, quarks, and bosons in the SM are summarized in Table 1.2

The complete set of interactions of the Standard Model particles is described by the gauge group

$$\mathrm{SU}_C(3) \otimes \mathrm{SU}_L(2) \otimes \mathrm{U}_Y(1), \tag{1.1}$$

which are the gauge groups of color, weak isospin, and weak hypercharge, respectively.

Electromagnetic interactions are mediated by the photon exchange between particles with electric charges. It acts on particles carrying weak hypercharge. The interaction corresponds to the $\mathrm{U}_Y(1)$ symmetry of quantum electrodynamics (QED).

The weak interactions are carried by charged $W^{\pm}$ and neutral Z^0 bosons and they act on all quarks and leptons. This is described by the $\mathrm{SU}_L(2)$ group and acts on particles carrying weak isospin. The fact that W and Z bosons are very massive is reflected in the very short range of these interactions. At high energies, above the W mass, the SM effectively unites the electromagnetic and weak interactions into electroweak (EW) force. The electroweak symmetry $\mathrm{SU}_L(2) \otimes \mathrm{U}_Y(1)$ is broken, which results in very different masses for the mediating photon and the W and Z

	symbol	name	mass	charge (e)
Leptons (spin = 1/2)	e	electron	0.510998928 MeV	-1
	ν_e	electron neutrino	< 2 eV	0
	μ	muon	105.6583715 MeV	-1
	ν_μ	muon neutrino	< 2 eV	0
	τ	tau	1776.86 MeV	-1
	ν_τ	tau neutrino	< 2 eV	0
Quarks (spin = 1/2)	u	up	2.3 MeV	$-1/3$
	d	down	4.8 MeV	$2/3$
	s	strange	95 MeV	$-1/3$
	c	charm	1.275 GeV	$2/3$
	b	bottom	4.18 GeV	$-1/3$
	t	top	173.21 GeV	$2/3$
Gauge bosons (spin = 1)	γ	photon	0	0
	$W^\pm$	W	80.385 GeV	± 1
	Z	Z	91.1876 GeV	0
	g	gluon	0	0
Higgs boson (spin = 0)	H	Higgs	125.09 GeV	0

Table 1.2: The SM fermions, gauge bosons, and Higgs boson and their basic properties, given without uncertainties, quoted from Ref. [21]. The electric charge is given in units of the charge of the electron.

bosons, and which is accommodated by the Higgs mechanism [22, 23] in which the presence of non-zero vaccum value of the Higgs field breaks the EW symmetry. The Higgs boson that corresponds to an excitation of the Higgs field is the last particle that has been discovered [3] and thus all the particles predicted in the SM have been observed in experiments.

Additionally for the quarks, the weak force provides the only mechanism for transitions from one family to another. With six quark flavors, the mixing between the different families is governed by a 3×3 unitary matrix V_{ij}, known as Cabibbo-Kobayashi-Maskawa (CKM) matrix [5]

$$V_{\mathrm{CKM}} = \begin{pmatrix} V_{ud} & V_{us} & V_{ub} \\ V_{cd} & V_{cs} & V_{cd} \\ V_{td} & V_{ts} & V_{tb} \end{pmatrix} . \tag{1.2}$$

As for any 3×3 matrix, we can define three Euler angles and one phase angle, and the latter introduces the possibility of the simultaneous violation of Charge Conjugation and Parity conservation (CP-violation) in EW processes. The values are either measured directly from particle decays, or obtained assuming the unitarity of the matrix and the latest oveview can be found in [21].

The strong interaction is mediated by gluons that couple to color charged particles

(quarks and gluons), and is described by an $SU_C(3)$ symmetry group. Unlike quarks, gluons bi-color combination of color and anti-color charges, and are postulated to belong to an octet of states from combination of three colors and three anticolors. Strong force is the strongest of the fundamental interactions and the strength increases as the distance of the interacting objects increases. As color is not a physically observable quality, any quarks or gluons produced in high energy collisions transform to color-neutral hadrons, i.e. hadronize, as the final states evolves in time. Experimentally, when a quark or gluon is produced in a collision, it will generate a shower of hadrons, called jet, that can be detected with the color quantum number of the final state identical to that of the initial colliding objects.

QCD processes cannot be calculated exactly, but approximation techniques based on perturbation theory are available, in which an asymptotic series can be given in terms of the coupling strength of the interaction. The coupling strength of the strong interaction, denoted as α_S, decreases with increasing transverse momentum of the elementary collision. Therefore for the high-energy hadron colliders and top qaurk physics, perturbative QCD (pQCD) at leading (LO), next-to leading (NLO), and next-to-next-to leading order (NNLO) are now available for most production processes.

SM based on EW and QCD interactions is a very successful theory verified by many experiments. But still, it is an incomplete theory with some known issues. The absence of gravitational force might not be an issues for the high energy physics, but it also does not involve "dark matter" nor "dark energy". The SM assumes neutrinos to be massless, which we now know to be wrong. Therefore, the presence of things outside the SM is a great motivation for us to search for processes beyond the SM in every possible scenario. And the top quark with large mass and short lifetime is great candidate to look for new physics.

1.2 Top Quark

The top quark is the most massive known fundamental particle to date. It forms a weak isospin doublet with the bottom quark in the third generation of quarks. Top quark is known for its very short lifetime, even shorter than time needed for QCD hadronization, so the top quark is the only bare quark observed [4]. After the discovery in 1995 a lot of effort has been put into measuring its mass, nowadays the precision is gained by combination among the experiments achieving precision under 0.5% [24]

$$m_t = 173.34 \pm 0.27(\text{stat.}) \pm 0.71(\text{syst.})\,\text{GeV}. \tag{1.3}$$

There are already new measurements that are not in the combination, but the value is already dominated by the systematic uncertainty. With a mass above the mass of the W boson, the top quark decays rapidly to a W boson and a b quark. The

[4] Due to the QCD confinement quarks are bound into hadrons and cannot be separated.

extremely short life time of about 5×10^{-25} s presents an unique opportunity to study a bare quark. The top quark lifetime can be measured experimentally through the decay width of the top quark. The charge of top quark is $+\frac{2}{3}e$, fractional as for other quarks. EW theory will also hold with exotic top quark charge of $-\frac{4}{3}e$, but that has been excluded at both Tevatron and LHC with over 99% probability and the SM value is acknowledged. Top quark has weak isospin of $+\frac{1}{2}$. It is the only quark that has Yukawa coupling to the Higgs boson of order of unity. Top quark phenomenology is a unique place to understand and test strong interactions, both in the perturbative and non-perturbative regimes. And an accurate knowledge of its properties is important for explaining fundamental interactions at the electroweak breaking scale and beyond. The properties can be studied experimentally at any type of accelerator or collider, where top quark is produced. At this moment, that means only Tevatron (that stopped its operation in 2011) and LHC, but there are plans for more facilities to measure top quarks, among other physics program, especially the International Linear Collider (ILC) and the High-Luminosity upgrade of the LHC (HL-LHC).

There are many detailed reviews of top quark physics dealing with both experimental and theoretical aspects of the top quark - References [21, 25, 26, 28] are among the most useful. The following sections will briefly summarize the top quark production and the top quark decay and the respective top quark properties.

1.2.1 Top Quark Production

The top quark production mechanisms differ according to the particles colliding and the centre-of-mass energy. At the Tevatron, proton and antiproton were colliding at centre-of-mass energy of $\sqrt{s} = 1.96\,\text{TeV}$, producing top quarks dominantly via through the $q\bar{q}$ annihilation. On the other hand, at the LHC, only protons collide at different centre-of-mass energies of 7 TeV, 8 TeV, and 13 TeV with the top quark production coming mostly from gluon fusion. In both cases, top quarks are produced predominantly in pairs, referred to as the top quark pair production. This thesis is dealing only with the Tevatron production of the top quark pairs.

The cross section for the $t\bar{t}$ production at the Tevatron is predicted to be [29]

$$\sigma_{t\bar{t}} = 7.37 \pm 0.39\,\text{pb} \tag{1.4}$$

for the top quark mass of 173.3 GeV by employing an approximate next-to-next-to-next-to-leading-order (aNNNLO) calculations. NNLO+NNLL calculation [33] gives cross-section prediction of

$$\sigma_{t\bar{t}} = 7.16^{+0.11}_{-0.20}\,{}^{+0.17}_{-0.12}\,\text{pb}. \tag{1.5}$$

The latest DØ measurement [30] (using the same data as this thesis) is in a very good agreement with the theory by measuring the cross-section of

$$\sigma_{t\bar{t}} = 7.26 \pm 0.13(\text{stat.})^{+0.57}_{-0.50}(\text{syst.})\,\text{pb}. \tag{1.6}$$

Approximately 85% of top pairs are produced via the annihilation of a quark and an antiquark to a gluon which then decays to a top quark and top antiquark. The remaining 15% of top pairs are produced by the fusion of two gluons. The leading order Feynman diagrams of both processes are shown in Figure 1.1. For the measurement in this thesis, the ratio of the two production mechanisms is important. It can be understood by considering the typical momentum fraction x of the colliding hadron which is required to produce a pair of top quarks. A centre-of-mass energy of at least the mass of the two top quarks, $2m_t$, is required. For the Tevatron energies, the colliding parton needs to have a momentum fraction $x = \frac{2m_t}{\sqrt{s}} \approx 0.18$ of the hadron's momentum to produce the top quark pair. For this value of x, the quark distribution functions, in particular the u and the d valence quark distribution, are much larger than that of the gluon. The gluon distribution increases more steeply towards low x and thus the LHC top quark pair production is dominated by gluon fusion.

Top quarks are produced mainly in pairs, but there is also a possibility that only one single top quark will appear with a cross section about three-times smaller and more background processes to consider. The single top processes produced by electro-weak interactions are different to the pair production and their leading order diagrams are shown in Figure 1.2, where the W. The cross section for the single top production has a theoretical prediction of $\sigma_t = 3.12\,\text{pb}$ [31, 32]. DØ measured this value to be [34] $\sigma_t = 3.43^{+0.73}_{-0.74}\,\text{pb}$, which is in good agreement with prediction. This measurement is focused only on top quarks pairs and thus single top production is not further considered in the text.

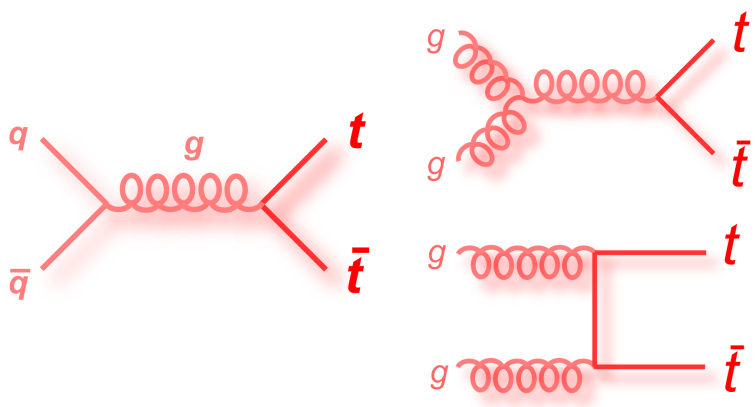

Figure 1.1: Feynman diagrams for top quark pair production at the Tevatron with $q\bar{q}$ annihilation on the left and two possibilities of gluon fusion on the right.

1.2.2 Top Quark Decay

In SM, the top quark is predicted to decay to a W boson and a b quark ($t \to Wb$) almost 100% of the time. In general, the top quark can decay to any down-

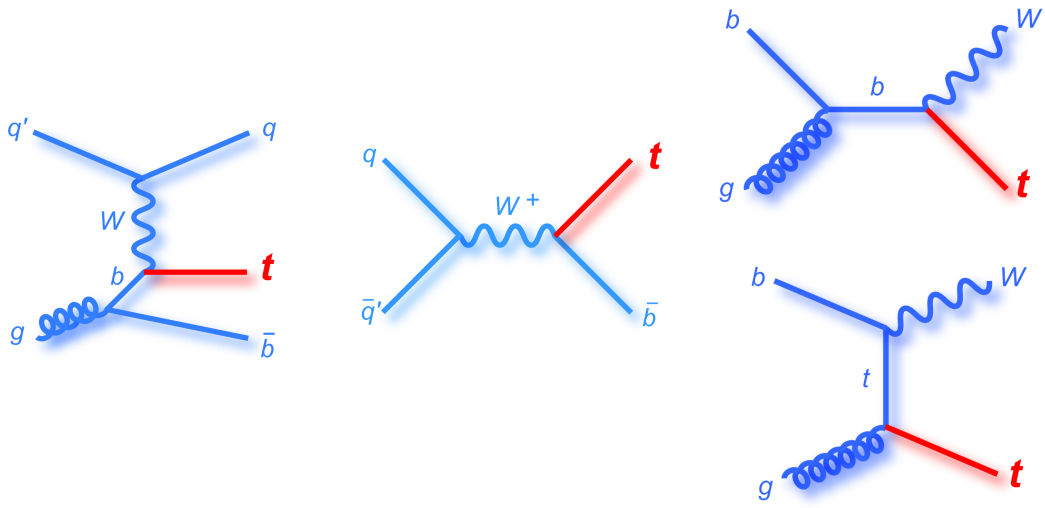

Figure 1.2: Feynman diagrams of single top quark production at the Tevatron, with t channel on the left and s channel in the middle and two Wt channels on the right.

type quark and a W boson. The rate at which the different decays take place is proportional to the CKM matrix, Eq. (1.2), elements $|V_{tq}|^2$, with $q = d, s, b$. Under the assumption that there are only three families of quarks, the matrix elements $|V_{tq}|^2$ are well constrained, with $|V_{tb}|$ close to unity [21].

The value of $|V_{tb}|$ can be determined experimentally by comparing branching fractions of the different decays $t \to Wq$, with $q = b, s, d$. The ratio of these fractions is measured by counting how many decays of top quarks are compatible with a signature corresponding to $t \to Wb$ and the total number of top quark decays. The most recent measurement by DØ [35] finds $0.90 < V_{tb} < 0.99$ at 95% confidence level assuming the CKM matrix unitary. With the top quark mass larger than the mass of the W boson, only the decay $t \to Wb$ is assumed in this work.

The top quark decay width is a quantity that is corresponding to top quark lifetime with NNLO prediction of a width of 1.32 GeV [36] and a lifetime of 5×10^{-25} s. The width has been measured experimentally by the DØ experiment [37] resulting in $\Gamma_t = 2.00^{+0.47}_{-0.43}$ GeV, which translates into top quark lifetime of $\tau_t = 3.29^{+0.90}_{-0.63} \times 10^{-25}$ s. For comparison, a typical hadronization timescale is an order of magnitude larger than this lifetime.

Important feature of the lifetime shorter than hadronization is that itop quark decays before its spin can be flipped by the strong interaction. Thus, the top-quark polarization is directly observable via the angular distribution of its decay products. It is possible to define and measure quantities sensitive to the top quark spin and its production mechanism. Top quark pairs should be produced unpolarized in the SM, but spins of top and antitop quarks are correlated, preserved and affect the angular distribution of the decay products. The $t\bar{t}$ system is produced with parallel spins for $q\bar{q}$ annihilation and with antiparallel spins for gluon-gluon fusion.

This means that the $t - \bar{t}$ spin correlations are predicted at the Tevatron by the SM to be non-zero and a value consistent with this expectation has been observed by the DØ Collaboration [38] as well as by other experiments [39]. This confirms the top quark spin of 1/2 and the fact that it decays before strong interaction can affect the spins. There are also possible processes beyond the SM that could affect this measurement to enhance unlike spin contribution or change the correlation by changing the fraction of gluon fusion produced top pairs. Therefore it is essential to perform measurements of the top quark polarization and the top quark spin correlations to search for new physics in top quark production and decay or to confirm the SM. Other quantities are sensitive to the BSM physics like the top quark forward-backward asymmetry (top quark charge asymmetry), or the differential cross-section in the $t\bar{t}$ production.

The daughter products from the W boson decay determine the the top quark channel. The W boson has two different types of decays. For the first type, called leptonic, the W boson decays to a lepton and a neutrino, $W \to \ell_i \nu_i$, where i is either electron, muon, or tau flavor. In the second type of decay, called hadronic, the W boson decays to two quarks, $W \to q\bar{q}$, where one is either up or charm quark, second can be either down, strange, or bottom quark. The assignments of quarks or antiquarks depends on the charge of the W boson in order to preserve the charge in the decay. In the $t\bar{t}$ decay, there are two W bosons and two b quarks leading to signature $t\bar{t} \to W^+ b W^- \bar{b}$. By combining different decay modes of the $W^\pm$ bosons, three experimentally distinguished final states are observed [21] and summarized in Figure 1.3.:

1. The lepton+jets channel with one ($W \to \ell\nu$) and one ($W \to q\bar{q}$). The branching ratio is BR = 43.8%. The decay topology up to the final state is $t\bar{t} \to W^+ b W^- \bar{b} \to (q\bar{q}b)(\ell\nu\bar{b})$.

2. The dilepton channel when both W bosons decay leptonically with BR = 10.5% and topology of $t\bar{t} \to W^+ b W^- \bar{b} \to (\ell^+\nu b)(\ell^-\bar{\nu}\bar{b})$.

3. The all jets channel when both W bosons decay hadronically with BR = 45.7% and topology of $t\bar{t} \to W^+ b W^- \bar{b} \to (q\bar{q}b)(q\bar{q}\bar{b})$.

The branching ratios for lepton+jets and dilepton channels are actually smaller in real experiments. It is so due to very difficult reconstruction of final states with τ lepton as the τ decays very quickly, hadronically in 65% cases. Hadronic τ decays are reconstructed as jets and thus the events contribute to the multijet background, while leptonic decays, where τ decays to electron or muon, are still correctly assigned to the lepton+jets and dilepton channels. In the end, the branching ratios observed by the experiments are approximately 6.5% for dilepton channel and 34.3% for lepton+jets channel. This thesis describes the measurement in the lepton+jets final states with the respective Feynman diagram of the decay shown in Figure 1.4.

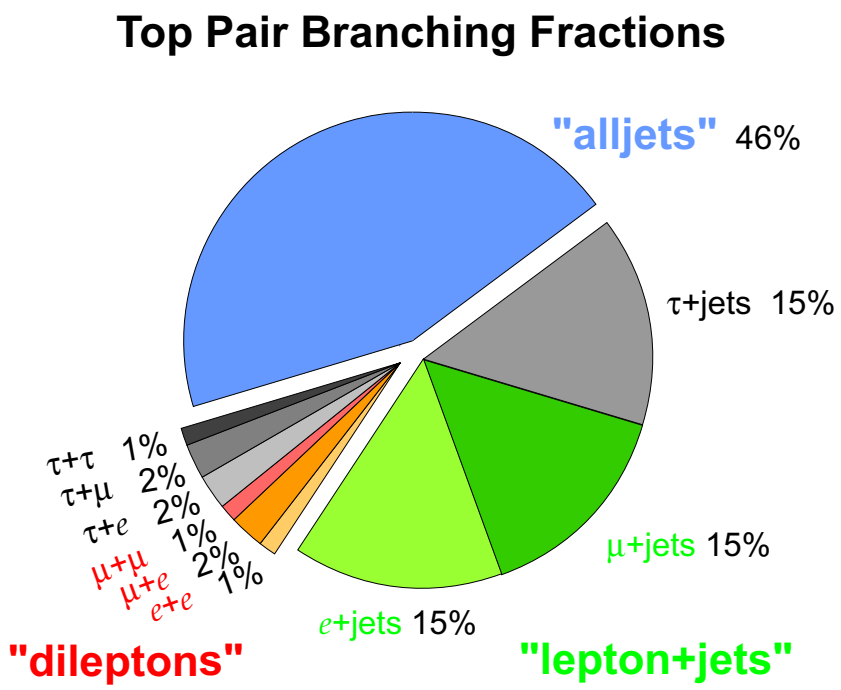

Figure 1.3: Final states signatures for the $t\bar{t}$ pairs.

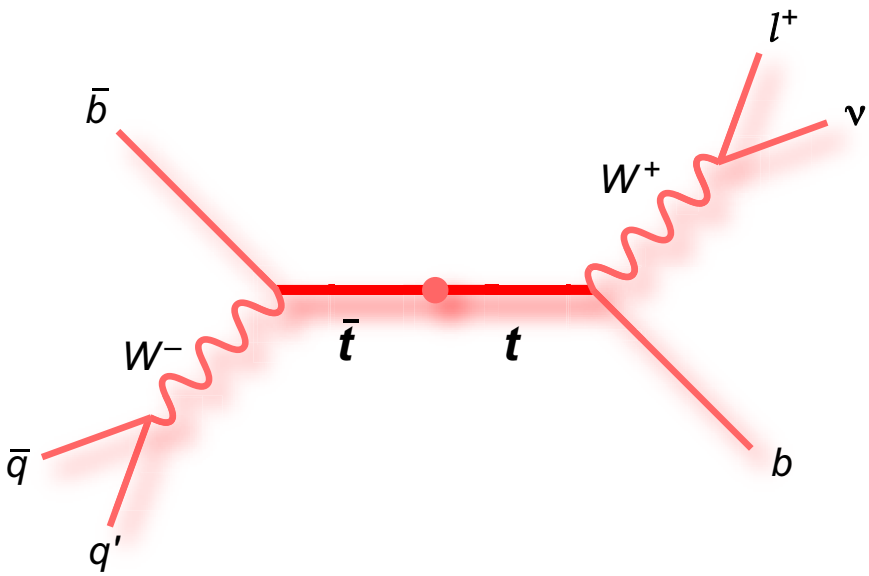

Figure 1.4: Feynman diagram for the top quark pair decay to the lepton+jets final state with positively charged lepton.

1.3 Author notes

In the introduction chapter, I have tried to guide the reader to the basics of the Standard Model, elementary particles, and top quarks physics. The description is not complex and certainly lacks of many details, but complexity was not the purpose as it would need a large number pages to get to the widely acceptable theory of the Standard Model (if this is even possible!) and to describe everything that happened in the field of top quark physics so far. Another goal of the introduction was to present the motivation for the measurement of the top quark polarization.

This chapter is written from my point of view. I wanted to tell the reader more than list of facts, but also back up the motivation for this measurement and for the top quark physics by my own observations made through the years I have spent analyzing the data and trying to understand the top quark.

As one would expect, the content of this chapter is not referring directly to my work, but mainly to the theory and studies made before by many great physicists. In many citations in this chapter, I focused mostly on results from the DØ experiment, as those results are more familiar to me since I was participating in my top quark group meetings at DØ and watched the development of some of these measurements. If I should stress my contribution, apart from writing this introduction, it is my involvement in top quark analyses at the DØ experiment. I was participating in the selection of top quark events in the lepton+jets channel and my contribution to systematical uncertainties evaluation was recognized in the measurement of the top quark mass [40], where I was noted as one of the main authors. Even now with the many LHC results, this is the most precise single measurement of the top quark mass.

Chapter 2

Experimental Apparatus

For any measurement involving top quarks, two very specific pieces of equipment need to be in operation. First is a machine to produce the top quarks. Top quark with a lifetime of 5×10^{-25} s is not present in nature nor in the universe. To create conditions for the production of top quarks, one needs a high-energy collision of particles that can be achieved by cosmic rays colliding with particles in the air, or created by particle accelerator or a collider. In this measurement, the Tevatron Collider is used to produce the top quarks. Second equipment is a machine to detect and measure the final state products of the top quark decay. In general this has to be high-energy multipurpose detector system composed of several types of detectors. The DØ detector is used in this thesis. Both, the Tevatron Collider and the DØ detector, are located in the Fermi National Accelerator Laboratory (Fermilab) in Batavia, IL, USA. The operation of both machines was shut down in September, 2011. However, the unique dataset is still worth analyzing since most likely there will be no $p\overline{p}$ accelerator in the near future. This chapter provides the description of the Tevatron Collider and the DØ detector.

2.1 Tevatron Collider

The Fermilab accelerator complex [41] consists of a chain of eight accelerators (of which two are storage rings): the Cockroft-Walton injector, the LINAC (Linear Accelerator), the Booster, the Main Injector, the Debuncher, the Accumulator, the Recycler, and the Tevatron. General schematic view of the complex is shown in Figure 2.1.

The acceleration process begins with a small bottle of hydrogen. The protons are produced by turning the hydrogen gas into hydrogen ions (H^-) which is done in the magnetron chamber. Then the 750 kV Cockroft-Walton pre-accelerator accelerates the H^- ions to 750 keV through the static electric field. The ions are further accelerated to 400 MeV through a series segmented alternating electric fields in the LINAC [42], which is a 150-meter-long linear accelerator consisting of drift tubes and vacuum gaps. The electric field in LINAC is produced by radio frequency (RF) power and polarized in the same direction in all gaps. The ions increase their speed

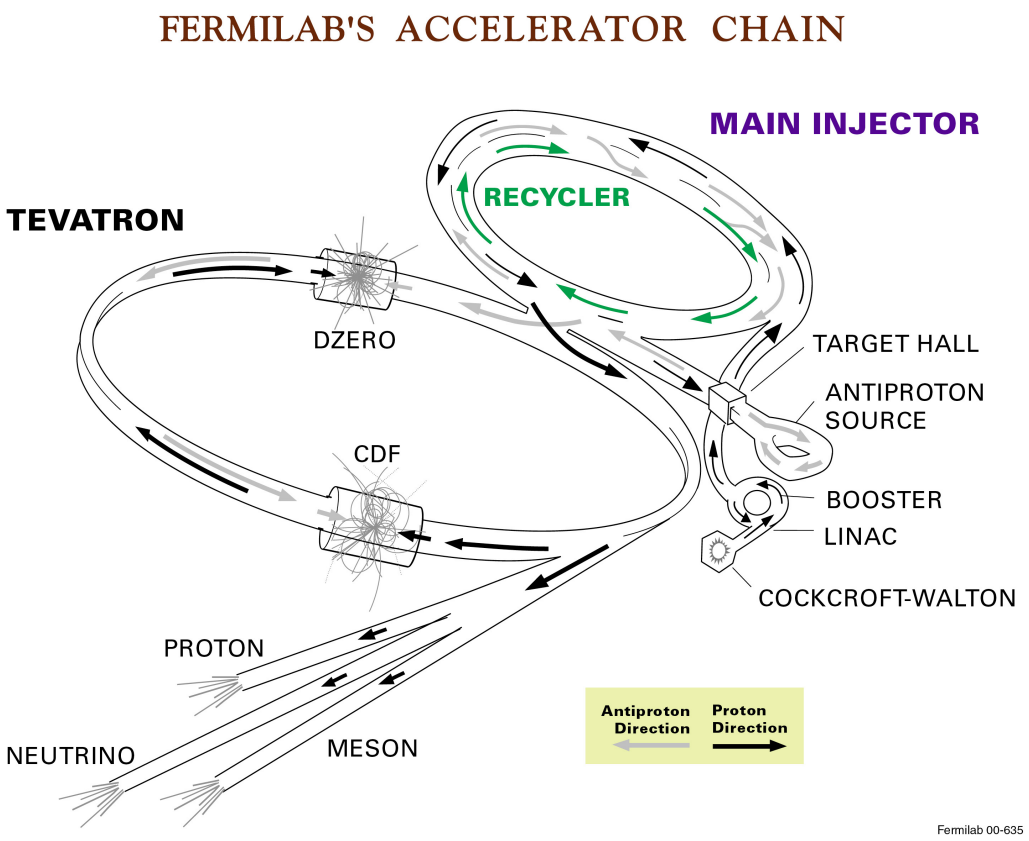

Figure 2.1: The Fermilab accelerator complex - Tevatron accelerator chain [41].

in the gaps and keep the speed inside the drift tubes when the electric field reverses. Therefore, the drift tubes become longer and longer as the velocity of H^- increases. Then, the H^- ions are send through a carbon stripping foil to make bare protons by removing both electrons. The proton beam is injected into the Booster [43], a synchrotron ring with a circumference of 475 m. The protons are here bent into a circular orbit by dipole magnets and accelerated to 8 GeV by RF cavities within 33 ms. The apparatus described in this paragraph is referred as the Proton Source.

After the Booster, protons are injected into the Main Injector [44], a synchrotron accelerator with a circumference of approximately 3.3 km. It consists of a series of dipole magnets for bending the particle beam and quadruple magnets to focus the beam. The protons can be accelerated up to 150 GeV within 3 s. The accelerated protons from the Main Injector are used for two purposes, at 120 GeV for fixed-target operation, in our case for the antiproton production, and at 150 GeV for injection into the Tevatron. The 120 GeV protons from the Main Injector are directed to strike a nickel target every 1.47 seconds to produce antiprotons with energy of ≈ 8 GeV. Antiproton is created only once per approximately 50 thousands incident protons. A lithium lens and a pulsed magnet (which acts like a charge-mass spectrometer) are used to remove other negatively charged particles produced and to focus the

antiprotons into the beam line. The antiprotons are then moved into the Debuncher where the processes called stochastic cooling and radio-frequency bunch rotation are used to reduce the beam emittance and to minimize the momentum spread. The beam is then passed into the Accumulator where antiprotons are collected and further cooled. For the collisions at the Tevatron, large number of antiprotons is needed, approximately 30000 cycles, which took hours to accomplish. The Debuncher and Accumulator are both 8 GeV synchrotrons with circumferences of 505 m and 474 m. Together with the target station they are called the Antiproton Source [45]. Antiprotons are then sent back to the Main Injector or to the Recycler [46]. The Recycler is a fixed-energy storage ring for the antiprotons, where antiprotons from the source are accumulated and also the remaining antiprotons after each Tevatron storage recycled. It is housed in the Main Injector tunnel and it was one of the main upgrades for Run II operation of the Tevatron. The Recycler provides stochastic and electron cooling and thus improves the antiproton beam quality. Antiprotons from Accumulator or Recycler go to the Main Injector where are accelerated up to 150 GeV.

Both protons and antiprotons beams at 150 GeV were injected into the last and also the largest synchrotron in the accelerator chain, the Tevatron [47]. They were ramped up to 980 GeV in separate tubes and opposite direction within the nearly 2 km diameter storage ring in a 4.2 T magnetic field generated by 774 niobium-titanium superconducting dipole magnets. Both beams were focused by 240 niobium-titanium quadruple magnets that narrowed them down into a small transverse area of 5×10^{-5} cm^2 for head-on collisions. There were two crossing points, the CDF and the DØ, where the opposite beams collided at a centre-of-mass energy of 1.96 TeV. Each beam consisted of 36 bunches grouped in three trains of 12 bunches with a bunch spacing of 396 ns. Each proton bunch consisted of up to $2.5 - 3.0 \times 10^{11}$ protons, while antiproton bunches had $0.4 - 1.0 \times 10^{11}$ antiprotons each[1]. This corresponds to a collision rate of ≈ 2.5 MHz. During the period of collisions, also known as a "store", the proton and antiproton collided with an instantaneous luminosity of about $\mathcal{L}_{\text{inst}} \approx 200 \times 10^{30}$ cm^{-2}s^{-1}. The instantaneous luminosity is defined as

$$\mathcal{L}_{\text{inst}} = \frac{f N_p N_{\overline{p}}}{A}, \tag{2.1}$$

where f is the bunch crossing frequency, N_i are the number of particle i per bunch, and A is the effective cross section area of the beams. A can be expressed in terms of the transverse widths of the proton and antiproton beam, and the luminosity in the Tevatron can be written as

$$\mathcal{L}_{\text{inst}} = \frac{f N_p N_{\overline{p}}}{2\pi(\sigma_p^2 + \sigma_{\overline{p}}^2)} F, \tag{2.2}$$

where σ_i is the effective standard deviation of the particle i beam distribution at the interaction point in the detector, and F is a factor that depends on the

[1] There have been attempts to have 103 bunches with bunch spacing 132 ns [45].

bunch length and the interaction point. For Tevatron Run II, σ_p and $\sigma_{\overline{p}}$ are about $25 - 30\,\mu\text{m}$, and F is about 0.7 [45]. The instantaneous luminosity during the run exceeded $400 \times 10^{-30}\,\text{cm}^{-2}\text{s}^{-1}$ at the beginning of stores. The instantaneous luminosity was decreasing with time as collisions took place, and the store usually ended within 24 hours. To get an optimal antiproton beam took about 21 hours.

The Tevatron began its operation in 1983 and it was ground-breaking accelerator with many achievements and records set [2]. In the beginning, the physics program focused on fixed target experiments. The collider program, with two detectors DØ and CDF, was operating later and was split in two phases - Run I and Run II. Run I took place from 1992 to 1996 with the Tevatron operating at the centre-of-mass energy of 1.8 TeV and ended with about $125\,\text{pb}^{-1}$ of integrated luminosity. Major success of Run I was the discovery of the top quark. The setup and characteristic values described in this section represent only Run II, which corresponds to the DØ data used in the analysis. Run II used upgraded accelerators and magnets and in the period from 2001 until 2011, it reached centre-of-mass energy of 1.96 TeV. It was a very successful operation with the final integrated luminosity of almost $12\,\text{fb}^{-1}$ as shown in Figure 2.2. Inverse picobarns (pb^{-1}) and inverse femtobarns (fb^{-1}) are conventional units for time-integrated luminosity. With $1\,\text{fb}^{-1}$ of integrated luminosity, we expect to find 1 event with femtobarn (fb) cross-section within this data, while $1\ \text{fb} = 10^{-39}\,\text{cm}^2$.

2.2 DØ Detector

The DØ detector [48] is a multipurpose detector designed to study, identify, and measure particles originating from $p\overline{p}$ collisions in the Tevatron. It consists of several subdetectors. An overview of the DØ detector is shown in Figure 2.3. DØ is a typical high energy physics detector that has its subdetectors arranged symmetrically around the interaction point and the proton beam. It is about 13 meters tall and 20 meters long and consists of three major subsystems: a tracking detector for measuring momenta of charged particles and identifying the vertices of interactions, a uranium-liquid argon calorimeter for measuring the energies of electromagnetic and hadronic showers, and a muon spectrometer for measuring muon momenta. In this section, the Trigger system will be discussed as it belongs to the detector and was essential for its successful performance. The operation of the detector has two major epochs, same as the Tevatron accelerator, Run I and Run II, where the latter is formally split in several subperiods: Run IIa in 2001 – 2006 and Run IIb 2006 – 2011 that was further splitted into Run IIb1, IIb2, IIb3, and IIb4 parts. There was an extensive upgrade of the detector between Run I and Run II periods and minor upgrade between Run IIa and Run IIb periods. Following text will focus only on the upgraded Run II detector described with more details in Ref. [48].

[2] In May 1986, the Tevatron was named one of the Top Ten Engineering Achievements of the Last 100 Years

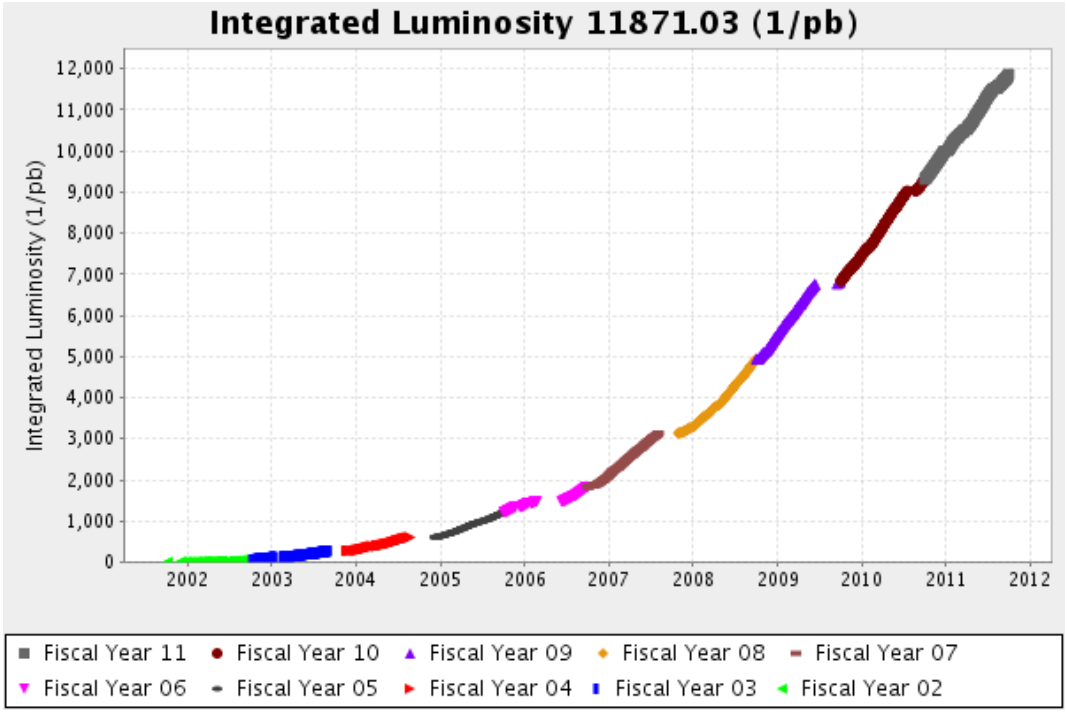

Figure 2.2: Tevatron Run II integrated luminosity with fiscal years shown.

2.2.1 Coordinate System

The coordinate system is used to describe parts of detectors, areas and angles covered and particles properties in the analysis. The DØ uses a characteristic right-handed coordinate system with the origin at the designated interaction point in the center of the detector. The positive z direction is defined along the direction of the incoming proton, which are circulating clockwise in the ring, and the x and y axes pointing upwards and towards the center of the Tevatron ring, respectively. For the determination of the positions in the transverse plane, cylindrical coordinates (r, θ, ϕ) with radius r, polar angle θ, and azimuthal angle ϕ defined as

$$r = \sqrt{x^2 + y^2}, \tag{2.3}$$

$$\theta = \arctan \frac{r}{z}, \tag{2.4}$$

$$\phi = \arctan \frac{y}{x}, \tag{2.5}$$

are used.

It is common to use variables invariant under Lorentz boosts in the z direction. In particular, we choose the transverse momentum p_T (the momentum in the (x, y) plane), the pseudorapidity η (Lorentz-invariant is the difference of rapidities), the

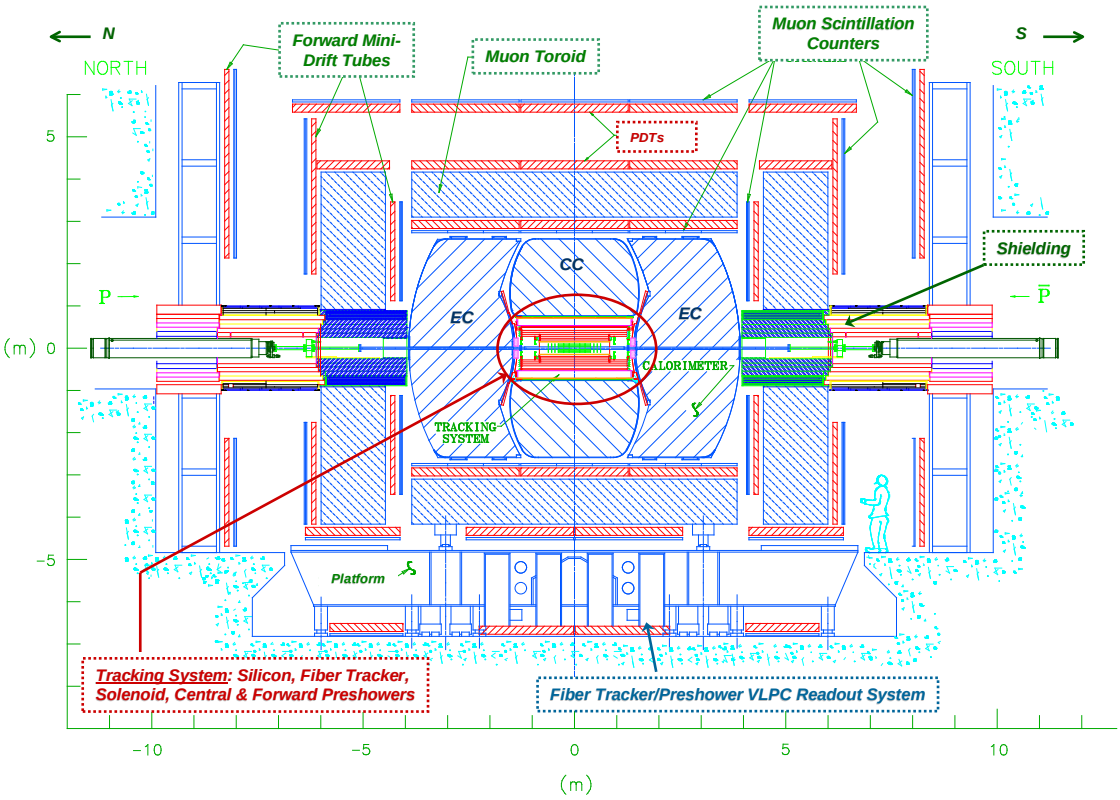

Figure 2.3: Cut view of the upgraded DØ detector.

azimuthal angle in the transverse plane ϕ, and the observed energy E to describe the kinematic properties of all objects. The pseudo-rapidity η is a function of θ

$$\eta = -\ln \tan \frac{\theta}{2}, \tag{2.6}$$

while for massless particles or where masses can be neglected, the pseudo-rapidity is equivalent to the rapidity y

$$y = \frac{1}{2} \ln \frac{E + p_z}{E - p_z}, \tag{2.7}$$

where p_z is the longitudinal component of the momentum vector. Pseudorapidity of particles in the final state is calculated with respect to the measured position of each vertex. In studying different regions of the detector, it is more convenient to use the detector pseudorapidity η_{det}, which reflects η measured relative to the center of the detector.

The distance in the $\eta - \phi$ plane is usually denoted as ΔR and is defined as

$$\Delta R = \sqrt{(\Delta\eta)^2 + (\Delta\phi)^2}. \tag{2.8}$$

2.2.2 Tracking System

The momentum, electric charge and vertex origin of an outgoing charged particle are first detected and measured according to its curved trajectory in the central tracking system, which is the innermost detector part. DØ central tracking instruments are comprised of 3 components: a Silicon Microstrip Tracker (SMT) [49], a Central Fiber Tracker (CFT) and a surrounding solenoidal magnet. The SMT and CFT are able to locate the primary vertex with about 35 μm resolution along the beam line and help identifying jets originated from b quarks. Figures 2.4 and 2.5 show the schematic views of the DØ central tracking system.

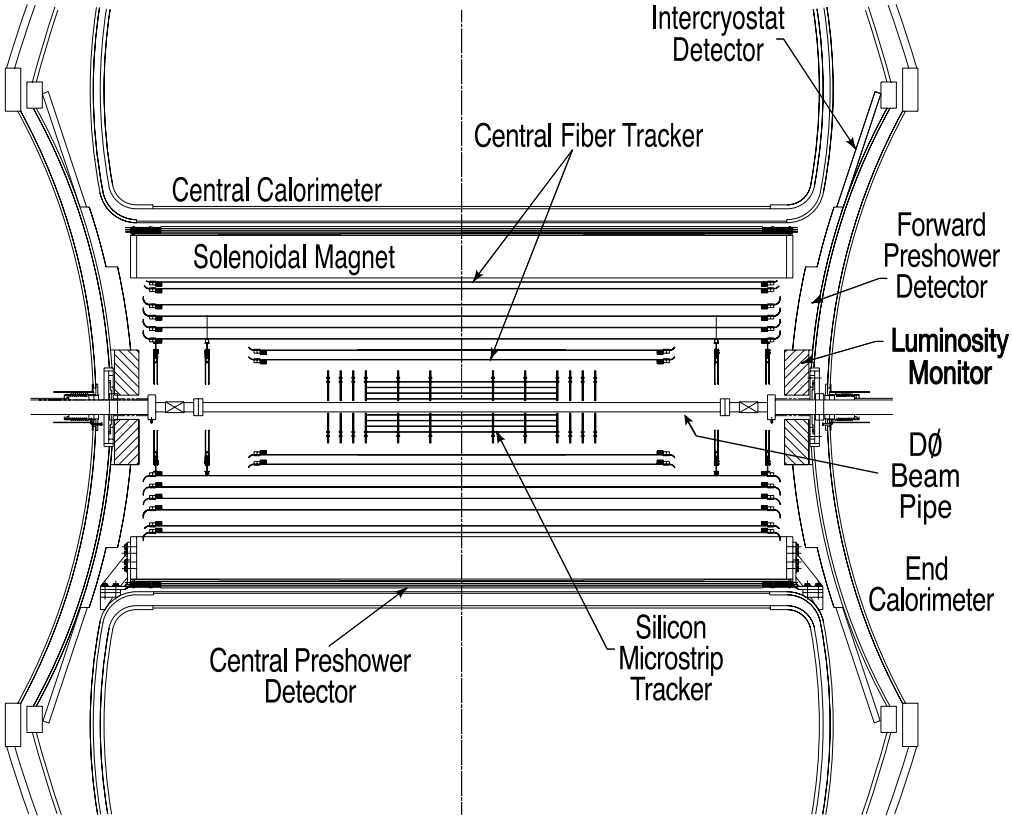

Figure 2.4: Cross-sectional view of the central tracking system.

The Silicon Microstrip Tracker is the closest detector to the beam pipe. The high density of silicon strips in the SMT allows high resolution track finding and vertex identification over nearly full η_{det} region. The SMT consists of silicon wafers in the form of barrel and disk modules. The wafers are n-type silicon etched with many p-type silicon strips. There are six barrel modules, each having four cylindrical layer of 12 cm long, shown in Fig. 2.6. Each of the four layers is made up of two sublayers of overlapping silicon sensors to cover the whole angle range. Inter-spaced between the barrels are the 12 F discs. In addition, there are 4 larger H discs in the far forward regions to provide a high pseudo-rapidity region coverage. The F and

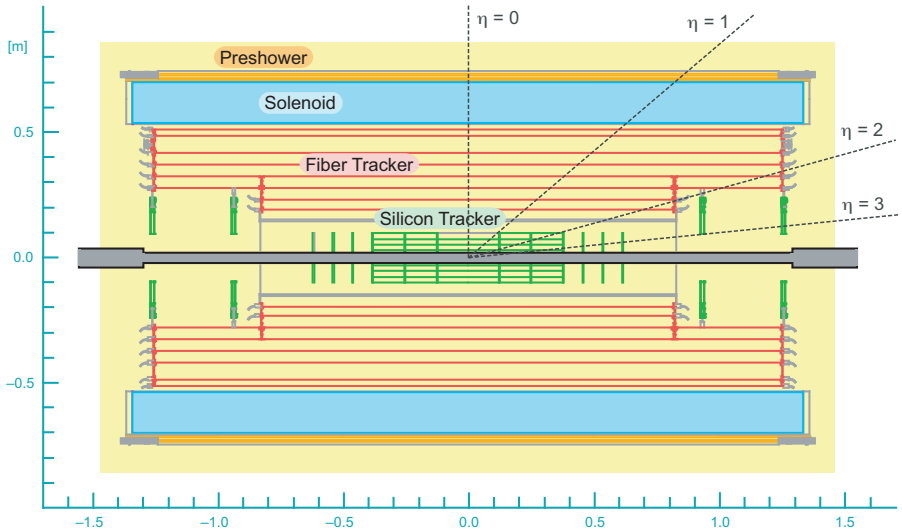

Figure 2.5: Schematic view of the DØ central tracking system.

H disks are made of 12 double-sided and 24 single-sided wedges, respectively, and are used to measure both the (r, ϕ) and (r, z) components of a particle trajectory. In the double-sided wedges, the two surfaces are implanted with p-type and n-type silicon strips respectively. Moreover, the strips in one surface are aligned at a small stereo angle with respect to the other surface, providing a three dimensional measurement of position. The picture of the DØ silicon microstrip detector is shown in Figure 2.7.

After the SMT follows the Central Fiber Tracker, which occupies the radial space 20 to 52 cm from the beam pipe center. The CFT is made of 76800 scintillating fibers mounted on eight concentric cylinders outside the SMT, providing coverage for $|\eta_{\text{det}}| < 1.7$. Each cylinder consists of double layers of fibers in the axial direction and a doublet layer of fibers with a stereo angle ϕ oriented at $+3°$ for odd-numbered layers and $-3°$ for even-numbered layers). Both of the (r, ϕ) and (r, z) coordinates are measured in the CFT with a resolution of about 100 μm. The schematic view of the CFT layers is shown in Figure 2.8. When a charged particle passes through a fiber, the scintillator emits light through a rapid fluorescence. Readout fibers are coupled to waveguides that transport the scintillation light to visible light photon counters (VLPCs) for processing.

The tracker is surrounded by a superconducting solenoid magnet of 2.73 m in length and 1.4 m in diameter. It submerges the whole trackers in a 2 T magnetic field. The thickness of the magnet is designed to be about 1 radiation length to balance optimal momentum resolution with tracking pattern recognition. By the presence of magnetic field the momentum of charged particles can be determined, because of the Lorentz force which causes the helical trajectory of charged particles.

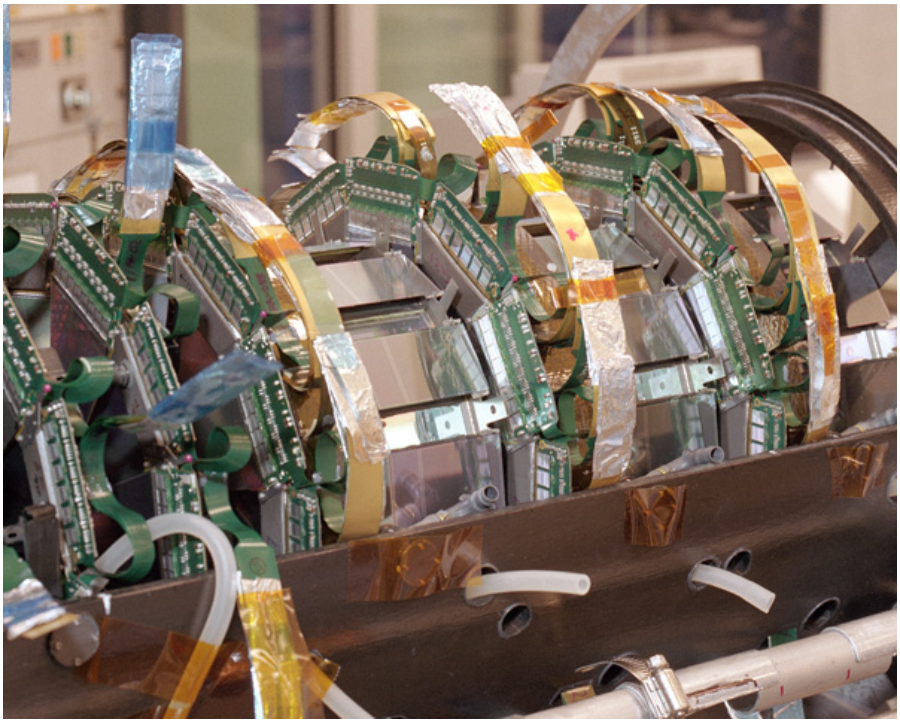

Figure 2.6: Photo of the DØ SMT barrel.

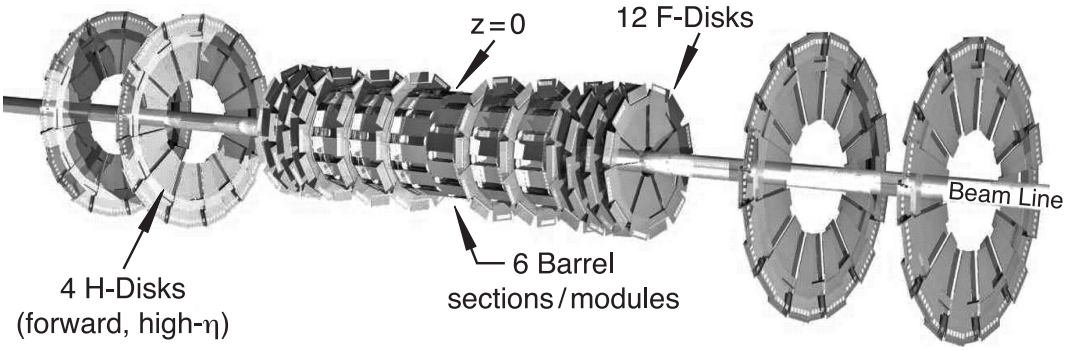

Figure 2.7: The arrangement of the DØ Silicon Microstrip Tracker.

2.2.3 Calorimeter

First, there is preshowering system located between the Tracking and the Calorimetry systems that features a Central Preshower Detector (CPS) and two Forward Preshowering Detectors (FPS). The CPS has three layers of triangular scintillating fiber strips interlocked together and covers region of $|\eta_{\text{det}}| < 1.3$. Each of the FPS has four layers and they cover $1.5 < |\eta_{\text{det}}| < 2.5$. This arrangement is used to cover most of the calorimeter space and to improve the electron and photon identification as well as background rejection during both online and offline recon-

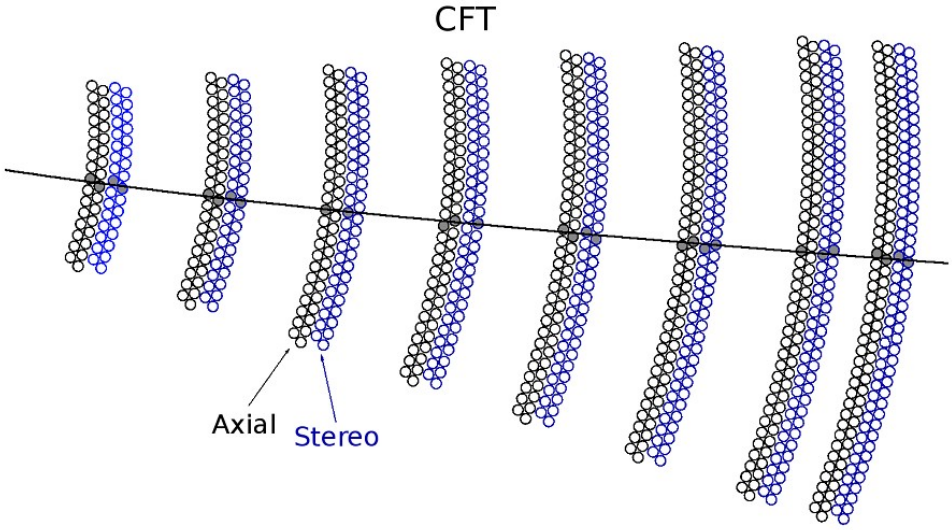

Figure 2.8: The arrangement of the layers in DØ Central Fiber Tracker.

struction. The fast energy sampling of the particles before entering calorimeter and position measuring capability make the preshowering system aid to both the calorimetry system and tracking system. Both CPS and FPS are constructed of triangular scintillator strips. In the center of each strip, a wavelength-shifting fiber is embedded to collect and carry scintillation light to the end of the detector. 11 mm thick lead-stainless-steel absorber is plugged in between the two FPSs to induce high energy photons or electrons to begin showering. The light from the fibers is then transmitted to an attached VLPC for readout.

The DØ liquid argon calorimeter detects and records the energy of the particles like electrons and photons, and hadronic jets, as they interact with the calorimeter materials. The data from calorimeter are also used to determine missing transverse energy $\not{E}_T$ associated to the neutrinos. A high energy electron penetrating material of large atomic number, like uranium, initially radiates photons in a process known as bremsstrahlung. A radiated high energy photon penetrating the material further will produce an electron and positron pair. Hence, both electrons and photons of high energies produce extensive electromagnetic showers, i.e. with an increasing numbers of lower-energy electrons and photons as the shower develops. The high energy hadrons interact with nuclei of the material via the strong force. This interaction produces secondary hadronic particles and a subsequent hadronic shower, i.e. a large number of hadronic particles, but also photons from decays of hadrons. Once the particles in the electromagnetic and hadronic showers have sufficiently low energies, their dominant interaction with the calorimeter material will be through ionization of atoms, which can also be detected.

The calorimeter is divided into three parts as shown in Figure 2.9, the central calorimeter (CC) and two end calorimeters (EC). Each calorimeter contains electromagnetic and hadronic sections, which are divided into fine and coarse parts.

The CC and EC are located in their own cryostats and held at a temperature of approximately 90 K. This temperature is important for liquid argon (LAr), which is the active medium in the calorimeter. The purity of liquid argon is critical to detector performance and needs to be monitored, especially for electronegative contaminants like oxygen. The CC part covers $|\eta_{\text{det}}| \leq 1$, the ECs extend this coverage to $|\eta_{\text{det}}| \approx 4$. Most calorimeter cells have transverse dimensions of $\eta_{\text{det}} \times \phi$ of 0.1×0.1 rad, except for the most forward regions, where they are 0.2×0.2 rad. All calorimeter components are segmented radially as towers from inside out as shown in Figure 2.10.

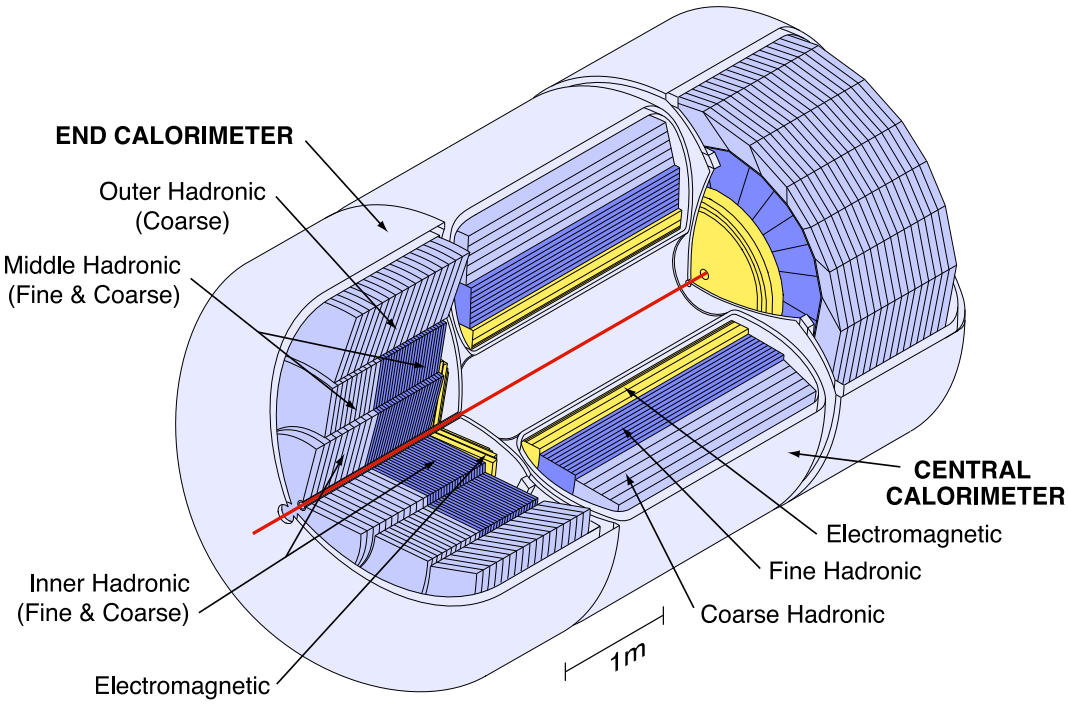

Figure 2.9: Schematic view of the DØ Liquid Argon Calorimeter.

The basic detection unit is a calorimeter cell as shown in Figure 2.11. The gaps are filled in all parts of calorimeter with the active medium - liquid argon. Metal absorber plates are grounded in order to establish an electric field. The absorber layers are geometrically and materially different in the electromagnetic (EM), coarse hadronic (CH), and fine hadronic (FH) sections. The EM thin plates are 3 mm thick in CC and 4 mm thick in the ECs, all made from nearly pure depleted uranium. The FH layer uses a 6 mm thick uranium-niobium alloy plates while CH layer uses 46.5 mm thick copper plates in the CC and stainless steel plates in the EC.

Since the calorimeter system is contained in three separate cryostats, it provides incomplete coverage in the pseudo-rapidity region $0.8 < |\eta_{\text{det}}| < 1.4$, which degrades the energy resolution. To address the issue, the Inter-cryostat detector (ICD) is mounted on the exterior surface of the ECs. The ICD covers $1.1 < |\eta_{\text{det}}| < 1.4$ and is made of small scintillating tiles, each of which provides the same coverage as

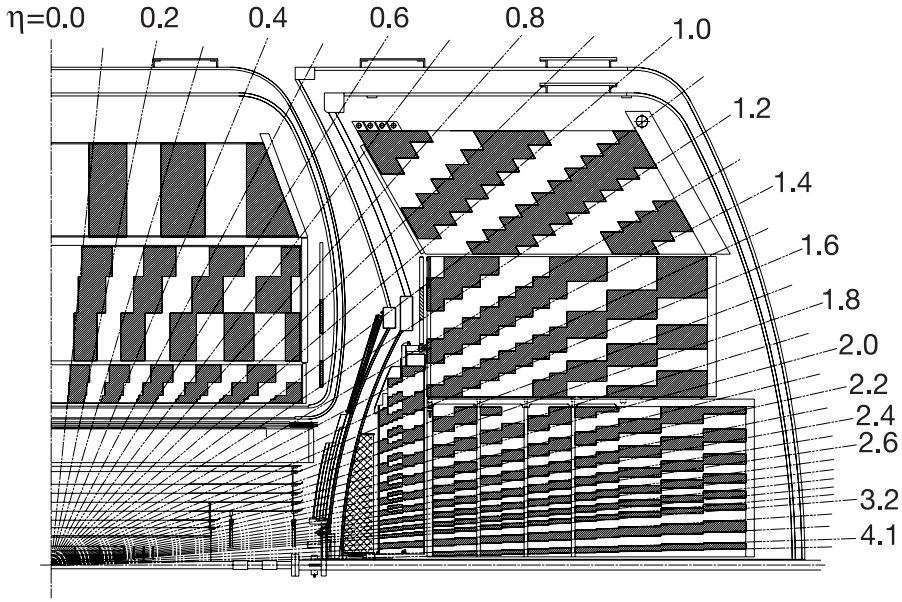

Figure 2.10: Cross section of one quarter of the calorimeter showing the coverage in pseudo-rapidity. The shading pattern indicates groups of cells connected into towers.

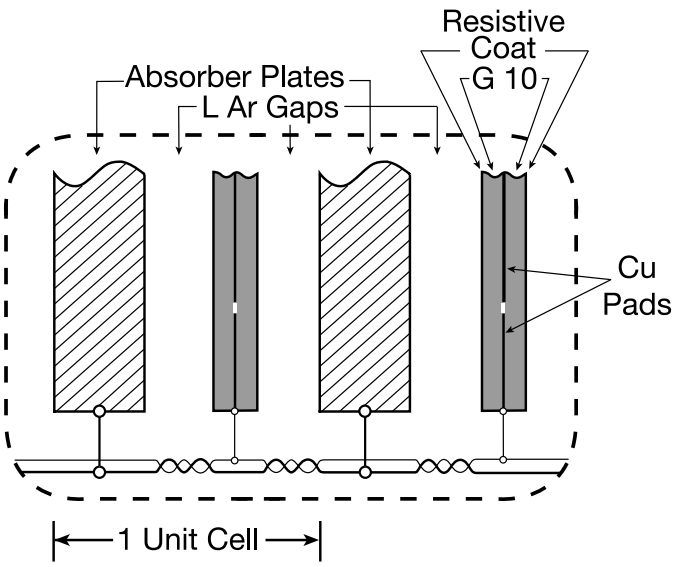

Figure 2.11: Schematic diagram of individual calorimeter cell with liquid argon filled gaps and signal board unit.

the calorimeter cells, $\eta_{\text{det}} \times \phi \approx 0.1 \times 0.1$ rad. Readout cells called massless gaps are also added inside the CC and EC cryostats to supply information lost due to

unsamples materials.

2.2.4 Muon System

Most of the particles are captured by the calorimeter except for the muons and the neutrinos. Neutrinos cannot be detected due to the tiny interaction cross section. The most outer detector is therefore designed to identify muons. The muon detector [50] consists of three parts: the central muon system covering $|\eta_{\mathrm{det}}| < 1$, the forward muon system covering $1 < |\eta_{\mathrm{det}}| < 2$, and the toroidal magnet of 1.8 T magnetic field. Both of the muon systems use wire drift tubes and scintillation counters. The drift tubes are arranged in three layers, where layer A is located between the calorimeter and the toroidal magnet, and layers B and C are outside the magnet. The drift tubes are made of rectangular aluminum tubes, filled with a gas mixture. Each tube has an anode wire at the center, which gives an information on position of the muon trajectory, and vernier cathode pads positioned above and below the anode. When a charged particle passes through the tube, the gas is ionized and electrons liberated by the ionization drift toward the anode. The drift time and charge deposition are recorded and used to determine the position of the deposited ionization from the passing particle.

The central muon detector is instrumented with proportional drift tubes (PDTs) as shown in Figure 2.12. The PDTs contain a gas mixture of 84% argon, 8% methane, and 8% CF4, which was optimized for faster drift times of the high instantaneous-luminosity environment of Run II. Because the drift time of the PDTs, 750 ns, is still longer than the bunch crossing time at the Tevatron, two additional layers of scintillators, the A-ϕ scintillators (situated between the calorimeter and the layer A) and the Cosmic Cap scintillators (located outside the layer C) shown in Figure 2.13, are used to trigger muon events and reject cosmic muons. Furthermore, the A-ϕ scintillators are also used to reject any other particles that emerge from the calorimeter. The coverage of the bottom scintillators is reduced because the detector has a support from the ground.

The forward muon detector is instrumented with mini drift tubes (MDTs) and scintillation counters. The drift time of the MDTs is only 60 ns and the scintillators are also used to trigger on muon events and to reject cosmic muons and other backgrounds.

The toroidal magnet provides the momentum measurement, with trajectories always bending in the (r, z) plane of the muon systems. This offers better matching to central tracks and helps reject muons from π or K decays. The external muon system also helps to improve the momentum resolution for high momentum muons detected in the central tracker. Figure 2.14 shows a schematic view of the whole muon system.

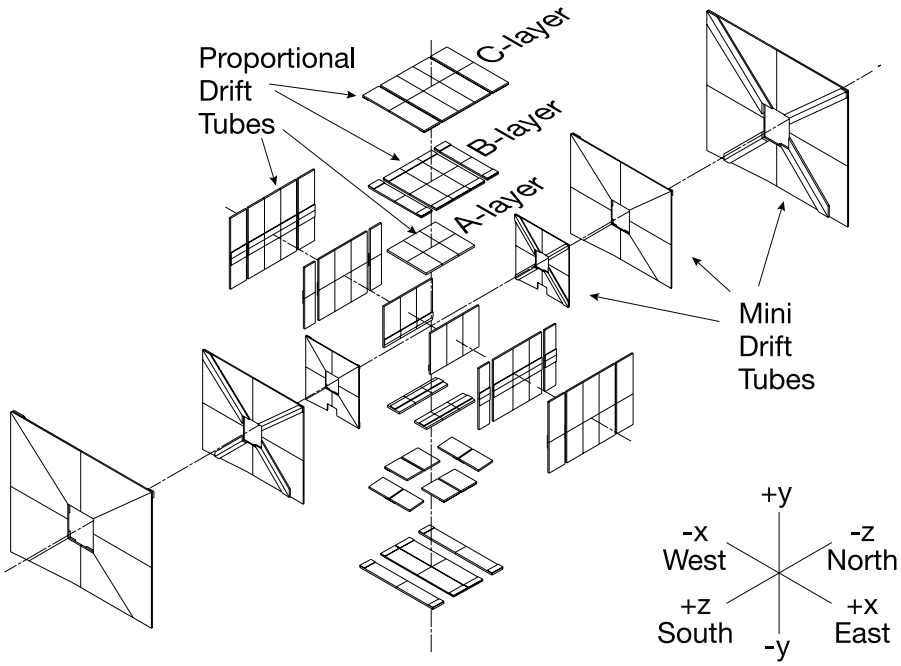

Figure 2.12: Schematic view of the DØ muon drift tube system.

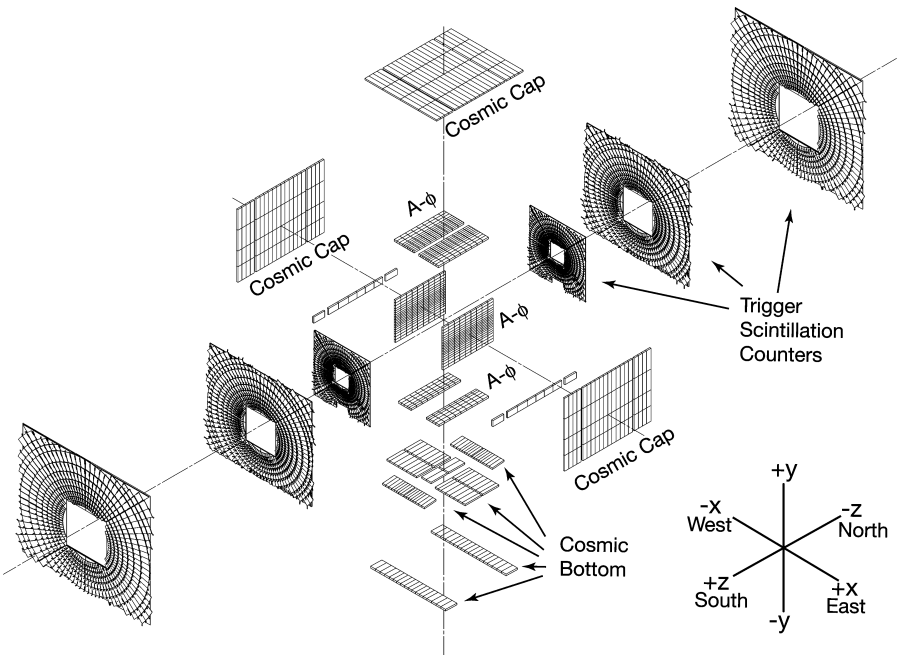

Figure 2.13: Schematic view of the DØ muon scintillation system.

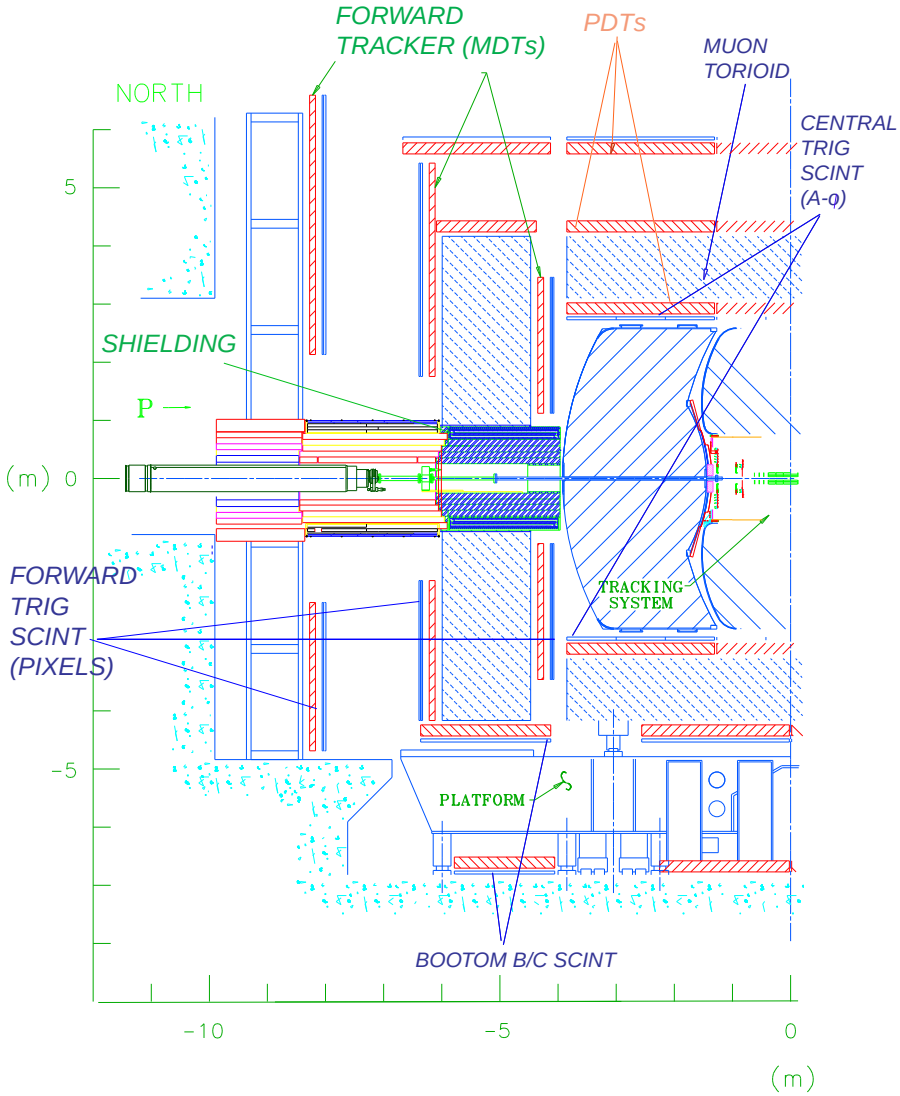

Figure 2.14: Schematic view of the left part of the DØ muon system.

2.2.5 Luminosity Monitor

The luminosity monitor (LM) determines the Tevatron luminosity at the DØ detector by detecting inelastic $p\overline{p}$ collisions. The cross section for these collisions is dominated by soft processes, where no high p_T particles are produced. The monitor also measures beam halo rates and makes a fast measurements of the z coordinate of the interaction vertex. The two luminosity monitors are located at $z = 140\,\text{cm}$ and $z = -140\,\text{cm}$ relative to the center of the detector. The LM are located close to the beam pipe and cover the range of $2.4 < |\eta_{\text{det}}| < 4.4$ as shown in Figure 2.15. Each LM consists of an array of 24 plastic scintillation counters, and the light from the scintillating medium is recorded using photomultiplier tubes (PMTs). They

cover region of $2.7 < |\eta_{\text{det}}| < 4.4$. To distinguish the $p\overline{p}$ interactions from collisions in the beam halo, the z coordinate of the interaction vertex is calculated from the difference in time-of-flight between the $+z$ and $-z$ luminosity monitors. Particles produced from the $p\overline{p}$ interactions have smaller time-of-flight difference than those from the beam halo. The overall uncertainty on the integrated luminosity is 4.3% in Run IIb and 6.1% in Run IIa.

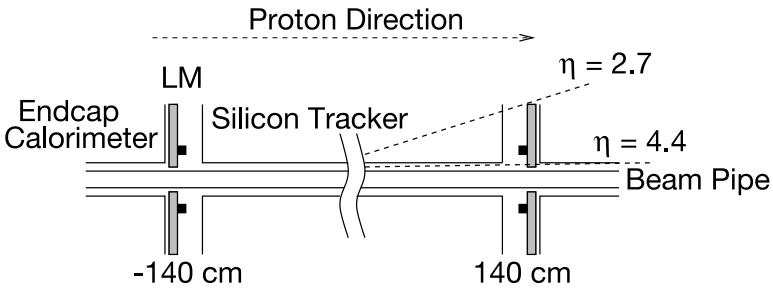

Figure 2.15: Schematic drawing of the DØ luminosity monitors.

2.2.6 Trigger System

In the Tevatron, the bunches are divided into three groups, where collisions happen every 396 ns, with distance between the groups of 7 μs. That translates into initial data rate is approximately 1.7 MHz, meaning 1.7 million interactions take place every second. If a typical event contains $\approx$ 250 kB of data, it means there is 425 GB of data to record every second. This is technically impossible and in addition, we are only interested in inelastic physics events such as $t\overline{t}$ pair events which are only a small fraction of all events. It is necessary to have a trigger system which is able to reduce the data rate to about 50-200 Hz. DØ uses trigger system consisting of three sequential levels and each following level explores events with more detailed patterns and sophisticated algorithms. The first in the chain is Level 1 (L1) trigger which is comprised of pure hardware with an accept rate of 2 kHz. L1 utilizes electronic signals from multiple detectors to execute initial selection of events. Level 2 (L2) trigger is a mixture of hardware and software that use individual reconstructed objects and their correlations for trigger decisions. L2 provides an accept rate of 1 kHz. Events passed L1 and L2 are sent to the pure software based Level 3 (L3) trigger for final decision making. The L3 accept rate is reduced up to 50 Hz due to sophisticated algorithms. The L3 output rate changes from 200 to 50 Hz depending on the instantaneous luminosity. The software package COOR is installed on an online host to coordinate and control DØ triggering. An overview of the DØ trigger and data acquisition system can be seen in Figure 2.16.

As the first stage, L1 trigger faces a pool of numerous events and needs to make very fast decisions for each bunch crossing. It consists of calorimeter (L1Cal), central track (L1CTT), muon system (L1Muon), and forward proton detector (L1FPD)

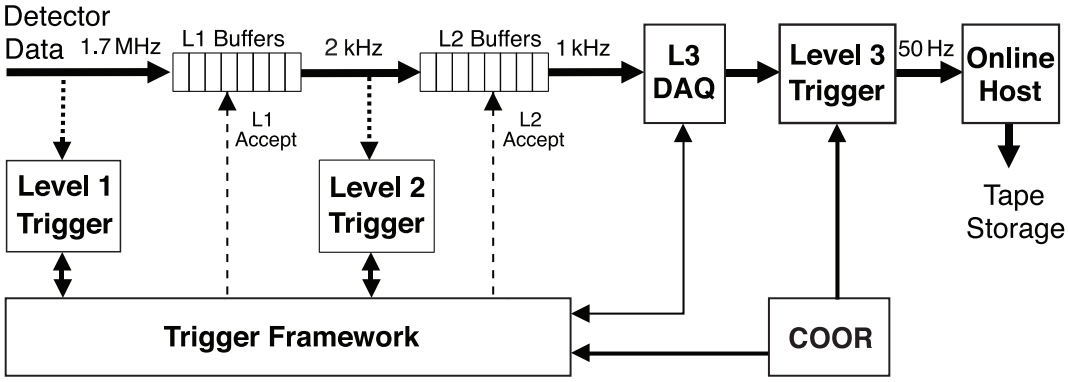

Figure 2.16: Overview of the DØ trigger and data acquisition systems.

triggers. The Level 1 trigger framework coordinates timing of L1 detector triggers. Each subsystem looks at their detector readout and sets detector-specific trigger terms, e.g. electrons, photons, jets, and $\not\!\!E_T$ in L1Cal. These terms are taken up by the trigger framework to make trigger decisions. The L1 trigger decision time is 3.5 µs or less. Accepted events are passed on to L2.

The L2 trigger system consists of two stages: the preprocessor (hardware) stage and the global (software) stage. The preprocessor stage includes the Level 2 calorimeter (L2Cal), the preshower detector (L2PS), the muon system (L2Muon), the SMT (L2STT), and the Level 2 central track (L2CTT) triggers. In this stage, the L2 preprocessors collect information from the front-ends and L1 trigger system to analyze and form physics objects. L2Cal constructs primitive electrons, photons and jets with clustering algorithms. Event missing transverse momentum $\not\!\!E_T$ is also determined based on the imbalance of trigger tower energies. L1CTT tracks are further processed in L2CTT using transverse momentum. The L2Muon imports L1Muon candidates to improve the muon quality using timing data. In the global stage, a global processor (L2Global) selects events based on the identified objects formed in a previous stage and a certain selection criteria to make a decision. The L2 trigger decision time is ≈ 100 µs.

The L3 trigger is a fully programmable software based trigger system running in a farm of parallel computers to further select L2 events based on the reconstructed physics objects and their correlation. The L2 objects receive a more sophisticated reconstruction and more complicated algorithms are applied for event filtering, like the b-tagging probability. The reconstruction is done in 25 ms for each event. This results in the data rate reduced from 1 kHz to 50 Hz which is synchronized with the pace of tape recording. The objects passing L3 trigger have quality information in their definition and reconstruction and are finally recorded on the tape for an offline analysis.

2.3 Author notes

I have neither designed nor built the DØ detector or the Tevatron accelerator. In this chapter, I only describe the technical aspects of the tools used in my analysis. And it is important to stress out that my work would not be possible without the many great achievements of the DØ collaboration and the accelerator division in Fermilab in designing, building, and operating such tremendous technology for this very long time.

I have taken series of shifts in the control room, trying to secure smooth data taking for calorimeter and muon part of the DØ detector, until September 2011 when the Tevatron collider was shut down for good. In total, I have done 50 shifts in the control room, i.e. 400 hours underground, watching protons and antiprotons to collide and keeping our systems fully functional to take as much good data as possible. I remember those times with a great joy as I met many amazing people during my shifts and learned a lot about the detector. Bill Lee, who recently passed away, and George Ginther to name at least two that were almost always around and knew everything about the detector.

The pictures and schematics used in Section 2.2 are used from the DØ picture gallery. I am not using a direct citation here as I think it is not necessary due to the fact that I am member of the DØ collaboration and some of the pages of the gallery are no longer online. I thank here to all authors of these pictures and schematics, mainly by Abid Patwa and Ann Heinson.

Chapter 3
Object Reconstruction and Identification

The DØ trigger system, described in Section 2.2.6, is applied to store on a tape the interesting and high-p_T events. These recorded events are raw data that corresponds to bits of electric signal collected when the particles interact with the detector. The goal is to obtain objects that can be used in the analysis. This process is a reconstruction of the recorded events, where the software finds hits in the subdetectors, reconstructs tracks in the central tracker and clusters in the calorimeter, and combines them into a form of physical objects. In this chapter, the reconstruction and identification of objects in the recorded raw data is described. The objects are tracks, track vertices, and objects that are present in the top quark decay: electrons, muons, jets, b quark jets, and energy imbalance left by undetected neutrinos.

3.1 Tracks

Tracks are made up of the deposits of charge left behind as charged particles propagate through the layers of the tracker. Tracks are used for object identification, such as differentiating between photons and electrons (they look the same in the calorimeter), and for measuring the momentum of particles. Trajectories are bent by the magnetic field of the solenoid and hits are left in the SMT or CFT. The hits from the tracking system are formed into clusters, which are fed into a pattern recognition software to search for tracks. Two algorithms are applied sequentially to reconstruct track trajectories from these hits:

The **Alternative Algorithm** (AA) starts with a combination of three or more hits to preselect the initial track candidates. Each track candidate is extrapolated and associated with additional hits found in the next SMT or CFT layer once they satisfy certain requirements, e.g. the χ^2 should be within a specified threshold level for each hit added to the algorithm. Once the criteria is not fulfilled with the new hits, the original track hypothesis is split and new tracks are formed.

The Histogram Track Finding Algorithm (HTF) [51] uses three parameters to characterize each track in the transverse plane: the track curvature ρ, the distance of the closest approach (DCA) to the origin, d_0, and the azimuthal angle

to the center of the track projection, ϕ. Each pair of hits from track candidates produces a 2-D histogram with respect to a point in the (ρ, ϕ) space. These hits can be described by a straight line in the (ρ, ϕ) space. Each intersection of the lines corresponds to a track candidate.

The track candidates are passed to a track fitter based on the Kalman Filter algorithm [52]. This fitter contains a detailed map of the magnetic field and the material in the detector and using track candidates from the previous algorithm, it finds tracks throughout the entire tracking system and reconstructs the final track parameters. How the track is built inside the CFT tracker was shown in the previous Chapter in Figure 2.8.

Tracks are not considered as individual objects and take part in the identification and reconstruction of other objects like electron, muon, and jets. Different criteria are applied on the properties of the track candidates afterwards, depending on the object.

3.2 Vertex Reconstruction

Primary vertex (PV) is a name for the point where a $p\bar{p}$ collision takes place. The average number of collisions per crossing of bunch of protons and anti-protons is usually only about two, but can be higher in runs with a higher initial luminosity. The goal of the primary vertex construction is to distinguish an interesting physics event, such as $t\bar{t}$ production, that caused the trigger to fire from the other collisions during the same bunch crossing, known as the underlying events or minimum bias interactions. Locating precisely the primary vertex is useful for rejecting backgrounds, for the identification of $\not{E}_T$ and for the identification of long living particles like B hadrons.

At DØ, primary vertices are reconstructed using an adaptive primary vertex algorithm [53]. The first step is to select tracks with $p_T > 0.5\,\text{GeV}$ and two or more hits in the SMT. The z-clustering algorithm is applied to tracks within 2 cm in z axis to form vertex clusters. The common vertices are built with the Kalman Filter vertex fitting algorithm [52], which repeatedly removes the track with the highest χ^2 contribution to the vertex until the total χ^2 per degree of freedom is smaller than 10. Among the remaining tracks, only the ones whose closest distances in (x, y) plane are within 5 standard deviations of the beam spot calculated in the previous step are further selected. Uncertainties of the selected tracks are reweighted according to their χ^2 distributions by:

$$w_i = \frac{1}{1 + e^{\frac{\chi_i^2 - \chi_{\text{cutoff}}^2}{2T}}}, \tag{3.1}$$

where χ_i^2 is the χ^2 contribution from the ith track, χ_{cutoff}^2 is a cutoff constant where the weight function drops to 0.5, and T is the parameter that controls the sharpness of the function. The Kalman Filter fitter is used iteratively until it converges, i.e.

meet the requirement $|w_i - w_{i-1}| < 1 \times 10^{-4}$. Tracks with weights $w_i < 1 \times 10^{-6}$ are excluded from the fitting iteration.

The next step is to distinguish the hard-scattering vertices from the minimum bias vertices. For that, the transverse momenta of the tracks at each vertex are used in a probabilistic approach [54]. Each track is assigned a probability of originating from a minimum bias vertex as these events event tend to have a lower p_T. Then the vertex minimum bias probability is calculated by multiplying the minimum bias probability from all contributing tracks. The vertex with the lowest minimum bias probability will be selected as the primary vertex.

Due to the fact that heavy hadrons can travel up to several millimeters in the detector, a **secondary vertex** can be reconstructed and used in identifying b quark jets and heavy hadrons. The reconstruction procedure involves the track jet reconstruction, the track selection, the vertex finding and the final vertex selection [55]. The secondary vertex reconstructed from the track jets is independent of the calorimeter reconstruction. The track clustering again applies the z-clustering algorithm. The tracks are added in decreasing order of p_T and the requirements include > 1 SMT hits, $p_T > 0.5\,\text{GeV}$, the distance of the closest approach to the nearest vertex DCA $< 0.2\,\text{cm}$, and $Z_{\text{DCA}} < 0.4\,\text{cm}$. The cone algorithm with parameter 0.5 is used to form track jets in each cluster. Tracks with $\text{DCA}/\sigma_{\text{DCA}} > 3$ are selected, where σ_{DCA} is the uncertainty of DCA. Unlike primary vertex, the Kalman Filter algorithm is employed to reconstruct secondary vertex for track jets with at least two tracking selected by the $\text{DCA}/\sigma_{\text{DCA}}$ requirement. It starts by fitting all combinations of track pairs in the track jet to reconstruct a seed vertex. Each seed vertex is joined with additional tracks until χ^2 is beyond a certain threshold or no more tracks are available. Sharing tracks are allowed between reconstructed vertices, while for b quark tagging it is avoided by algorithms in the Neural Network b-tagger, which will be explained later.

3.3 Electrons

The objects registered in the EM part of the calorimeter in the form of showers are generally EM objects, electrons and photons [57]. The differentiation between an electron and photon is very simple as only electrons leave tracks in the central tracking system and the shower development in the calorimeter is different[1]. Photons are not used in this analysis, but they are important as they are considered to be the main background for electrons, $\gamma \to e^+e^-$, together with $\pi_0 \to \gamma\gamma$ decay with small contribution of charged pions decays and the fluctuation in hadronic showers.

The electron reconstruction starts with information from the calorimeter - the EM tower is defined by adding the energies measured in a section of 0.1×0.1 in

[1]The electrons shower starts with bremsstrahlung, while the photon shower begins with an electron pair production. After the showers fully develop in the calorimeter, electrons interact through the ionization and photons through the Compton scattering.

$\eta \times \phi$ occupying all four layers of the EM calorimeter and the first hadronic layer. Using a simple cone algorithm centered on an EM tower with the highest transverse energy E_T, the EM cluster is formed within radius $R = \sqrt{(\Delta\eta)^2 + (\Delta\phi)^2} = 0.2$ using adjacent towers with $E_T > 50\,\text{MeV}$. The following criteria are used:

- transverse energy of the cluster to be $E_T > 1.5\,\text{GeV}$
- at least 90% of the cluster energy must be deposited in the EM layers, i.e.

$$f_{\text{EM}} = \frac{E_{\text{EM}}}{E_{\text{tot}}} > 0.9 \tag{3.2}$$

- the EM objects are required to be isolated, meeting criterion of

$$f_{\text{iso}} = \frac{E_{\text{tot}}(R < 0.4)) - E_{\text{EM}}(R < 0.2)}{E_{\text{EM}}(R < 0.2)} < 0.2, \tag{3.3}$$

  where $E_{\text{tot}}(R < 0.4)$ is the total energy in all the towers within a cone of radius of 0.4 around the central cluster, and $E_{\text{EM}}(R < 0.2)$ is the energy in the EM calorimeter within a cone of radius 0.2.

Clusters passing the criteria above are considered as EM object candidate. The primary vertex and other information, e.g. from preshower detector, are used to calculate the 4-momentum of the particle.

The particle is considered as an electron if it is matched to track with $p_T > 1.5\,\text{GeV}$ in central tracking system within 0.05×0.05 in $\eta \times \phi$ by fulfilling that probability $p(\chi^2_{\text{spat}})$ is larger than zero, where χ^2_{spat} is defined as

$$\chi^2_{\text{spat}} = \left(\frac{\delta\phi}{\sigma_\phi}\right)^2 + \left(\frac{\delta z}{\sigma_z}\right)^2, \tag{3.4}$$

where δ_i represents the difference between the positions of the third layer of EM calorimeter and the track in variable i, σ_i is the root-mean-squares (RMS) of the experimental distributions of the corresponding quantities.

Another criteria are used to study the shape of the shower to distinguish electrons from hadronic showers. Those criteria include energy fraction, shower isolation, shower width, H-matrix technique, track isolation, track match, and "hits on the road" that are defined by a number of hits in CFT and SMT along the path from primary vertex towards the EM cluster. The similarity of the hadronic shower to an EM shower is quantified by a 8×8 (7×7 for CC) covariance matrix, so-called H-matrix [56], which is parameterized by eight correlated variables: the fraction of energy deposited in each four EM layers (4 variables that represent the shower development), total shower energy in the EM calorimeter, the z position of the primary vertex divided by its uncertainty, and the width in both dimensions of the shower in (r, ϕ) plane of the third layer of the EM calorimeter that has the finest

granularity for this measurement (only one dimension is used in CC). For clusters to be identified as EM objects, the χ^2 of the H-matrix has to satisfy $\chi^2_H < 50$.

The objects that passed all the requirements are considered to be loose electrons. Tight electrons are considered to achieve objects almost completely pure from photons and other background sources with the misidentification rate of 0.2%. The tight requirement is evaluated using various multivariate analysis (MVA) techniques that include the H-matrix method, a Likelihood method, a Neural Network (NN) method, and a Boosted Decision Tree (BDT) method [57]. BDT is the most advanced method and incorporates the previously mentioned methods. BDT uses a great number of variables that have strong discrimination for the signal and the background. These variables include tracking and calorimeter parameters, χ^2_H, DCA, track isolation calculated in $0.05 < \Delta R < 0.4$, electron likelihood, hits in SMT and CFT, and also information from CC, EC, all layers of EM, and the first layer of the fine hadronic calorimeter. The BDT is trained separately for the CC and EC, and for high and low luminosities. The output for analyzers are BDT working points that are calorimeter section and luminosity dependent, as seen in Figure 3.1 with different cuts used. The working point used in this measurement is called "emvPoint1" and cuts on the BDT output for real electrons in CC has the value of -0.22 and in EC the value of -0.74, while the fake electrons have cuts of -0.86 in both CC and EC.

3.4 Muons

Muons are not stopped in the calorimeter and the independent muon detector system, described in Section 2.2.4, is constructed to help identify muons. To reconstruct and identify muon readings from the tracking system, the calorimeter, and the muon detector are used [58]. The segments from the three layers of drift tubes are used to find tracks in the muon system. The hits from the drift tubes wires and from the three layers of scintillation counters are matched together to form a central muon track. Such objects reconstructed in the muon detector are called local muons. To identify the object as a muon candidate, it is required to match the track in the central tracking system. The muon are further identified as isolated by using the isolation criteria. The isolation is required for high-p_T physics, because the absence of significant activity around the muon trajectory, both in the calorimeter and in the central tracker is demanded.

The muon detector system provides a positive muon identification and, with enough information from all layers, also a momentum measurement. Information provided by the central tracking system allows for more precise measurement of the muon momenta. The calorimeter can independently confirm the muon identification by the signature left by a muon, unfortunately with efficiency only around 50%. Despite the relatively high amount of energy lost by a muon in the calorimeter, the energy deposit of muons in an individual cell is close to the threshold level of the calorimeter noise-suppression algorithm, and is therefore not well measured.

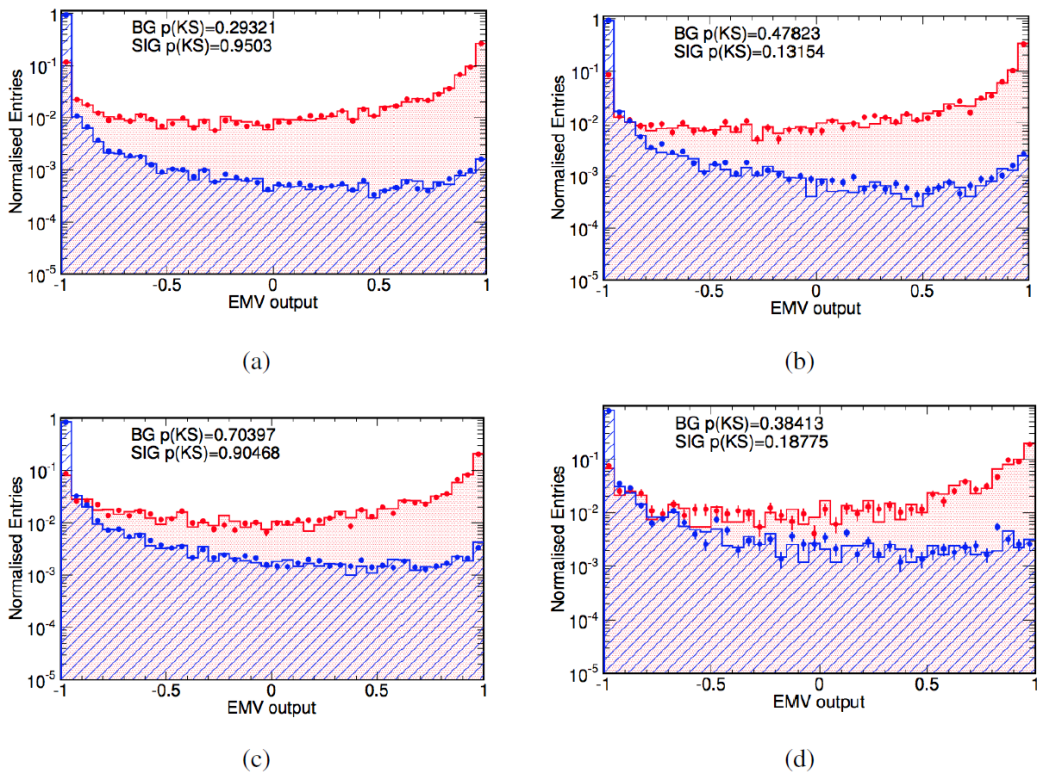

Figure 3.1: BDT method output for (a) CC electrons in low luminosity events, (b) CC electrons in high luminosity events, (c) EC electrons in low luminosity events, and (d) EC electrons in high luminosity events. Solid red distributions are from real electrons and blue from fake electrons, with the points being a testing sample.

Thus, the calorimeter information is not exploited to identify high-p_T muons that are used in this analysis.

There are three steps in the muon identification: local muons, track matched muons, and isolated muons. For each of these three steps, different identification quality categories are defined to provide several categories (or working points) defined for different usage and described in Ref. 2.2.4. Only the working points used in the selection described in Section 4.3 will be discussed here.

The local muon is required to meet the *medium* (sometimes denoted as *mediumnseg3*) criteria:

- at least one scintillator hit and at least two wire hits in the A layer of the muon system
- at least one scintillator hit in $|\eta_{\text{det}}| > 1.6$ and at least two wire hits in the BC layers
- in the case of the bottom part of the detector with the support structure for the calorimeter ($5/4\pi < \phi < 7/4\pi$ and $|\eta_{\text{det}}| < 1.6$), only one of the criteria

above is required.

The matched track has to follow the *medium* criteria defined as:

- the track distance of the closest approach to the beam axis, DCA, is $|\mathrm{DCA}| < 0.04$ cm and there are SMT hits, or the are no SMT hits and the requirement is $|\mathrm{DCA}| < 0.2\,\mathrm{cm}$
- $\chi^2/N_{\mathrm{DOF}} < 9.5$, where χ^2 is the result of the fit used for reconstruction of the track in the central tracking system and N_{DOF} is the number of degrees of freedom
- there are at least two hits in CFT.

The isolation criterium is called *TopScaledTight* and was designed to select isolated muons arising from the primary vertex and to reject secondary muons from semi-leptonic decays of b or c quarks, which are surrounded by additional particles. This is very important in high-p_T events used in the top quark measurements. The muons are required to pass

- $\Delta R(\mu, \mathrm{jet}) = \sqrt{\Delta\eta^2(\mu, \mathrm{jet}) + \Delta\phi^2(\mu, \mathrm{jet})} > 0.5$, i.e. the distance between muon and the closest jet with $p_T > 15\,\mathrm{GeV}$ in (η, ϕ) space is larger than 0.5.
- $\sum\limits_{\mathrm{tracks}\ \epsilon\ \Delta R<0.5} p_T^{\mathrm{track}}/p_T^{\mu} < 0.1$, i.e. the scalar sum of transverse momenta of all tracks inside a $\Delta R(\mu, \mathrm{track}) < 0.5$ cone around the muon track, with the exception of the muon track itself, divided by the muon transverse momenta, is smaller than the parameter 0.1.
- $\sum\limits_{\mathrm{clusters}\ \epsilon\ 0.1<\Delta R<0.4} E_T^{\mathrm{cluster}}/p_T^{\mu} < 0.1$, i.e. the scalar sum of transverse energies of all calorimeter clusters inside a hollow cone around the muon defined by $0.1 < \Delta R(\mu, \mathrm{cluster}) < 0.4$ divided by the muon transverse momenta, is smaller than the parameter 0.1.

Furthermore, to veto cosmic muons, the time of flight between the collision and hits in the layers must be less than 10 ns.

3.5 Imbalance in Transverse Momentum

The imbalance in Transverse Momentum, the Missing Transverse Energy $\not\!\!E_T$, is the estimation of the energy that is not detected in the system presumably carried away by neutrino. As the momenta of the incoming partons in the z direction in Tevatron collisions are unknown, only the imbalance in the transverse momentum in an event can be calculated, indicating the possible presence of undetected particles. Thus, instead of the conservation of momentum, the conservation of transverse momentum is used.

The calculation starts with vector sum of energy deposits in calorimeter cells in transverse plane that are above the noise threshold. Cells from the coarse hadronic part of the calorimeter are left out to reduce the noise. The value is corrected to take into account reconstructed muons, photons, electrons, and jets:

$$\vec{\not{E}}_T = -\sum_i \vec{p_i}^{\text{cell}} - \sum_j (\vec{p_j}^{\text{object}} - \sum_{k_j} \vec{p_{k_j}}^{\text{cell}}), \tag{3.5}$$

where $\vec{p_i}^{\text{cell}}$ is the energy deposited in calorimeter cell i, with the direction given by the coordinate of each cell, $\vec{p_j}^{\text{object}}$ represents the p_T of the reconstructed object j with all corrections applied, and $\vec{p_{k_j}}^{\text{cell}}$ is the original p_T in the cell k_j that belongs to a reconstructed object j. Only calorimeter cells that are not contained in any reconstructed object, including the projected energy loss along the path of the muon, are included in the computation of the fully corrected missing energy.

3.6 Jets

Jets are collimated showers of particles from the decay of a hadron originating from quarks or gluons produced at the primary vertex. The initial parton evolves around the original flight direction with particles produced by parton hadronization and gluon soft radiation. In the hadron rest frame, the particles form basically a sphere, but one needs to consider large boosts from top quarks ($m_t = 173.3\,\text{GeV}$) and W bosons ($m_W = 80.4\,\text{GeV}$) decaying to lighter particles ($< 5\,\text{GeV}$). Such boosts cause these bunches of particles to become cone-shaped. Therefore, a cone-based algorithm [59] is designed to reconstruct and identify jets.

The content of a jet is not essentially restricted to hadrons, there could be electrons, muons, photons, and other particles. Jet contents vary widely and jet shower shapes differ significantly. Jets deposit energy not only in hadronic layers of the calorimeter but also in the electromagnetic layers. The jets in $p\overline{p}$ collisions originate from hard-scattering partons, initial/final state radiation (ISR/FSR) partons and beam remnants (beam jets).

3.6.1 Jet Reconstruction

The DØ cone algorithm described in Ref. [59] has been developed further and the method used for this measurement is named the "Improved Legacy Cone Algorithm" [60]. The cone radius is defined as

$$\Delta R == \sqrt{(\Delta\eta)^2 + (\Delta\phi)^2}. \tag{3.6}$$

Similarly to an electron, the jets reconstruction takes part mainly in calorimeter. Each cell of the calorimeter, considered as massless object, has assigned 4-vector and a direction defined by the primary vertex. A reconstructed tower is built from

each 0.1×0.1 in the $\eta \times \phi$ space with all cells above noise threshold. The sum of 4-momenta in all cells in a tower gives the 4-momentum for the tower $\vec{p}_{\text{tower}}$. Towers are listed by p_T order. The cone algorithm consists of three steps:

- In the first step, calorimeter towers are preclustered by the Simple Cone Algorithm. All towers with $p_T^{\text{tower}} > 500\,\text{MeV}$ are selected and grouped with surrounding towers in a cone of radius $\Delta R = 0.3$. All clustered towers are removed from the list and the procedure continues iteratively until all towers are clustered. Onle preclustered towers with $p_T^{\text{precluster}} > 1\,\text{GeV}$, or at least two towers, are passed on to the next step.

- In the second step, the p_T-ordered preclusters are used as seeds for creating protojets. The protojet is built from the preclusters with the highest $p_T^{\text{precluster}}$ from the list, but this time using cone of radius $\Delta R = 0.5$. The cone center is recalculated iteratively with each added precluster within the cone until all the jet centers are found and stable.

- In the final step, protojets are merged and split to check for overlapping and double-counting. Each pair of the protojets with the distance in R larger than the cone size but smaller than twice of the cone size are processed. If the energy shared by two adjacent protojets is more than 50%, the two jets are merged to form a new protojet. If the overlapping energy is less than 50% the two jets are split by assigning the preclusters to the closest of the two protojets in $\eta \times \phi$ space. The merging/splitting process repeats until all jets are stable and do not overlap with each other. Objects acquired with this procedure are considered jet candidates if their $p_T > 6\,\text{GeV}$.

3.6.2 Jet Identification

The jet candidates from the jet reconstruction are qualified for the identification to remove fake jets that arise mainly from the noise in the calorimeter and are considered unphysical. To do so, set of requirements is applied:

- The fraction f_{EM} of the energy in the EM calorimeter must be greater than 5%. In addition, it must be less than 95% to different jets from EM objects. This is done to discriminate EM objects and jets and suppress the noise.

- The fraction of energy f_{CH} in the coarse hadronic calorimeter must be: less than 40% in the central calorimeter and less than 46% in the end calorimeters.

- The jet must be confirmed by the Level 1 trigger:

$$R_{\text{L1}} = \frac{p_T^{\text{L1}}}{p_T^{\text{non-CHjet}}} > 0.5, \tag{3.7}$$

  where p_T^{L1} is the sum of the scalar transverse momenta from the 100 hottest L1 towers in a cone of $\Delta R < 0.5$ around the jet, and $p_T^{\text{non-CHjet}}$ is the vector

p_T sum over all reconstructed towers assigned to the jet, excluding the coarse hadronic calorimeter.

- Additionally in the Run IIb, at least two tracks within the cone of the jet that are associated with the primary vertex. This is known as the jet vertex confirmation requirement.

The jet evolution in the DØ detector is shown in Figure 3.2.

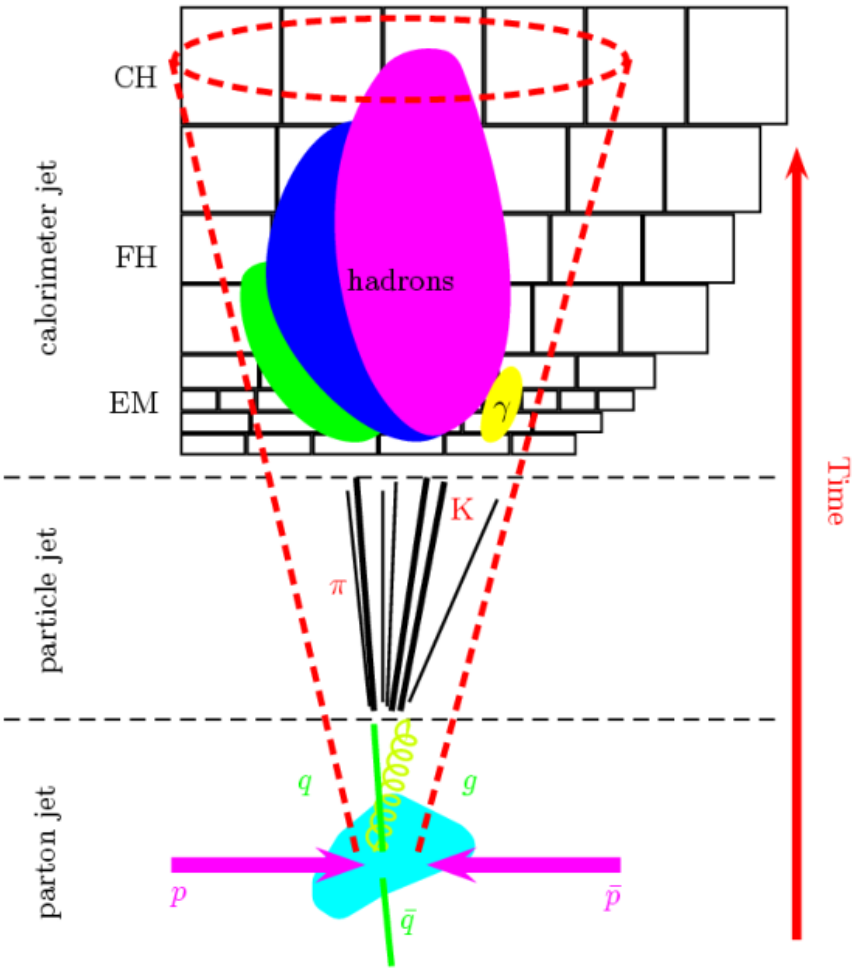

Figure 3.2: Visualization of the jet evolution in the DØ detector from the original parton [62].

3.6.3 Identification of b quark jets

The identification of b quark jets is very important in the top quark pair decay as two or three b quarks are present, while background processes are more likely

to produce light quark jets instead of b quark jets. Hence, identifying jets that originate from b quarks, a procedure known as b-tagging [61], significantly reduces background. The b-tagging algorithm distinguishes b jets from light-flavored jets (originated from light-flavor quarks and gluons) by utilizing the fact that b quark hadrons have a longer lifetime and therefore can travel several millimeters before decaying. This often implies the presence of tracks with origins displaced from the primary vertex. Therefore the b jet identification relies on the reconstruction of a secondary vertex with a large transverse impact parameter.

First, the "taggability" of a jet is investigated. The b-tagging involves only tracking and vertex information, so taggability ensures that there is enough information to begin with and that the procedure is less dependent on possible variations of the tracking system efficiency. A calorimeter jet is **taggable** if it is matched to at least two tracks within a cone of radius $R = 0.5$ with the origin set along the jet axis. The reconstructed tracks are required to have at least one hit in the SMT and at least six hits in the CFT, to have $p_T^{\mathrm{trk}} > 0.5\,\mathrm{GeV}$, to have DCA$< 4\,\mathrm{mm}$ along the z axis and DCA$< 2\,\mathrm{mm}$ in the transverse plane. Around 90% jets with $p_t > 20\,\mathrm{GeV}$ is classified as taggable.

The taggable jets then undergo the V^0 rejection procedure. Neutral hadrons containing strange quarks (V^0) have decay signatures similar to those of b hadrons. In particular, K_S and Λ hadrons as they have similar lifetimes. To suppress this background, secondary vertices with two oppositely charged tracks are rejected with the following criteria: (1) the z projection of each track has DCA$< 1\,\mathrm{cm}$, (2) DCA/σDCA > 3, (3) the tracks associated with the V^0 candidate must have DCA$< 200\,\mu\mathrm{m}$, and (4) the invariant mass of the two tracks must be outside the mass range expected from K_S or Λ.

In the past, DØ used three algorithms to identify b jets: Counting Signed Impact Parameters (CSIP), Jet Lifetime Impact Parameter (JLIP) and Secondary Vertex Tagger (SVT) [61]. These tools were further combined in neural network (NN) algorithm and now replaced by algorithm called MVA$_{bl}$, standing for a multivariate analysis that discriminates between b quarks and light jets [61]. This advanced algorithm implements input variables from the previous methods.

The MVA$_{bl}$ algorithm uses simulated di-b jet signal events and di-light jet background events. The list of input variables has been extended to achieve better results to 9 variables from the impact parameter and 29 secondary vertex variables. These variables are used to train six random forests (RF) using the ROOT TMVA [63] framework. One of the RF is trained using the impact parameter from the CSIP and JLIP algorithms. The other five RFs use each set of secondary vertex variables from the five different SVT algorithms configurations. The combination of the six RFs is performed using a NN implementation, which produces the MVA$_{bl}$ output using nonlinear correlations between the inputs.

The performance and efficiency of the MVA$_{bl}$ algorithm is shown in Figure 3.3 using the simulation samples. Different operating points, defined as cuts on the MVA$_{bl}$ output, are shown in the Figure as blue vertical lines. This analysis uses L4

operating point, $\mathrm{MVA}_{bl} > 0.035$, which is shown as third line from the left.

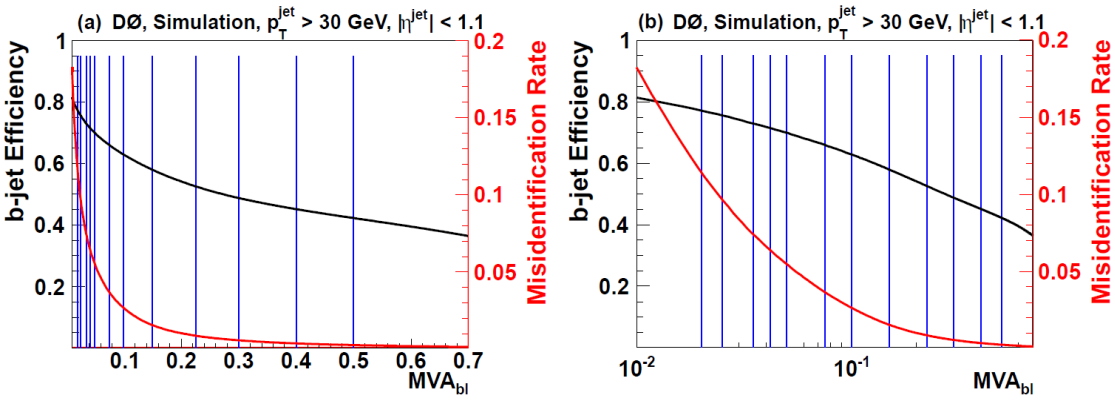

Figure 3.3: The efficiency for selecting a b jet and the light jet misidentification rate as a function of the MVA_{bl} requirement as determined in simulations. The vertical lines correspond to the selected operating points with (a) linear and (b) logarithmic scales. Source: [61]

3.7 Jet Energy Calibration

The jet energy measured by the detector is not the same as the energy of the particles that decay into the jet, due to imperfect detector response or due to the physics effects. This is illustrated in Figure 3.2. The physics effects include soft gluon radiation (ISR/FSR), fragmentation, and color reconnection and they are treated separately in the systematic uncertainties evaluation, as will be discussed in Section 5.4. Imperfect detector response and experimental configuration include the response due to detector nonlinearity, uninstrumented regions, energy deposition in the liquid argon from uranium decays. There are effects in reconstruction and resolution of the jet. A set of correction is employed and globally recognized as Jet Energy Scale (JES). The goal of this correction is to obtain the corrected jet energy that on average is equal to the energy of a particle jet, which is defined as the particles produced inside a jet cone by the primary $p\overline{p}$ interaction. Particles before entering the calorimeter are referred to as the "particle level", while particles identified and measured in the detector are called as "reconstructed level" or "detector level" as shown in Figure 3.2. The DØ jet energy calibration is built with the aim to get the data/MC ratio to 1 after all calibrations. The DØ JES correction is evaluated from the γ+jet sample and extrapolated to high energy region using dijet sample and the detailed description can be found in Ref. [64].

The set of corrections in the standard jet energy scale can be expressed as

$$E_{\text{jet}}^{\text{corr}} = \frac{(E_{\text{jet}}^{\text{meas}} - E_{\text{O}})k_{\text{O}}}{Rk_{\text{R}}S} \cdot F_{\text{corr}}, \tag{3.8}$$

where $E_{\text{jet}}^{\text{corr}}$ represents the corrected energy of the jet with the measured energy $E_{\text{jet}}^{\text{meas}}$ and the following list of correction factors:

- E_{O} is the offset energy with contributions from electronics noise, radioactive decay of the uranium absorber, and "pile-up" defined as additional $p\overline{p}$ interactions in time and those from previous crossings. E_{O} depends on the jet cone radius (R_{cone}), η_{det}, number of reconstructed primary vertices (nPV), and $\mathcal{L}_{\text{inst}}$.
- k_{O} represents correction for a bias introduced by the offset energy E_{O} determination.
- R represents the response of the calorimeter to the energy of particles comprising the jets and it is a function of jet energy and η_{det}. This is important particularly for the ICR region as it is poorly sampled with large variations in energy.
- k_{R} is the correction to bias from the detector response R determination.
- S stands for corrections for the showering of particles in the detector and for the migration of energy in and out of the finite R_{cone} and calorimeter cell size. Apart from true energy deposit outside the cone, energy may be deposited in cells inside this boundary that originated from particles that do not belong to the particle jet (e.g., due to showering effects in the calorimeter, or to the magnetic field changing the direction of particles outside of the jet cone). It depends strongly on R_{cone} and η_{det}, and only mildly on the jet energy.
- F_{corr} is a flavor dependent correction based on single particle response in the calorimeter and therefore correcting for the particle composition in a jet to bring data and MC into agreement. This is described in Section 3.7.1.

The factors E_{O}, R, and S can be defined as true corrections. Hovewer, the definitions of true correction factors, in Ref. [64], are only possible with some assumptions, like no multiple interactions or pile-up are present, or if the jets are produced only through the hard $p\overline{p}$ interaction. In practice, E_{O}, R, and S, that we measure and use in the final JES, represent only the estimators of the true corrections and may be affected by a number of biases resulting in several % difference in energy. To correct for these biases, factors k_{O} and k_{R} are introduced to ensure that the mean particle jet energy is recovered. Factor S is *a priori* an unbiased estimator of the true showering correction, and no bias correction is required. Corrected energy $E_{\text{jet}}^{\text{corr}}$ is obtained by using average values for all quantities mentioned above and provides, on average, the unbiased energy of the particle jet.

The offset correction, E_{O}, is measured from the energy in the calorimeter from *minimum-bias* (MB) and *zero-bias* (ZB) events. The MB events are collected using a trigger that requires only hits in the luminosity monitor, meaning the presence of a $p\overline{p}$ inelastic collision. The MB sample is dominated by soft interactions and is used to estimate the contribution from multiple $p\overline{p}$ interactions to the offset energy. The ZB events are collected during beam crossings without any trigger requirement. This sample represents an unbiased measurement of the energy in the calorimeter regardless of the nature of the $p\overline{p}$ interaction. Multiple interactions are removed by rejecting events with hits on both sides of the luminosity monitors (LM veto). The reconstructed $p\overline{p}$ collision vertices are used to estimate the contribution from noise and pile-up to the offset energy. This correction is usually up to 10 GeV, but this estimated correction can differ from the true offset. Corrections for this effect are estimated in MC to be 1 – 5% and are implemented in the k_{O} correction. This factor is estimated by comparing the measured energy of the leading jet from the same high-p_T one photon and one jet (γ+jets) events with and without offset energy added:

$$k_{\mathrm{O}}^{\mathrm{ZS}} = \frac{E_{\mathrm{meas}}^{\mathrm{noZB}}}{E_{\mathrm{meas}} - E_{\mathrm{O}}}. \tag{3.9}$$

The response correction, R, is numerically the largest correction in the jet energy scale calibration procedure. It accounts for various sizable effects: particles emerging from the hard scattering interact with the material before the calorimeter and lose a fraction of their energy; charged particles are deflected in the magnetic field and, in some cases, can fail to reach the calorimeter; DØ calorimeter has a higher and more linear response to electromagnetic particles than to hadrons (that is nearly logarithmic); zero suppression can also significantly contribute to the non-linearity of the response to hadrons; calorimeter module-to-module inhomogeneities and poorly instrumented regions (ICR). Some of these effects (mainly response to hadrons) is not modeled accurately in MC simulations resulting in MC and data to have different responses. To measure the response in data, the Missing E_T Projection Fraction (MPF) method [65] has been developed. The schema of MPF is shown in Figure 3.4 for γ+jets events. The method utilizes the two-body process X+jet to measure the response of jets, where X can be photon, Z, or any jet, i.e. a well-measured object referred to as the *tag object*, while the jet is *probe object*. In the transverse plane, the momentum conservation at the particle level requires the tag object $p_{T,\mathrm{tag}}$ and of the hadronic recoil $p_{T,\mathrm{recoil}}$, to be balanced:

$$\vec{p}_{T,\mathrm{tag}} + \vec{p}_{T,\mathrm{recoil}} = 0. \tag{3.10}$$

Therefore, the MPF estimates the calorimeter response of the probe jet relative to the response of the know tagged object.

Since the response of the tag object (R_{tag}) and of the hadronic recoil (R_{recoil}) might be different due to experimental effects, there can be an imbalance in their measured transverse momenta

$$\vec{p}_{T,\mathrm{tag}}^{\mathrm{meas}} + \vec{p}_{T,\mathrm{recoil}}^{\mathrm{meas}} = -\vec{\not{E}}_T^{\mathrm{meas}}, \tag{3.11}$$

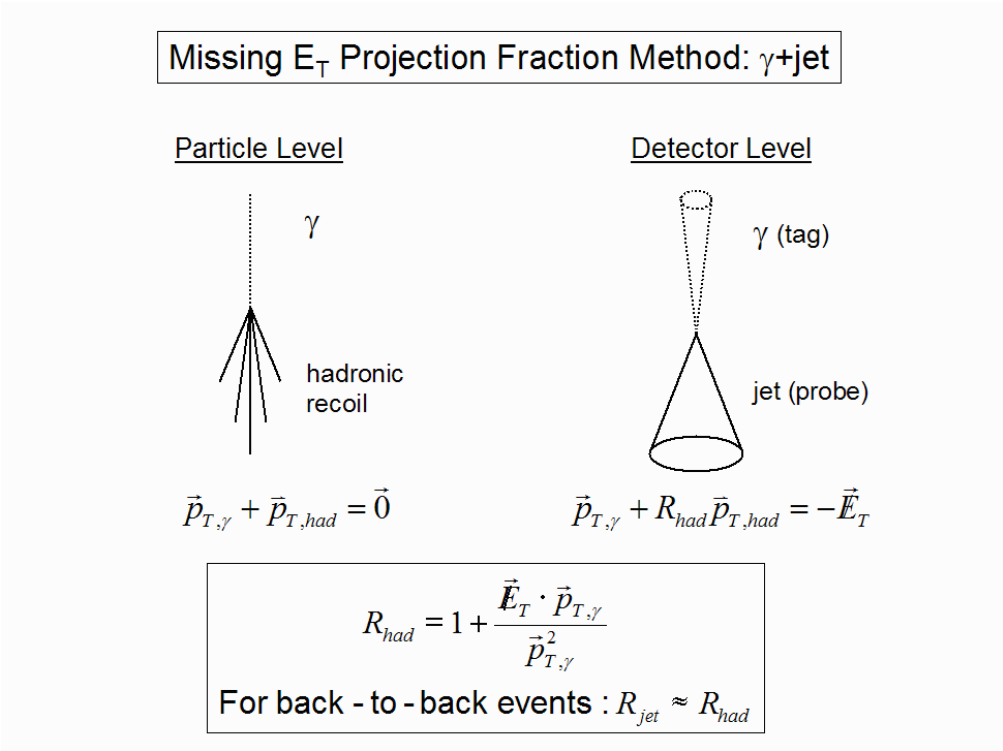

Figure 3.4: Illustration of MPF correction in γ+jet events at the particle level and detector level [62].

where $\vec{p}^{\,i}_{T,\mathrm{tag}} = R_i \vec{p}_{T,i}$ is the measured transverse momentum of the object and $\vec{\not{E}}_T^{\mathrm{meas}}$ is the measured missing E_T of the event.

The combination of Eq. (3.10) and Eq. (3.11) is

$$\frac{R_{\mathrm{recoil}}}{R_{\mathrm{tag}}} = 1 + \frac{\vec{\not{E}}_T^{\mathrm{meas}} \cdot \vec{n}_{T,\mathrm{tag}}}{\vec{p}^{\,\mathrm{meas}}_{T,\mathrm{tag}}}, \tag{3.12}$$

which shows that the ratio of responses between the hadronic recoil and the tag object can be estimated from the projection of $\not{E}_T$ onto the tag object direction in the transverse plane $\vec{n}_{T,\mathrm{tag}}$ and $\vec{p}^{\,\mathrm{meas}}_{T,\mathrm{tag}}$. Ideally, the probe jet and the hadronic recoil are identical. To improve this relation, exactly two back-to-back objects are required, i.e. no additional jets are present in the event.

Since photons are well-measured and their response can be considered unitary after correction to the particle level, the γ+jet events are used to measure the response to jets:

$$R_{\mathrm{MPF}}^{\gamma^{\mathrm{meas}}+\mathrm{jet}} = 1 + \frac{\vec{\not{E}}_T^{\mathrm{meas}} \cdot \vec{n}_{T\gamma}}{\vec{p}^{\,\mathrm{meas}}_{T,\gamma}}. \tag{3.13}$$

The jet response depends on both jet energy and η_{det}. To minimize effects from the poor jet energy resolution, E' is used instead of the measured energy:

$$E' = \vec{p}^{\,\mathrm{meas}}_{T\gamma} \cosh(\eta_{\mathrm{jet}}), \tag{3.14}$$

where η_{jet} is the jet pseudorapidity with respect to the reconstructed event primary vertex. Since the photon energy and the jet η are more precisely measured quantities than the jet energy, E' is a more precise estimator for the particle level jet.

The MPF method is applied both in data and MC. Applying the method to MC, where the true jet response is known, allows the evaluation of the biases of the method and the development of a suitable correction to data. The response is an absolute correction in the CC, $|\eta_{\text{det}}| < 0.4$, but because of the non-uniform response to jets as a function of η_{det} in the ICR and the EC, the relative MPF response correction is applied to address this effect and obtain uniform correction independent of η_{det}. In the homogeneous region of CC, this response for jets can be parameterized by a quadratic logarithmic function:

$$R(E') = p_0 + p_1 \log(E'/E_0) + p_2 \log^2(E'/E_0), \tag{3.15}$$

where $E_0 = 100\,\text{GeV}$ and p_i are free parameters to be determined in a fit. The absolute response of the calorimeter as a function of the jet energy is shown in Figure 3.5.

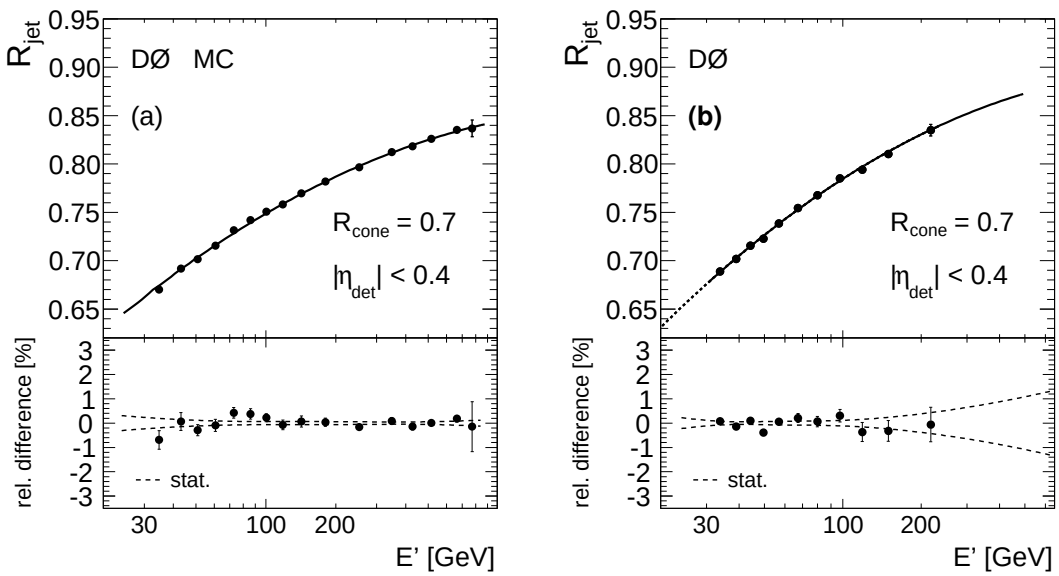

Figure 3.5: The absolute response of the calorimeter as a function of E' for $R_{\text{cone}} = 0.7$ jets in (a) MC and (b) data. The solid line indicates the fit to the function as in Eq. (3.15).

Of all correction factors, only the response is the term that results in energy being missed by the calorimeter, and this effect alone must be used to correct the event $\not{E}_T$.

The bias correction to the response, k_{R}, consists of three sources. First is the correction for the background of the γ+jet sample, consisting mainly of dijet events. Second source is due to the different effects of zero suppression inside and outside

the jet as there is a transverse momentum imbalance because of the offset energy. Third correction estimates the response to the hadronic recoil against the photon, which can differ from the true jet response, especially for forward jets.

The showering correction, S, is the last correction as after offset subtraction, not all the energy contained inside the jet cone originates from particles belonging to the particle jet, and thus the response correction can not recover the original particle jet energy. Showering is defined to compensate for the net energy flow through the jet cone boundary and in a way consistent with the rest of corrections to ensure that the particle jet energy is recovered. The showering correction is determined in both data and MC using same γ+jet events selected using the same criteria as for the absolute response measurement without the restriction on CC probe jet only. In the case of MC, it is possible to directly obtain an unbiased estimator of the true showering correction and this is later applied to data in a form of a template method to obtain final unbiased correction. In the case of data, the correction is determined by measuring energy distributions in annuli of increasing radius ΔR with respect to the jet axis. Templates are made from MC simulation energy profiles corresponding to the particles belonging to the particle jet matching the reconstructed jet and the rest of the particles. These templates are fit to data to find the size of this correction.

Separate corrections and uncertainties are extracted for data and simulation, for each of the jet cone sizes $R_{\text{cone}} = 0.5$ and 0.7, and for the different run periods. Figure 3.6 shows the typical JES correction factor $E_{\text{jet}}^{\text{corr}}/E_{\text{jet}}^{\text{meas}}$ for jets with $R_{\text{cone}} = 0.5$ in two run periods, Run IIa (corresponding to $1.1\,\text{fb}^{-1}$) and Run IIb2 (corresponding to $3.0\,\text{fb}^{-1}$). There are visible "horns" in the profile because of the reduced coverage in ICD region of the calorimeter and also the different response in the forward region of the calorimeter ($|\eta_{\text{det}}| > 3$) is evident. Figure 3.7 offers the comparison of the JES correction factor for $R_{\text{cone}} = 0.7$, where the absolute value is slightly smaller reflecting the better geometric coverage provided by the larger cone radius. The dashed lines represents total uncertainties on the corrections (more details about uncertainties can be found in Ref. [64]).

After calibrating the jet energy, the jet energy resolution is investigated using the γ+jet and the Z+jet events [66]. A process called jet shifting, smearing, and removing (JSSR) is used to compare the simulated jets to the jet resolution measured in the data, and the jet resolution is smeared to reproduce the resolution in the data.

3.7.1 Flavor Dependent Correction

The jet energy scale correction depends, in addition, on the topological configuration of the jet, i.e. type, energy and angular spectra of particles constituting the jet are important factors in JES. Jets originating from different flavors of parent partons have different topologies, and jets produced in different processes have different parent parton flavor compositions. This leads to a flavor-dependent JES. The standard JES correction described in Section 3.7 at DØ takes into account the

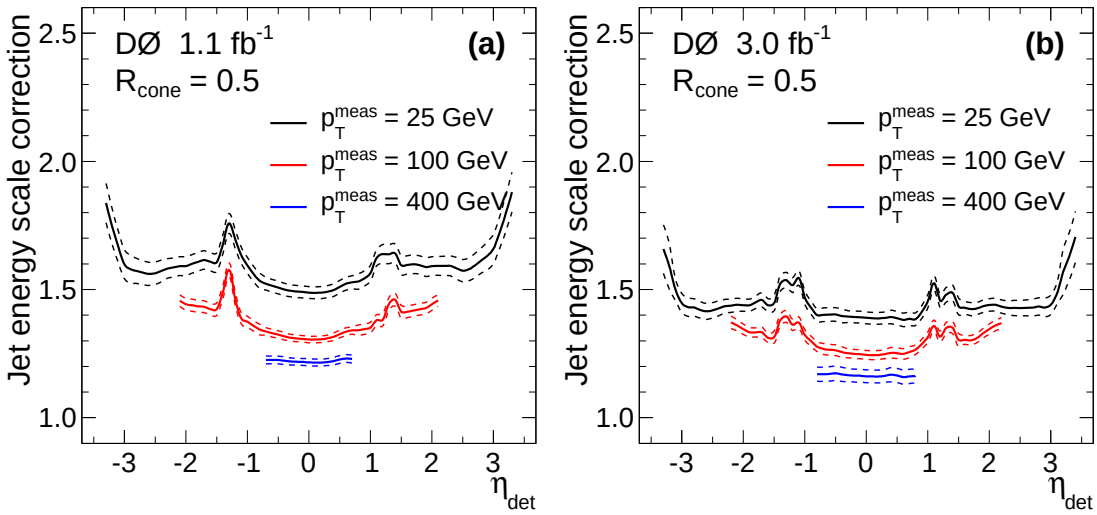

Figure 3.6: Jet energy scale corrections, $E_{\text{jet}}^{\text{corr}}/E_{\text{jet}}^{\text{meas}}$, for data jets with $R_{\text{cone}} = 0.5$ in (a) Run IIa and (b) Run IIb2 as a function of η_{det} for different uncorrected jet p_T^{meas} values. Dashed lines show the total systematic uncertainty on the corrections.

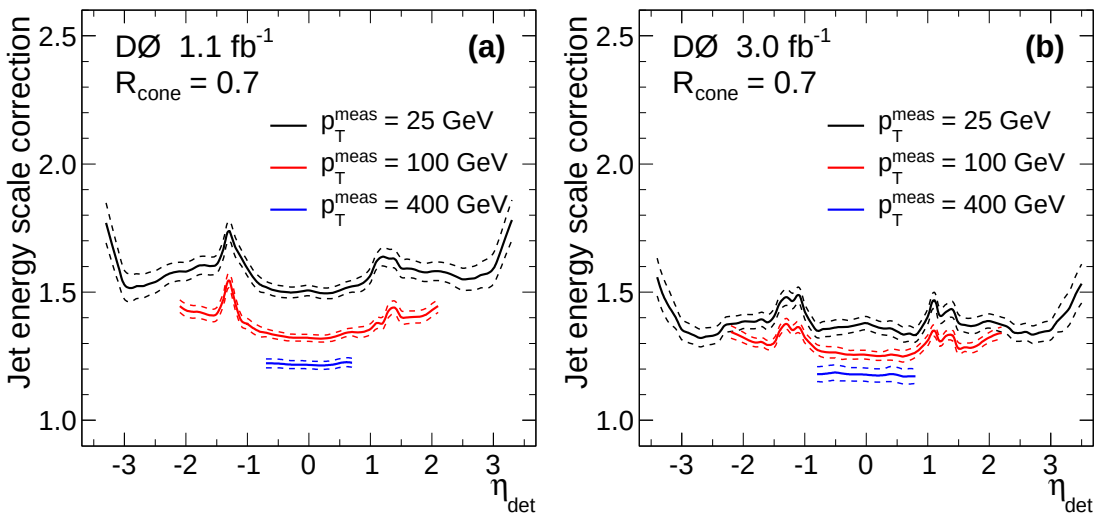

Figure 3.7: Jet energy scale corrections, $E_{\text{jet}}^{\text{corr}}/E_{\text{jet}}^{\text{meas}}$, for data jets with $R_{\text{cone}} = 0.7$ in (a) Run IIa and (b) Run IIb2 as a function of η_{det} for different uncorrected jet p_T^{meas} values. Dashed lines show the total systematic uncertainty on the corrections.

kinematic dependence, but not the flavor dependence. Many analyses calibrate the data analysis results using the MC simulation (including most measurements with the top quark), and therefore it is necessary for the MC to do a good job in describing data. In the view of the flavor dependent jet response, this is true at CDF as they tune their detector simulation using test beam data to have the same

response to single particles (mainly to charged pions) as in data [67]. Unfortunately, this is not the case at DØ which has different single particle responses between the MC simulations and data due to the absence of test beams to tune the calorimeter simulation.

Therefore, the flavor-dependent MC-data difference in the jet response at DØ has been a large factor for the systematic uncertainty evaluation in many measurements, especially in the top quark sector. Most important systematic uncertainty sources consists of

(a) difference in the b and light jet response ratio between the MC and data;

(b) difference in the quark and gluon jet response ratio between the MC and data.

This sources can contribute significantly to the uncertainty, for example the DØ top quark mass measurement using the matrix element method in the lepton+jets channel [68] has the systematic uncertainty from (a) about 0.8 GeV and due to (b) about 0.6 GeV. Estimation of (a) is based on the MC and data charged pion responses extracted in the jet response of the data, resulting in ratio between the b and light jet response in the MC higher by about 1.8% compared to that ratio in data. Uncertainty on (b) is given by different particle multiplicity as shown in Figure 3.8. The value has been estimated by the difference between the top quark mass measured from the MC with JSSR shifting turned on and that with shifting turned off. This is, however, very rough estimate that does not completely correspond to the truth, but it has been the only officially accepted way. In total, (a) and (b) give uncertainty of 1.0 GeV, which is by far the largest systematic uncertainty in this measurement, while the corresponding number at CDF is 0.2 GeV. The influence is similar in other analyses, where MC is used to estimate signal/background ratio. The latest measurement of top quark mass [40] using the flavor dependent correction, that is described in this section, corrects for this sources and the uncertainty on the method counts for only 0.16 GeV.

The method to correct the MC for the MC-data difference in the jet response at DØ is called Flavor Dependent Correction [69]. The idea of the method is that for each calorimeter jet in the MC, a spatially matched particle jet is looked for to calculate the correction factor F

$$F = \frac{\sum_i E_i \cdot R_i^{\mathrm{data}}}{\sum_i E_i \cdot R_i^{\mathrm{MC}}}, \tag{3.16}$$

where the subscript i runs over the particles in the particle jet, E_i are the energies of the particles and R_i the single particle responses in MC or data. However, this factor implies the new Jet Energy Scale. In order to preserve standard JES, the ratio of this correction factor and average F in γ+jet sample is used:

$$F_{\mathrm{corr}} = \frac{\frac{\sum_i E_i \cdot R_i^{\mathrm{data}}}{\sum_i E_i \cdot R_i^{\mathrm{MC}}}}{\langle F \rangle_{\gamma+\mathrm{jet}}}. \tag{3.17}$$

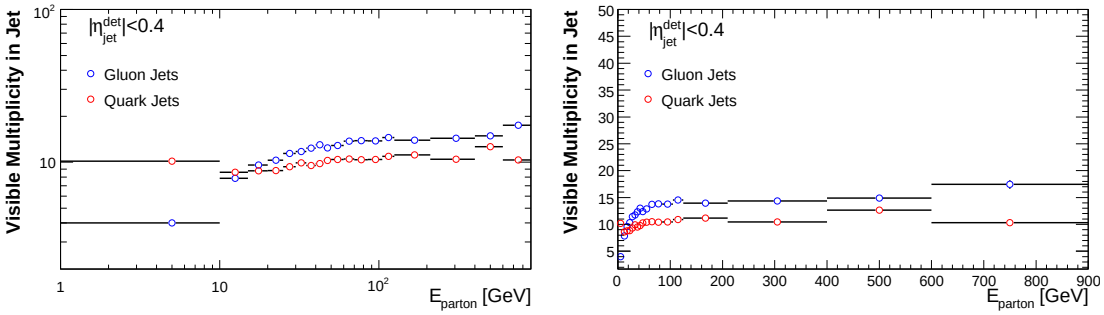

Figure 3.8: Number of particles (excluding neutrinos) in particle jets produced by quarks or gluons in γ+jet MC samples. On the left side in logarithmic scale and on the right side in linear scale. The x axis is the energy of quarks or gluons, while the y axis shows the number of particles (excluding neutrinos) in particle jets. The simulation is for Run IIa period only.

The $\langle F \rangle_{\gamma+\text{jet}}$ is average correction parameterized without any JES correction applied. The factor F_{corr} should be applied to the jet energy after the offset correction as

$$(E_{\text{jet}}^{\text{meas}} - E_{\text{O}}) \cdot F_{\text{corr}}, \tag{3.18}$$

where $E_{\text{jet}}^{\text{meas}}$ is the measured raw jet energy, and E_{O} the offset correction for noise, pile-up and multiple interactions. The F_{corr} is independent of other JES corrections like response or showering.

To perform evaluation of the correction F_{corr}, the single particle responses in MC and data have to be known. Except the neutrinos, all the other "stable" particles are included to reconstruct the particle jet. Most of the energy in the particle jets is coming from $\pi^{\pm}$ and γ. The matching between the particle jet and calorimeter jet is based on the angular separation $\Delta R = \sqrt{\Delta\phi^2 + \Delta\eta^2}$ between the two. Following MC single particle samples were used: γ, $e^{\pm}$, $\mu^{\pm}$, $\pi^{\pm}$, $K^{\pm}$, K_0^S, K_0^L, $p^{\pm}$, n and Λ. For each single particle, the energy of the calorimeter cells contained in the $R = 0.5$ cone around the particle are summed over to give the MC single particle response, defined as the measured energy divided by the MC truth energy. The responses from single particle MC are parameterized as shown in Figure 3.9 in case of $\pi^{\pm}$ sample. The parameterization has been studied and different fit functions have been found to describe the MC with minimal number of parameters:

$$R_{\gamma}^{\text{MC}} = 0.25 \cdot p_{\gamma}^{0} \cdot \left[1 + \text{erf}\left(\frac{E + p_{\gamma}^{1}}{\sqrt{2 \cdot p_{\gamma}^{2}}}\right)\right]\left[1 + \text{erf}\left(\frac{E + p_{\gamma}^{3}}{\sqrt{2 \cdot p_{\gamma}^{4}}}\right)\right] + p_{\gamma}^{5}, \tag{3.19}$$

$$R_{e^{\pm}}^{\text{MC}} = 0.25 \cdot p_{e^{\pm}}^{0} \cdot \left[1 + \text{erf}\left(\frac{E + p_{e^{\pm}}^{1}}{\sqrt{2 \cdot p_{e^{\pm}}^{2}}}\right)\right]\left[1 + \text{erf}\left(\frac{E + p_{e^{\pm}}^{3}}{\sqrt{2 \cdot p_{e^{\pm}}^{4}}}\right)\right], \tag{3.20}$$

$$R_{\mu^{\pm}}^{\text{MC}} = (p_{\mu^{\pm}}^{0} + p_{\mu^{\pm}}^{1} \cdot E) \cdot \text{Landau}(E, p_{\mu^{\pm}}^{2}, p_{\mu^{\pm}}^{3}), \tag{3.21}$$

$$R_{\mathrm{h}}^{\mathrm{MC}} = p_{\mathrm{h}}^{0} \cdot \left[1 - p_{\mathrm{h}}^{1} \cdot (E/0.75)^{p_h^2 - 1}\right], \tag{3.22}$$

where $h = \pi^{\pm}$, $K^{\pm}$, K_0^S, K_0^L, $p^{\pm}$, n or Λ.

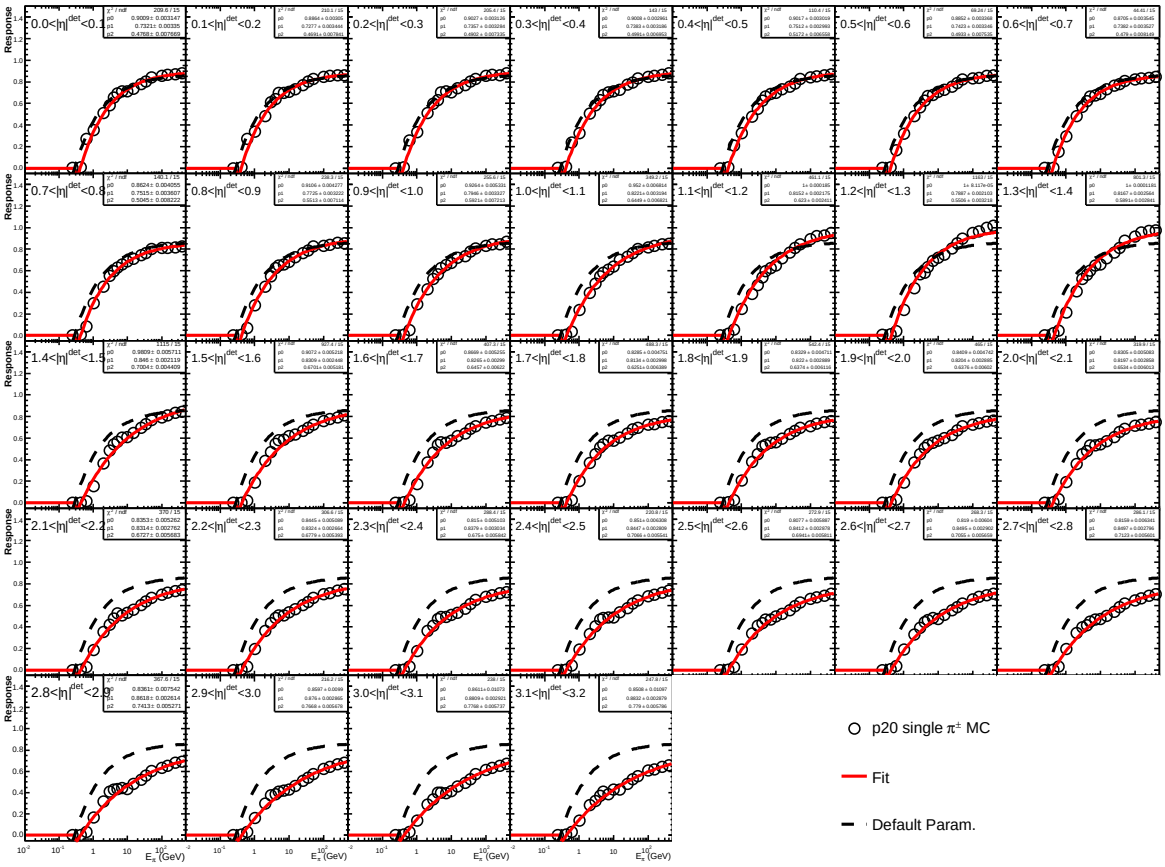

Figure 3.9: Single pion response in DØ detector from Run IIb single $\pi^{\pm}$ MC sample. The black dashed line corresponds to the single pion response evaluated in Run IIa JES studies. The red line is a fit to the MC points represented by black circles.

It is important to check how well the denominator in Eq. (3.17) describes the MC raw jet energy after the offset correction, i.e. the ratio

$$\frac{(E_{jet}^{\mathrm{meas}} - E_{\mathrm{O}}) \cdot k_{\mathrm{O}}}{\sum_i E_i \cdot R_i^{\mathrm{MC}}}, \tag{3.23}$$

as shown in Figure 3.10. The discrepancy in this MC closure test is within 2% and this residual is assigned as a systematic uncertainty.

The single particle responses in data cannot be determined directly. Therefore the MC single-particle responses need to be tuned to reproduce the data in the distribution of the ratio $p_T^{\mathrm{corr}}/p_{T_\gamma}$. Here, p_T^{corr} is the reconstructed jet p_T with the offset correction using the MC single particle responses, and p_{T_γ} is the p_T of the EM cluster that passed the photon selection criteria. The standard JES MC γ+jet

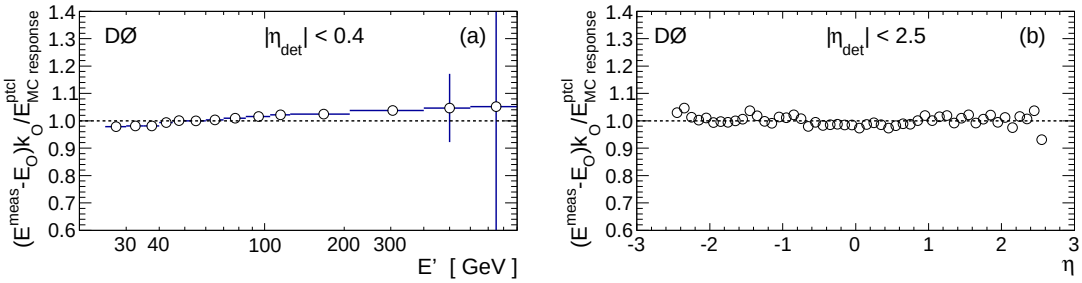

Figure 3.10: Ratio between the jet energy as reconstructed, including offset corrections, and the jet energy calculated using the MC single particle responses, as in Eq. (3.23). (a) shows jets with $|\eta_{\rm det}| < 0.4$ in the γ+jet sample as a function of jet E', and (b) is for jets with $|\eta_{\rm det}| < 2.5$ in the γ+jet sample as a function of jet $\eta_{\rm det}$. The shown uncertainties are statistical.

sample is combined with the dijet sample to provide an accurate representation of the selected data. The responses of γ, $e^{\pm}$ and $\mu^{\pm}$ are considered to be the same in data as in MC. The hadron responses introduce three additional parameters A, B and C as compared to the MC response parameterization as in Eq. (3.22):

$$R_{\rm h}^{\rm data} = C p_{\rm h}^{0} \cdot \left[1 - A p_{\rm h}^{1} \cdot (E/0.75)^{p_h^2 + B - 1}\right] \text{ if } p_T > m_{\rm h};\ 0 \text{ if } p_T < m_{\rm h}, \qquad (3.24)$$

where $R_{\rm h}^{\rm data} = R_{\rm h}^{\rm MC'}$, when A = C = 1 and B = 0. These parameters are varied to reproduce the data distribution of the $p_T^{\rm corr}/p_{T_\gamma}$ ratio in MC and thus the correction factor F defined in Eq. (3.16) depends on A, B, and C through Eq. (3.24).

The tuning of parameters A, B, and C is performed by a fit, which is performed simultaneously for the γ+jet and dijet samples. The procedure is applied for four different $\eta_{\rm det}$ regions of the detector. Figure 3.11 shows the result of the tuning for jets with $|\eta_{\rm det}| < 0.4$. The $p_T^{\rm corr}/p_{T_\gamma}$ ratios are shown before and after MC tuning. Good agreement between MC and data is obtained.

Using the tuned responses in data and the MC single-particle responses in MC, the correction factors F, Eq. (3.16), and $F_{\rm corr}$, Eq. (3.17) are evaluated. The resulting relative jet energy correction factors $F_{\rm corr}$ for different jet flavors (light quark, gluon, and bottom quark) are shown in Figure 3.12. However, the figure is only for illustration purpose since the correction is calculated and applied jet-by-jet. The relative correction required for the light quarks is 1%, but it is significantly larger for gluon and b quark jets, where energies are undercorrected by a few percent, especially at low p_T.

The systematic uncertainty bars shown in Figure 3.12 are given by the sum of three contributions added in quadrature. The dominant contribution is obtained by propagating the fitting errors on the three parameters A, B, and C as estimated by the covariance matrix and is typically smaller than 0.5%. The discrepancy in this MC closure test is propagated as a second contribution to systematic uncertainty. To study this, MC single particle samples with zero-suppression turned on are used

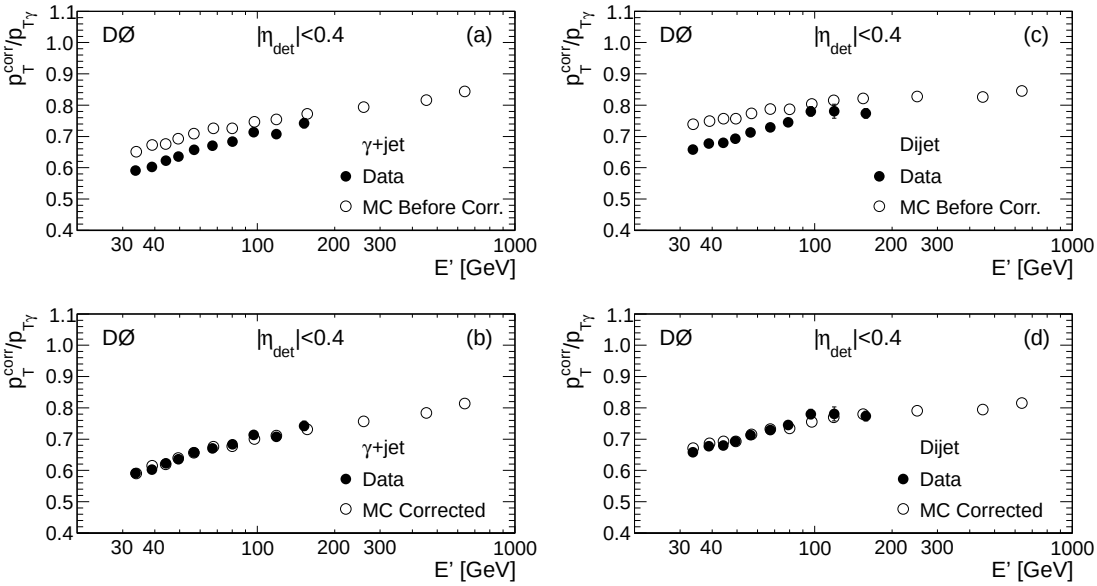

Figure 3.11: Tuning of single particle responses in data and MC using the ratio $p_T^{\mathrm{corr}}/p_{T_\gamma}$ as a function of E' for jets with $|\eta_{\mathrm{det}}| < 0.4$ in a high-purity γ+jet sample, (a) before the MC response correction and (b) after the correction, in dijet events, (c) before the MC response correction and (d) after the correction.

and the difference in evaluated F_{corr} is assigned as uncertainty. It was observed that the samples with ZS turned on are showing good agreement in the MC closure test, although they, unlike the ZS off samples, introduce bias to the calorimeter response. This source of uncertainty is typically small for the CC, but can be up to 0.5% for the ICD and EC. Third source of uncertainty is due to the assumption that the γ, $e^{\pm}$ and $\mu^{\pm}$ responses are perfectly simulated in MC. The γ and $e^{\pm}$ responses are varied according to the accuracy of their energy scale calibration (0.6% and 0.3% respectively), but the effect on final correct is found to be negligible compared to other two sources.

3.8 Author notes

The basics of object identification at DØ are discussed in this chapter. I have not been involved in identification of most of the objects and mostly used only the final product - the data with reconstruction, identification, and various corrections applied. I was part of the MuonID group for a short time testing new trigger files. My main service task in the DØ collaboration was in the Jet Energy Scale group. Together with Zhenyu Ye, I was responsible for the Flavor Dependent Correction, which is described in Section 3.7.1 and also in three DØ Notes [69]. I am the main author of all three, while the last one was my main service task at DØ as I wrote it

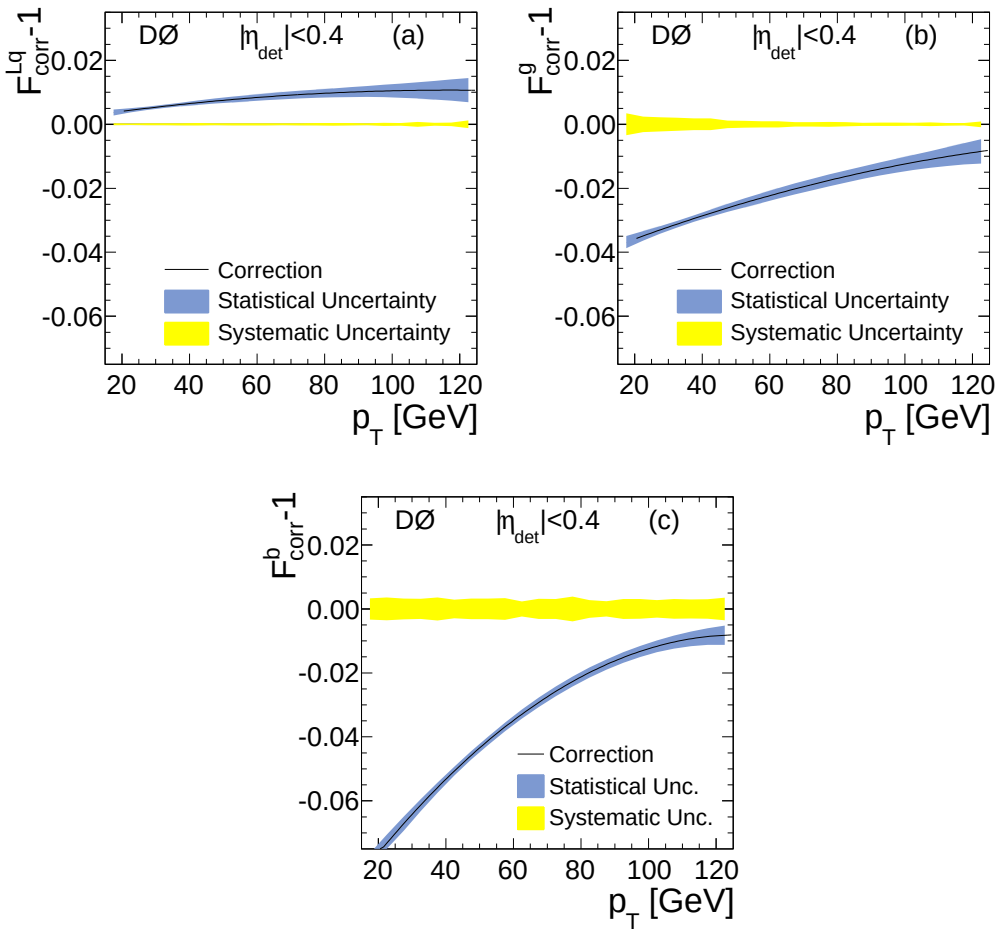

Figure 3.12: The Flavor Dependent Correction factor F_{corr} derived using tuned MC single particle responses for central jets with $|\eta_{\text{det}}| < 0.4$ and different jet flavors, shown separately for jets from (a) light quarks (u, d, s, c), (b) gluons, and (c) b quarks. The bands represent the statistical and systematic uncertainties.

and prepared the output in a code that has been implemented in the DØ framework for the analyzers in different physics groups. In the flavor dependent correction, we achieved very good results that helped to improve JES and the related systematical uncertainties in many measurements, foremost in the top quark mass measurements. This method is also used in the measurement described in this thesis. I was part of the team that finalized the JES studies in the DØ with output being detailed NIM paper [64]. I have been responsible for flavor dependent correction section of this paper and therefore one of the main authors.

Chapter 4
Data, Simulations, and Selection

The measurement of the top quark polarization uses data collected by the DØ detector (corresponding to $9.7\,\mathrm{fb}^{-1}$ of integrated luminosity) and simulated signal and background events. Data has to meet data quality requirements. MC simulations are integrated with a detector simulation for better comparability. This chapter describes the data and the data quality requirements, the MC simulations, and the selection requirements applied to both data and simulations.

4.1 Data

The full Tevatron Run II data sample is analyzed in this measurement. This data were collected with the DØ detector in two major periods: Run IIa (April 2002 – February 2006) and Run IIb (June 2006 – September 2011). The data taking in terms of integrated luminosity is shown in Figure 4.1. The delivered luminosity of $11.9\,\mathrm{fb}^{-1}$ represents the number of collisions by the Tevatron Collider. Unfortunately, not all the time the DØ detector was operational and recording data, which is propagated into the recorded luminosity of $10.7\,\mathrm{fb}^{-1}$. Over 10 billions events were stored by the DØ detector in the Run II period.

To be suitable for analyzing, the recorded data need to pass quality criteria. Such set of criteria is designed to monitor and identify instrumental issues occurred during the subsystem operation. All events are stamped with a Luminosity Block Number (LBN) that is time dependent and splits data into time blocks of only several minutes. For luminosity measurements, the instantaneous luminosity in the block is assumed to be equal to the average luminosity of that period. If one or more subdetectors were not operational at the time of the block, the number is listed as bad in terms of online data quality monitoring[1]. To ensure all information is correct, offline data quality reprocessing is also enabled by recording the status of all detector subsystems into each of the luminosity blocks and stored in the Offline Run Quality Database. All qualified runs must be assured to be free of bad subsystems. The measurement in this thesis uses the standard definition of the

[1]This might apply to a single luminosity block or to longer periods like runs.

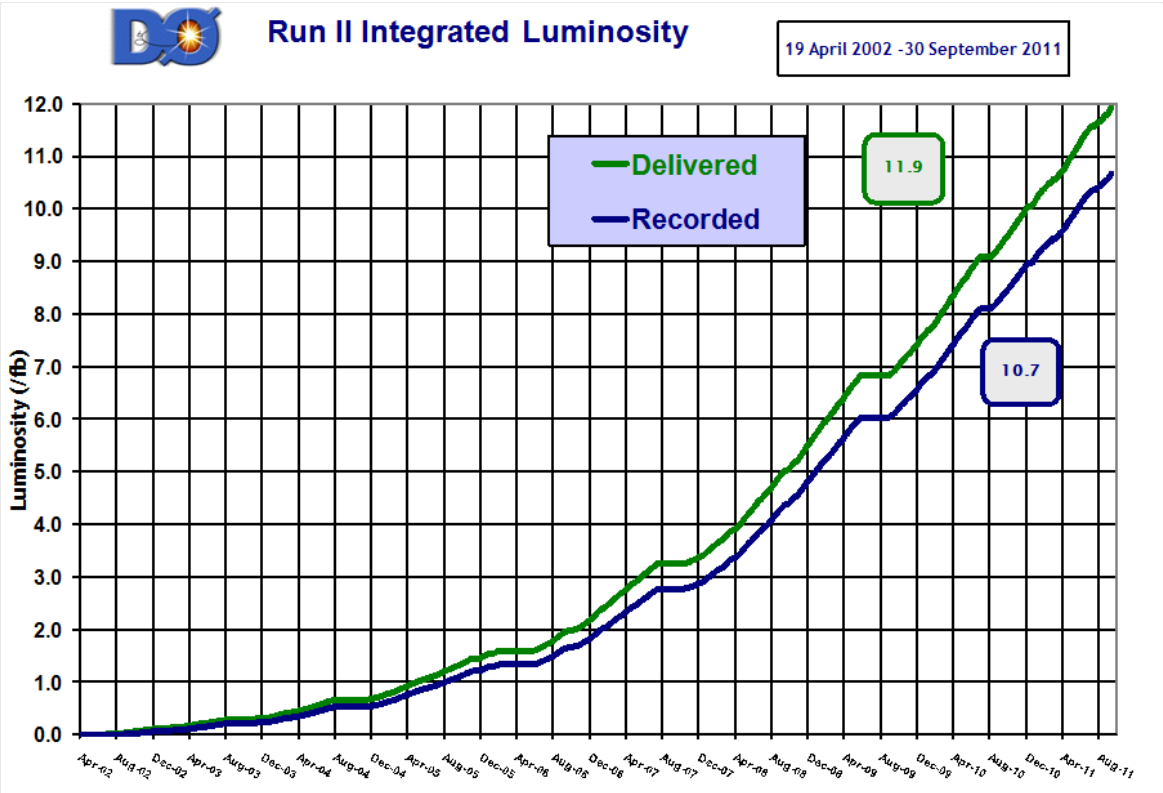

Figure 4.1: The integrated luminosity for Run II of the DØ experiment.

data quality that removes bad runs due to the bad SMT, CFT, muon or calorimeter as well as bad luminosity blocks due to the bad online calorimeter quality and due to the luminosity measurement. After removing bad blocks, the final data sample of integrated luminosity of $9.7\,\mathrm{fb}^{-1}$ is used in the analysis.

As described in Section 2.2.6, different triggers are applied online and offline to the detected events in order to remove large amount of data with no interesting information for physics analysis. This works the same way after the data are recorded - out of the 10 billions of recorded events, only a very small part is interesting for each physics group and selection channels are used in the analyses. To get a pre-selection of data, list of triggers is applied according to the requirements for the selection. First, the un-prescaled trigger is used to calculate the integrated luminosity and trigger versions as listed in Table 4.1. The top OR triggers [70] are used to select events with at least one electron or at least one muon. These triggers are usually sets of L1, L2 and L3 triggers in a form of SuperOR trigger packages. The e+jets channel uses a set of single electron and e+jets triggers. The single electron trigger requires an energy in the EM calorimeter with or without a track and the e+jets triggers require two jets with $E_T > 20\,\mathrm{GeV}$, one jet with $E_T > 25$ GeV and an electron with $E_T > 15$ GeV that matches certain shower shape requirements. The μ+jets channel requires a set of single muon and μ+jets

triggers. The single muon trigger requires hits in the muon system, with or without a loosely isolated track, and μ+jets triggers require at least one jet made with a simple cone algorithm with $E_T > 35\,\text{GeV}$ and a muon with $p_T > 3\,\text{GeV}$. More details about the triggers in different versions is listed in Ref. [70]. Each selected event for this analysis is required to pass one of the two sets, the electron triggers or the muon triggers.

Run Period	Trigger Version	Integrated Luminosity [pb^{-1}]
Run IIa	v8 - v14	1081.21
Run IIb1	v15.00 - v15.83	1217.67
Run IIb2	v15.90 - v16.29	3039.84
Run IIb3	v16.30 - v16.64	1994.27
Run IIb4	v16.65 - v16.99	2403.91
Run IIb	v15.00 - v16.99	8655.69
Run II	v8 - v16.99	9736.90

Table 4.1: Integrated luminosities for data with data quality requirements using un-prescaled triggers for each run period used in this measurement.

At DØ, the reconstruction software is called D0RECO and it employs methods for object reconstruction and identification as described in Chapter 3 and it also employs the trigger information.

4.2 Monte Carlo Simulations

To understand the composition of the data sample, signal and background events are simulated based on theoretical predictions and previously measured quantities and these simulations are compared to data. In the case of the top quark polarization measurement, we are looking for modeling signal to background ratio and for the prediction of the polarization introduced by the background. The simulations are carried out by Monte Carlo (MC) event generators that combine fundamental perturbative theoretical calculations with phenomonological models for a thorough simulation of the physics of an event. The entire chain of the event generation includes the simulation of the hard scattering interaction, the gluon radiation from the initial and final states, the hadronization, the underlying event from minimum-bias interactions, the effects of the detector, and the effects of reading out the detector from the electronic signal.

To simulate the hard scattering, several event generators are used to calculate the matrix elements for the $t\bar{t}$ production and the background production with parturbative QCD: MC@NLO [71], ALPGEN [72], PYTHIA [73], and COMPHEP [74]. While ALPGEN and PYTHIA are LO generators, MC@NLO is a full NLO generator. The simulation of the decay of the unstable particles, i.e. the parton showering

and hadronization processes, is carried out by PYTHIA and HERWIG [75]. Parton showering describes the effect when partons in the hard scattering process radiate gluons, in addition to photon emission, as they carry color charges. Due to the fact that gluons can also emit additional gluons or produce quark-antiquark pairs, partons can easily multiply and form showers of outgoing particles. The radiation from different states of partons observed as the gluons and photons originated from the incoming partons are defined as Initial State Radiation (ISR) and the radiation from the outgoing partons is called Final State Radiation (FSR). Hadronization is imporant beyond O(1) GeV energy scale as hadrons can be formed from parton fragmentation. Since QCD theory becomes non-perturbative at a low energy scale, phenomenological models are required to describe the hadronization at this stage. Two major models used across high energy physics field are string fragmentation (used in PYTHIA) and cluster fragmentation (used in HERWIG). At DØ, the partons interact in hard scatter processes to produce the $t\bar{t}$ pair, not the proton and antiproton. Parton distribution functions (PDFs) are used to properly simulate the colliding momenta of the partons. This analysis uses the CTEQ6.1 PDF [76].

Particles produced by the event generators are required to have simulated the interaction with the detector. The geometry and the material content are simulated with the D0GSTAR program, a simulation of the DØ detector based on GEANT3 [77]. GEANT is a software package that simulates the passage of elementary particles through matter. Physical processes for particle interaction with the detector such as the bremsstrahlung, the pair production, the ionization and the hadronic interactions are included in GEANT. D0SIM simulates the digitization of the simulated data. It adds zero-bias events and pile-up effect as the representation of noise from the detector and electronics.

4.2.1 Signal modeling

For the purpose of the top quark polarization analysis, the primary simulator of the $t\bar{t}$ production is the MC@NLO event generator version 3.4 utilized with HERWIG for the parton showering, hadronization, and modeling of the underlying event. Second generator of the $t\bar{t}$ signal is ALPGEN version 2.11 used with PYTHIA 6.4 for the parton showering and hadronization. The ALPGEN generator is used mainly as a cross-check and for several systematic uncertainty sources evaluation, including the top quark mass dependence as it is generated with the top quark mass of 170, 172.5, and 175 GeV. The MC@NLO event generator includes processes at the orders of α_s^2 and α_s^3. To model the effects of multiple $p\bar{p}$ interactions, the MC events are overlaid with events from random $p\bar{p}$ collisions with the same luminosity distribution as data.

4.2.2 Physics background

Physics background comes from processes with a similar final state as the $t\bar{t}$ events.

W+jets. The main background to the $t\bar{t}$ signal in the lepton+jets channel are the W+jets events, where the W boson is produced via the electroweak interaction together with additional partons from QCD radiation (ISR or FSR) forming jets. The W+jets final state can be split into four subsamples according to the parton flavor: $Wb\bar{b}+$ jets, $Wc\bar{c}+$ jets, $Wc+$ jets, and W+light jets, where light refers to gluons, u, d, or s quarks. The W+jets background is modeled with ALPGEN and PYTHIA.

Diboson. WW, WZ, and ZZ diboson productions are simulated using PYTHIA.

Single top. Events for single top quark electroweak production through the $s-$ and $t-$channel are generated with COMPHEP.

Z+jets. The Z+jets events are simulated with ALPGEN and PYTHIA for events where the Z boson decays to pair of electrons, muons or taus. The Z boson p_T reweighting is applied in order to achieve an agreement of the simulated Z p_T distribution with the data. Additional scale factors are used for the normalization of the Z+jets background.

dilepton $t\bar{t}$. Also the dilepton events from the $t\bar{t}$ decay form a small background to ℓ+jets channel in case one of the leptons is misidentified as a jet or is not detected. Same generators as for the $t\bar{t}$ lepton+jets events are used.

4.2.3 Instrumental background

Instrumental background arises from the mis-identification of a jet with a high electromagnetic fraction, which mimics an isolated electron or a muon from heavy flavor decays. This is the multijet background, numerically the second largest background after the W+jets events.

No MC generator is used to model the multijet background as it has been found that better estimation comes from the data itself using the matrix method [78]. Two different samples are used, one with a loose lepton isolation criteria and one with a tight lepton isolation criteria. Data used for the measurement are contained in the tight sample, which is a subset of the loose sample. Data from the loose sample that do not pass the tight selection criteria are used to estimate the contributions from the multijet background. This sample is known as the loose-minus-tight or QCD sample. The loose and tight samples can be defined as

$$n_l = N^{W-\text{like}} + N^{\text{QCD}} \tag{4.1}$$

$$n_t = \epsilon_{\text{Sig}} \cdot N^{W-\text{like}} + \epsilon_{\text{QCD}} \cdot N^{\text{QCD}}, \tag{4.2}$$

where $N^{W-\text{like}}$ is the number of events with a true isolated lepton that is originating from the physics backgrounds or the $t\bar{t}$ signal, N^{QCD} stands for the number of events with a fake isolated lepton, n_l represents the number of events in the loose sample, and n_t is the number of events in the tight sample. The factors ϵ_{QCD} and ϵ_{Sig} represent the probability for a fake and a real isolated lepton to pass the tight selection criteria, respectively.

The efficiency ϵ_{QCD} is determined from data. By selecting events with $\not\!\!E_T < 10\,\mathrm{GeV}$, but otherwise the same selection criteria as for the signal sample, the data is enriched with QCD multijet events. In this data sample, no real isolated leptons are assumed to be included. The ratio of events with a tight isolated lepton over the number of events in the selected sample with loose isolated leptons yields ϵ_{QCD}. The efficiency ϵ_{Sig} for a true isolated lepton to pass the tight isolation criteria is determined from MC samples with a true isolated lepton in the final state. The cross sections of W+jets and $t\bar{t}$ MC samples are added prior to the determination of the real lepton efficiency.

4.2.4 Beyond Standard Model processes

We use six different BSM models [79] to study modified $t\bar{t}$ production: one Z' boson model and five axigluon models with different axigluon masses and couplings: m200R, m200L, m200A, m2000R, and m2000A, where L, R, and A refer to left-handed, right-handed, and axial couplings, and numbers are the particle masses in GeV. These models are used to validate the measurement in terms of the sensitivity to non-zero polarization as the models are generated with some finite polarization. The events are generated with the MadGraph 5 [80] interfaced to PYTHIA for parton evolution.

4.3 Selection

Even with the right combination of triggers, most of the events in the triggered data sample are entirely unrelated to the $t\bar{t}$ decay to the ℓ+jets channel. Therefore, a set of well tuned criteria is required for events to pass to the final selection that is used in the analysis. The selection process is generally described in Ref. [81]. The goal of this tuning is to have as many top quarks events as possible and the lowest achievable background as the background events contribute to the polarization and their simulation is not perfect. Therefore, the background is a significant source of the uncertainty of the measurement. The selection criteria are applied to both data and MC simulations.

The decay sequence of the ℓ+jets channel is $t\bar{t} \to WbW\bar{b} \to \ell\nu q\bar{q}b\bar{b}$. The result of this chain is one isolated lepton with a large amount of momentum transverse to the beam pipe isolated from other particles, a neutrino represented by the missing transverse energy, and four or more jets. The ℓ+jets channel is divided into two sub-channels characterized by the lepton, e+jets and μ+jets, as both leptons, e and μ are quite different in the view of the DØ detector. The τ leptons are not considered as they decay quickly hadronically, contributing to multijet background, or leptonically, and thus correctly selected in the lepton+jets channel. The criteria common for both sub-channels are:

- Good event quality, as described in Section 4.1.

- The reconstructed primary $p\overline{p}$ interaction vertex (PV) must have a z coordinate of $|z_{\mathrm{PV}}| < 60\,\mathrm{cm}$. This criterion puts the PV within the center of the detector to ensure good tracking.

- Leptons are required to originate from within 1 cm of the PV in the z coordinate, $|\delta z_{\ell,\mathrm{PV}}| < 1\,\mathrm{cm}$.

- Events with second isolated lepton are vetoed to ensure orthogonality to the dilepton channels.

- The curvature of the track associated with the lepton needs to be well measured to reduce the lepton charge misidentification, i.e. we require the track curvature significance $|\mathrm{TrackCurvSig}_\ell| > 1$ and $\mathrm{TrackCurvSig}_\ell > -99$. The TrackCurvSig is defined as $\frac{q/p_T}{\sigma(1/p_T)}$, where q and p_T is charge and the transverse momentum of the of the charged track associated with the lepton.

- The events has at least three jets with $p_T > 20\,\mathrm{GeV}$ and $|\eta_{\mathrm{det}}| < 2.5$, reconstructed with a cone parameter of $R = 0.5$. All jets are required to be vertex confirmed in the Run IIb epoch. While at least four jets are in the signature of the ℓ+jets decay channel, one jets might be lost due to various effects. This will be discussed in Section 5.3.1.

- At least one jet is required to have $p_T > 40\,\mathrm{GeV}$. This leading jet requirement is to suppress the W+jets background.

- At least one jet is tagged as a b quark by the MVA_{bl} algorithm within the L4 operating point ($\mathrm{MVA}_{bl} > 0.035$).

- Fully corrected imbalance in the transverse momentum, $\not\!\!E_T$, is larger than $20\,\mathrm{GeV}$. This is the expected energy carried away by the undetected neutrino.

Additionally to the requirements above, e+jets channel criteria:

- Events have one tight isolated electron with $p_T > 20\,\mathrm{GeV}$ and $|\eta_{\mathrm{det}}| < 1.1$ using MVA working point "emvPoint1".

- Events in data are required to pass the e+jets superOR trigger, which is a combination of the single electron trigger and the e+jets triggers.

- Events pass the triangle cut, $\Delta\phi(\mu, \not\!\!E_T) > 2.1 - 0.035 \cdot \not\!\!E_T$, which helps to reject multijet events.

The additional μ+jets channel requirements are:

- Events have one tight isolated muon with $p_T > 20\,\mathrm{GeV}$ and $|\eta_{\mathrm{det}}| < 2.0$ with Muon ID working point *medium*, track criteria *medium* and isolation *TopScaledTight*.

- Events in data are required to pass the μ+jets superOR trigger, which is a combination of the single muon trigger and the μ+jets triggers. Run IIa data are required to pass only the single muon OR trigger.
- Events pass the triangle cut, $\Delta\phi(e, \not\!\!E_T) > 2.2 - 0.045 \cdot \not\!\!E_T$, which is used to reject multijet events.
- The transverse mass of the reconstructed W boson, defined as

$$M_T^W = \sqrt{(p_T^l + \not\!\!E_T)^2 - (p_x^l + \not\!\!E_x)^2 - (p_y^l + \not\!\!E_y)^2} \tag{4.3}$$

  is $< 250\,\text{GeV}$ and $\not\!\!E_T < 250\,\text{GeV}$.
- Triangular cut inspired by the single top selection is applied as: $((-7 \times \text{cut}) + (2.5465 \times \text{cut}) \times \Delta\phi(\mu, \not\!\!E_T)) > |\text{TrackCurvSig}|$ and $((-0.876 \times \text{cut}) + (0.438 \times \text{cut}) \times \Delta\phi(\mu, \not\!\!E_T)) > |\text{TrackCurvSig}|$, where cut$= 10$. The last two criteria help to minimize mismeasured muons and misreconstructed muon p_T .

4.4 Author notes

In this section, I have described the important facts regarding the data, the data quality, the simulations and the final selection applied to both the data and the MC. Personally, I did not participate in data quality analysis nor in the MC production. There are many details, mainly technical, that I have not described as I believe they are not essential to understand the top quark polarization measurement, despite the fact that they are necessary steps in the process of getting final data in format that can be analyzed.

I believe that the list of signal and background models is very important, as well as the list of the "cuts", the selection requirements, applied on the samples used in the analysis. I took part in the lepton+jets selection in the top quark group at DØ and I am one of authors of the selection Note [81]. However, the selection was a result of work of many people inside the top quark group and also the list of requirements used in this analysis is product of many years of tuning and searching what is the best criteria set to be used for the ℓ+jets channel and it is very similar in the latest top quark measurements in the ℓ+jets final states at DØ, e.g. in Ref. [30]. The only difference are the cuts on the track curvature significance, which are inspired by the forward-backward measurement published in the year 2014 [82]. This requirements was studied to help with lepton (muon especially) p_T precision. I have found this cut also very useful as the top quark polarization measurement relies on the lepton angular distributions and therefore removal of the misreconstructed leptons is essential. I have proven a positive effect of this requirement on the selection and on the polarization result uncertainties in a short study.

Chapter 5

Measurement of Top Quark Polarization

In Chapter 1, the short introduction to the top quark physics and the top quark polarization has been presented together with the motivation for the measurement. This chapter follows with the definition of the top quark polarization, with the list of previous measurement and with the description of the measurement itself in each step that leads toward the final results for the top quark polarization.

This measurement has been described in the DØ Analysis Note [83], DØ Conference Note [19] and most recently published in the Physical Review D (Rapid Communication) [84] that is also included in the Appendix Section B.

5.1 Top Quark Polarization

The SM predicts that top quarks produced at the Tevatron collider are almost unpolarized, while models beyond the Standard Model (BSM) predict enhanced polarizations [85]. The small polarization in SM is generated by SM parity-violating weak interactions [86].

The top quark polarization $P_{\hat{n}}$ can be measured in the top quark rest frame through the angular distribution of the top quark decay products relative to some chosen axis $\hat{n}$ [10]:

$$\frac{1}{\Gamma}\frac{d\Gamma}{d\cos\theta_{i,\hat{n}}} = \frac{1}{2}(1 + P_{\hat{n}}\kappa_i \cos\theta_{i,\hat{n}}), \tag{5.1}$$

where i is the decay product (lepton, quark, or neutrino), κ_i is its spin analyzing power (≈ 1 for charged leptons, 0.97 for d-type quarks, -0.4 for b quarks, and -0.3 for neutrinos and u-type quarks [87]), and $\theta_{i,\hat{n}}$ is the angle between the direction of the decay product i and the quantization axis $\hat{n}$.

The mean polarizations of the top and antitop quarks are expected to be identical because of the CP conservation in strong interactions. Although such polarizations can differ from event to event, the approximation that the top and antitop quark polarization are identical is valid in this measurement as we measure the mean polarization in large sample of events. There has been a cross-check in the evaluation of the top quark polarization and the antitop polarization separately in both data and MC, the results are presented in Chapter 6.

The quantization axes are defined in the $t\bar{t}$ rest frame, while the decay product directions are defined after boosting the particles to the $t\bar{t}$ rest frame and then to the parent top quark rest frame. We measure the polarization along three quantization axes:

- **beam axis** $\hat{n}_p$, given by the direction of the proton beam [10] (for both the top and antitop quark);
- **helicity axis** $\hat{n}_h$, given by the direction of the parent top and antitop quark;
- **transverse axis** $\hat{n}_T$, given as perpendicular to the production plane defined by the proton and parent top (or antitop) quark directions, i.e. $\hat{n}_p \times (-)\hat{n}_{t(\text{or } \bar{t})}$ [9, 88].

Here, the beam and helicity axes have been chosen to represent the longitudinal polarization of the top quark (and will be further in the text referred together as the longitudinal polarizations). Other axes can be used in the definition of the longitudinal polarization, such as the off-diagonal axis, but beam and helicity are preferred. The beam axis was previously used in the DØ top quark polarization measurement and this definition is in favor at the Tevatron energies. On the other hand, the helicity axis have been previously measured by the LHC experiments as it is optimal for the LHC energy. The polarization along the transverse axis, or the transverse polarization, is different from the definition of the longitudinal polarization. It is important that it is allowed to be non-zero in the SM. Therefore, this is a very important quantity and it has never been measured before. In fact, this thesis describes the first measurement of the transverse polarization in the $t\bar{t}$ production.

The polarization defined in Eq. (5.1) can effectively the measured through the cosines of the angles $\theta_{i,\hat{n}}$. It can be simply done by calculating the asymmetry between the positive and negative cosines as

$$A_{P,\hat{n}} = \frac{N(\cos\theta_{i,\hat{n}} > 0) - N(\cos\theta_{i,\hat{n}} < 0)}{N(\cos\theta_{i,\hat{n}} > 0) + N(\cos\theta_{i,\hat{n}} < 0)}, \tag{5.2}$$

where $N(x)$ is the number of events passing the requirement x and the polarization is then $P_{\hat{n}} = 2A_{P,\hat{n}}$. Top quark has a positive charge, while antitop quark charge is negative. The polarization of top quarks and antitop quarks are represented by P^+ and P^-, respectively. Then, the polarization in the CP conservation scenario is $P_{\hat{n}}^{\text{CPC}} = A_{P^+,\hat{n}} + A_{P^-,\hat{n}}$ and CP violating polarization is defined as $P_{\hat{n}}^{\text{CPV}} = A_{P^+,\hat{n}} - A_{P^-,\hat{n}}$. Other way is to use the $\cos\theta_{i,\hat{n}}$ distribution to perform a template fit with simulated samples containing events with positive and negative polarizations. Both methods are used in this measurement, but the template fit provides better performance in incorporating the effects from the expected background and therefore is utilized to measure the polarization in the data.

The lepton is the most sensitive to the polarization, i.e. it has the analyzing power close to unity and is easily identified with a good precision. This measurement

Exp. data	final state	beam axis	Ref.
DØ 9.7 fb^{-1} 1.96 TeV	dilepton	$+0.113 \pm 0.093$ (SM A_{fb}) $+0.072 \pm 0.113$ (meas. A_{fb})	[17]

Table 5.1: Overview of previous results for the top quark polarization along beam axis. The uncertainties are statistical and systematical added in quadrature.

focuses therefore on studying the angular distribution of leptons. The down-type quark has the spin analyzing power of ≈ 0.97 and in theory might be a good candidate to measure the polarization as well as the lepton from the top quark decay. Unfortunately, the identification of the d-type quark is very difficult with the efficiency of only about 50%. It is therefore not used in the measurement. However, to gain statistical precision, we use the reweighted Monte Carlo (MC) down-type quark distributions in forming the signal event templates, as will be discussed later.

The longitudinal polarizations along the beam and helicity axes at the Tevatron collider are predicted by the SM to be -0.0019 ± 0.0005 and -0.0039 ± 0.0004 [86], respectively, while the transverse polarization is estimated to be $\approx +0.0110$ [88]. Observation of a significant departure from the expected value would be an evidence for the BSM contributions [85].

5.2 Previous Measurements

The top quark polarization along the helicity axis was previously studied in $p\bar{p}$ collisions by the DØ collaboration [89] as part of the measurement of angular asymmetries of leptons in 2013. However, this was not a full measurement, rather a short study based on control plots for the $\cos\theta_{\ell,\hat{n}}$ distributions. More recently, DØ measured the top quark polarization along the beam axis, simultaneously with the forward-backward asymmetry, in $t\bar{t}$ final states with two leptons [17], and it was found to be consistent with the SM. This measurement was done in an orthogonal final state to the lepton+jets channel used in this thesis and the DØ combination for the top quark polarization along beam axis has been performed as a part of this analysis. There has been no measurement of the top quark polarization from the CDF experiment. The ATLAS and CMS collaborations measured the top quark polarization in pp collisions along the helicity axis in 2013 and in 2016, and the results are consistent with no polarization production [13, 14]. Both experiments used different approaches, while the method by the ATLAS collaboration is similar to the one in this thesis with the template fit being the main tool in evaluation of the polarization. The previous results for the top quark polarization are summarized in Tables 5.1 (beam axis) and 5.2 (helicity axis). There was no previous measurement along transverse axis or along any other axis apart from the listed beam and helicity axes.

The prediction for the SM polarization along the helicity axis at the LHC is

Exp. data	final state	helicity axis	Ref.
ATLAS $4.7\,\mathrm{fb}^{-1}$ 7 TeV	ℓ+jets and dilepton	-0.034 ± 0.040 (CPC) $+0.020 \pm 0.022$ (CPV)	[13]
CMS $4.7\,\mathrm{fb}^{-1}$ 7 TeV	dilepton	$+0.005 \pm 0.021$	[14]
CMS $19.5\,\mathrm{fb}^{-1}$ 8 TeV	dilepton	-0.022 ± 0.058 (CPC) $+0.000 \pm 0.016$ (CPV)	[14]

Table 5.2: Overview of previous results for the top quark polarization along helicity axis. The uncertainties are statistical and systematical added in quadrature.

slightly different from the Tevatron one, stated in previous Section 5.1, yielding to $+0.002 \pm 0.001$ in CP conserving scenario [14]. All of the measurements are in agreement with the SM prediction, but the motivation for another measurement is substantial as the only result from the Tevatron in dilepton final states is the only result along beam axis and suffers from large uncertainty. Results along helicity axis were measured only in the pp collisions, i.e. in different initial state.

In addition, there has been first measurement of the top quark polarization in the t-channel single top quark production by CMS using $19.7\,\mathrm{fb}^{-1}$ 8 TeV data yielding to polarization of $P_t = 0.52 \pm 0.22$ (with the expected SM value of 0.88) [90]. The single top quark polarization is a very intriguing measurement, but it was not described in this thesis as this measurement was not feasible in the Tevatron data.

5.3 Measurement

The measurement of the top quark polarization in ℓ+jets final states of $t\bar{t}$ production consists of several steps:

- The angular distributions of leptons, e and μ, are analyzed, because they are the most sensitive to the polarization and easily identified in the DØ detector.
- The selection of events in the ℓ+jets final state was described in Section 4.3 - events selected using those requirements are input for the measurement.
- A kinematic fit to reconstruct the lepton angles relative to the various axes is performed, knowledge of the full top quark pair decay is needed.
- The sample composition is studied using kinematic discriminant in order to provide the expectation for the dominant background sources.
- The distributions of lepton angles along various axes are fitted with mixtures of signal templates with $+1$ and -1 polarizations to extract the observed values.
- The measurement is verified with an ensemble testing procedure and with closure test.

- Systematic uncertainties are evaluated by repeating the measurement with modified samples or including uncertainties from assumptions made in the measurement.
- Combination with the previous DØ measurement in the orthogonal dilepton channel is performed.

5.3.1 $t\bar{t}$ Reconstruction

In the DØ detector, only the final states particles from the top quark decay are detected and reconstructed. In order to measure polarization in the top quark pair production, the top quark decay needs to be fully reconstructed to define the four-vectors of the top quark, antitop quark, and the $t\bar{t}$ pair. There are four final state quarks in the lepton+jets decay chain, while the selection, described in Section 4.3, requires at least three jets. If an event contains at least four jets, the four jets with the largest p_T are assumed to be originating from the $t\bar{t}$ decay and the rest is omitted, assuming initial or final state radiation occurred. Event with only three jets are considered to have one of the jets from $t\bar{t}$ decay missing. In either case all possible assignments of three or four jets to the final state quarks are used, with the likelihood of each assignment evaluated by the reconstruction algorithm described in Refs. [91, 92].

For $\ell+ \geq 4$ jet events, the $t\bar{t}$ system is fully reconstructed using a kinematic fitting algorithm, which utilizes an analytic solution for the neutrino momentum using the constraints on the W-boson (M_W) and top-quark masses (m_t). The likelihood term for each jet-to-quark assignment accounts for the differences between the observed jet energy and the energy scaled to satisfy the constraints on M_W and m_t. The jet energy resolution and the probability for a jet to be reconstructed are taken into account. The b-tagging observables MVA_{bl} are also used to evaluate the likelihood of each assignment.

For $\ell + 3$ jet events, a partial reconstruction algorithm of the $t\bar{t}$ decay is employed [92]. One of jets is lost due to the various reasons, e.g. when one of the quarks is too soft or when the angular separation between two of them is small. This algorithm assumes that the jet associated with the b quark from the leptonically decaying top quark is detected. Thus, the reconstruction starts with the M_W term from the leptonic decay of the top quark followed by the leptonic top quark candidate by adding one of the jets. The assumption, that the lost jet is from hadronically decaying top quark, holds for 80% of the $t\bar{t}$ events. The lost jet is assumed to be associated with either a light quark or a b quark from the hadronic top-quark decay. In the majority of cases (74%), this jet is lost due to its low energy, so this loss has little effect on the kinematics of the decaying top quark. Thus, the lost jet is neglected in the partial reconstruction algorithm. The sum of the four-vectors of the two jets assigned to the products of the hadronically decaying top quark serves as a proxy for the four-vector of the hadronically decaying top quark with the invariant mass m_p. Even though m_p is not expected to be equal to

m_t, the distribution in this variable is different for combinations correctly associated with the hadronically decaying top quark and combinations that include a b jet from the leptonically decaying top quark. In each event nine observables are considered: the MVA_{bl} for each of the three jets, the three possible m_t^ℓ (corresponding to the three possible lepton-neutrino-jet combinations), and the three possible m_p. The likelihood of each of the three possible jet-to-quark assignment is calculated by evaluating the consistency of this nine observables with the distributions corresponding to the hypothesized assignment. To compensate for the effect of the lost jet, an m_p-dependent scaling to the four-vector of the hadronically decaying top quark is applied.

In this analysis, all possible assignments of jets to final state quarks are considered and weighted by the χ^2 likelihoods of each kinematic fit. The performance of the three-jet fit is comparable to that for four-jet events, mainly for the reason that the $\ell+\geq 4$ jet events are more likely, up to 45%, to contain jets originating outside the $t\bar{t}$ decay, from initial or final state radiation. This number is only about 4% in $\ell+3$ jet events and thus, even though some information is lost with the unreconstructed jet, no wrong information is added.

The addition of the three-jet sample almost doubles the signal sample as will be shown later. The information from $\ell+3$ jet events is still useful for measuring top properties and the addition of events with the lost jet can actually reduce systematic uncertainties related to jet reconstruction. On the other hand, the background is significantly increased in the $\ell+3$ jet events compared to $\ell+\geq 4$ jet events and it needs to be studied carefully not to bias the top quark polarization.

5.3.2 Sample Composition

Even with carefully tuned requirements for selection, it is not possible to achieve a pure data sample containing only $t\bar{t}$ events unless many real $t\bar{t}$ events are lost during selection and therefore the measurement would lack precision. Thus, the signal and background composition of the data sample needs to be studied and this is essential in case of polarization quantity as, unlike the SM $t\bar{t}$ events, some of the background sources have non-zero polarization by definition. The signal and background models have been described in Section 4.2, most of them being based on MC simulations with use of the theoretical calculations and experimental observations. But it has been observed that this simulations are not describing reality of DØ data precisely and some scaling and corrections need to be applied.

Our data sample in the ℓ+jets final state is composed mainly out of $t\bar{t}$ signal events and W+jets background events. The second largest background is from the multijet events. This background is evaluated from data as described in Section 4.2.3. Sets of ϵ_{QCD} and ϵ_{Sig} parameters are calculated from data for each epoch and for different selections based on lepton type or number of jets. Therefore, we make assumption that it is the best possible estimate of this background. The diboson and single top background events have relatively small contributions in the ℓ+jets

events and the assumption, that the MC generators do good job in description of the contribution of the respective events in data, is taken. The Z+jets generated events are reweighted and normalized according to Ref. [81] to represent DØ data more accurately.

To determine the sample composition, we construct a kinematic discriminant based on the approximate likelihood ratio of expectations for $t\bar{t}$ and W+jets events [93]. The input variables are chosen to:

- have good separation between $t\bar{t}$ and W+jets events;
- be well modeled;
- have no strong correlated with one another or with the lepton angles used in the measurement.

Due to the different reconstruction mechanism, also input variables used for $\ell + 3$ jets and $\ell + \geq 4$ jets channels are different and studied completely separately. The variables considered in the $\ell + 3$ jets channel are: transverse momentum of leading b jet; k_T^{min}; aplanarity; sphericity; H_T^{ℓ}; p_T of third leading jet; m_T from lepton, second leading jet, and $\not{E}_T$; $\Delta R(\text{jet1}, \text{jet2})$; $\Delta R(\ell, \text{jet1})$; lowest M_{jj}; $\Delta\phi(\text{lepton}, \not{E}_T)$; $\Delta\phi(\text{jet1}, \not{E}_T)$; p_T^{ℓ}; and H_T^3. Some other variables have not met requirement of being well modeled, or were correlated to the lepton polar angles, and thus are not listed in here.

The variables considered in the $\ell + \geq 4$ jets channel are: transverse momentum of leading b jet; k_T^{min}; H_T; aplanarity; sphericity; centrality; M_{qq}^{min}; M_{qq}^{max}; χ^2 of best solution in kinematic fit; $M_{b\bar{b}}$; M_{jj}, the invariant mass of jets assigned to W boson; asymmetry defined as $(p_T^{b_{\text{had}}} - p_T^{b_{\text{lep}}})/(p_T^{b_{\text{had}}} + p_T^{b_{\text{lep}}})$; the softest jet p_T; H_T^{ℓ}; p_T^{ℓ}; and M_{bjj}.

The $t\bar{t}$ signal and W+jets background distributions of the input variables were derived from the simulation, and the logarithms of the signal to background ratios, P_S/P_B, for each variable were fitted by polynomial functions as shown in Figures A.1, A.2, A.3 in Appendix Section A. To estimate the best separation power of different combinations of the input variables, a figure-of-merit (FOM) is built from each subset of these variables using formula:

$$\text{FOM} = \int f(x)(2p(x) - 1)^2 dx, \tag{5.3}$$

where x refers to the value of the likelihood discriminant under consideration, $f(x)$ is its distribution, and $p(x) = \frac{P(x|\text{signal})}{P(x|\text{signal})+P(x|W+\text{jets})}$ is the probability for $t\bar{t}$ signal at some given x.

The correlations among input variables and lepton angles are studied directly in the respective distributions by calling ROOT function `GetCorrelationFactor()`. If two correlated variables are selected, only the one with better separation power is kept in the list and the procedure repeated until no correlated variables are selected by the FOM method. The variables are checked for

being well modeled in the control plots before and after sample composition. To quantify the modeling, Kolmogorov-Smirnov (KS) and χ^2 tests are used. Variables that did not passed the criteria were removed and the FOM method repeated.

Since the selections in e+jets and μ+jets channels are different, the channels are analyzed separately in the FOM method. However, the best combination obtained is the same for both channels.

The input variables used for the ℓ+3 jet kinematic discriminant are:

- $k_T^{min} = \min(p_{T,a}, p_{T,b}) \cdot \Delta R_{ab}$, where $\Delta R_{ab} = \sqrt{(\eta_a - \eta_b)^2 + (\phi_a - \phi_b)^2}$ is the angular distance between the two closest jets, a and b, and $\min(p_{T,a}, p_{T,b})$ represents the smaller transverse momentum of the two jets, and the ϕ are their azimuths in radians;
- aplanarity, $A = 3/2\lambda_3$, where λ_3 is the smallest eigenvalue of the normalized momentum tensor $M_{i,j}$;
- H_T^{ℓ}, the scalar sum of the p_T of the jets and lepton;
- $\Delta R(\text{jet1}, \text{jet2})$, the ΔR between the leading jet and the next-to-leading jet;
- $\Delta R(\text{lepton}, \text{jet1})$, the ΔR between the lepton and the leading jet.

The input variables for the $\ell+ \geq 4$ jet discriminant are:

- k_T^{min};
- aplanarity;
- H_T^{l};
- centrality, $C = H_T/H$, where H_T is the scalar sum of all jets p_T values and H is the sum of all jets energies;
- the lowest χ^2 among the different kinematic fit solutions in each event;
- $(p_T^{b_{\text{had}}} - p_T^{b_{\text{lep}}})/(p_T^{b_{\text{had}}} + p_T^{b_{\text{lep}}})$, the relative p_T difference between b_{lep}, the b jet candidate from the $t \to b\ell\nu$ decay, and b_{had}, the b jet candidate from the $t \to bqq'$ decay;
- M_{jj}, the invariant mass of the jets corresponding to the $W \to q\bar{q}'$ decay.

The distributions of listed input variables (often denoted as control plots) are shown in Figures 5.1 (e+3 jets), 5.2 (μ+3 jets), 5.3 ($e+ \geq 4$ jets), and 5.4 ($\mu+ \geq 4$ jets). The discriminant distributions with the combination of chosen variables are shown in Figures 5.5 (e+ jets) and 5.6 (μ+ jets). All the distributions represent the selection with at least 1 b-tagged jet, which is the requirement for selection used in the measurement of the polarization. However, the maximum likelihood fit on the discriminant uses additionally the information from events with no b-tagged jets.

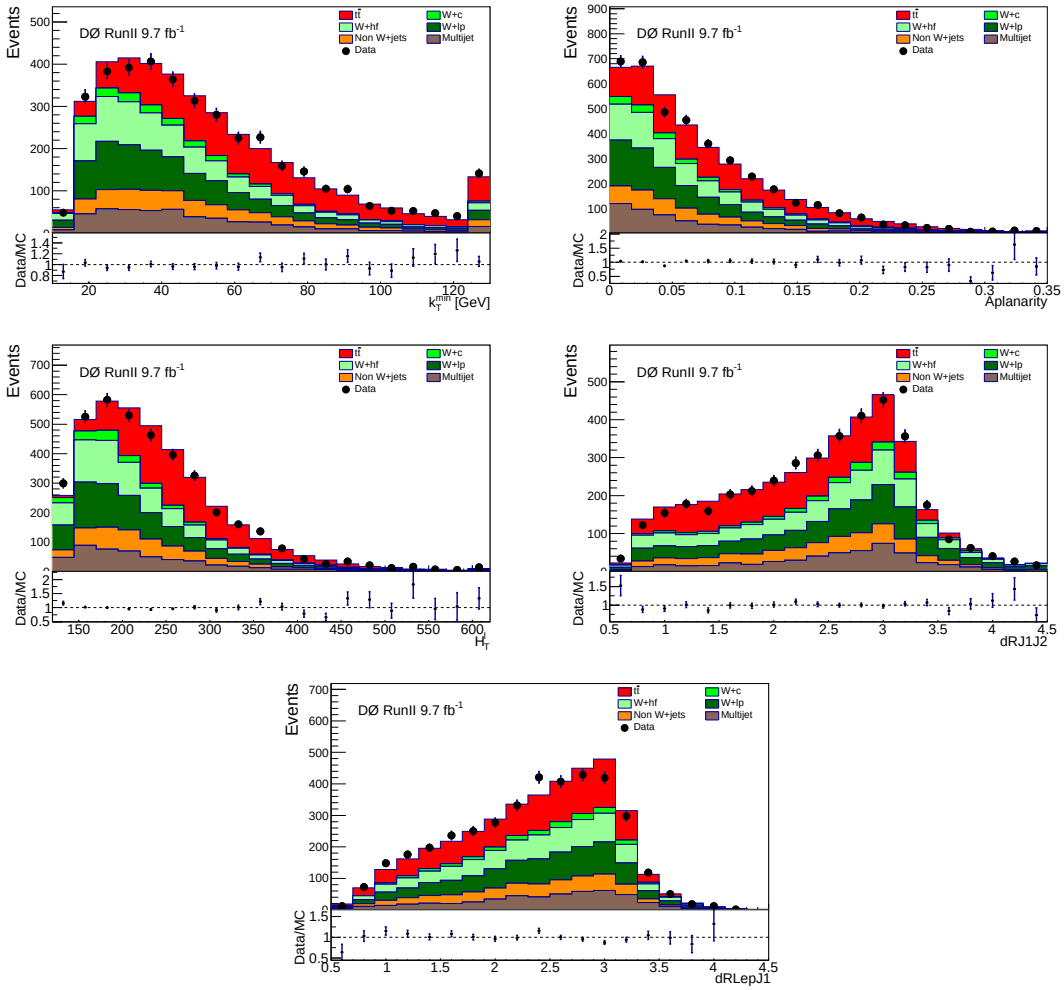

Figure 5.1: Control distributions of input variables for the kinematic discriminant: k_T^{min}, aplanarity, H_T^l, $\Delta R(\text{jet1}, \text{jet2})$, and $\Delta R(\text{lepton}, \text{jet1})$. The selection used is e+3 jets and at least 1 b-tagged jet.

The sample composition is determined from a simultaneous maximum-likelihood fit to the kinematic discriminant distributions on three subchannels in each selection according to the number of b-tagged jets: 0, 1, ≥ 2. The channels without b-tagged jets are not used in the measurement of the top quark polarization, only to determine the sample composition and later the W+jets background calibration. As the first step, the $t\bar{t}$ signal and the W+jets background are normalized in the fit. In the second step, the W+jets background is normalized separately for the heavy-flavor contribution W_{hf} ($Wb\bar{b}+$jets and $Wc\bar{c}+$jets) and for the light-parton contribution W_{lp} ($Wc+$ jets and W+light-parton jets). Other background sources remain constant during the fit. The output of the fit are the scale factors k that modify the sample composition of $t\bar{t}$ and W+jets events, so they better agree with data. The

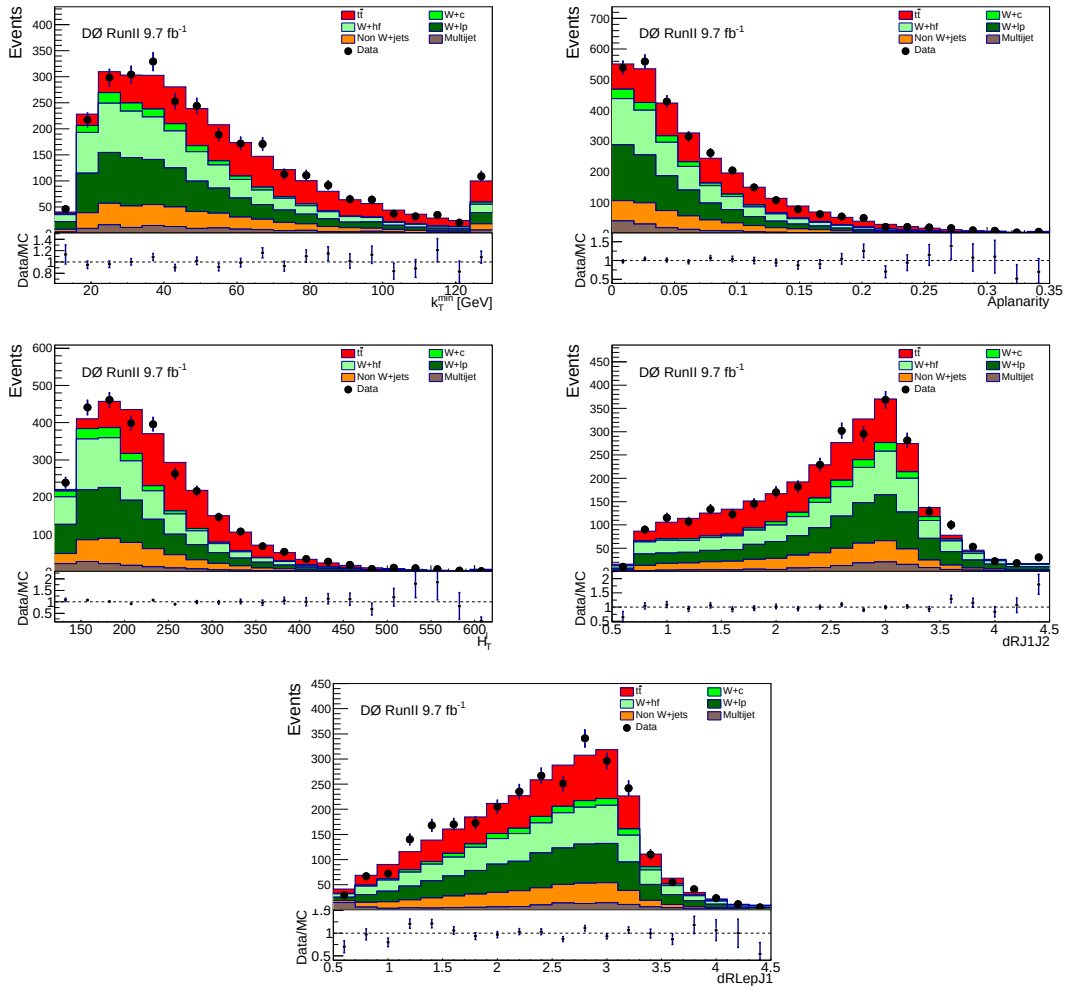

Figure 5.2: Control distributions of input variables for the kinematic discriminant: k_T^{min}, aplanarity, H_T^l, $\Delta R(\text{jet1}, \text{jet2})$, and $\Delta R(\text{lepton}, \text{jet1})$. The selection used is μ+3 jets and at least 1 b-tagged jet.

scale factors are $k_{t\bar{t}}$ for the signal, $k_{W_{\text{lp}}}$ for the light-parton contribution and $k_{W_{\text{hf}}}$ for the heavy-flavor contribution of the W+jets events. The discriminant distributions, as an illustration how the maximum-likelihood fit works, together with the fitted scale factors are shown in Figures A.4 and A.5 in Appendix Section A. The fitted scale factors k are listed in Table 5.3.

The sample composition after implementing the selections, and fitting the maximum-likelihood to data, is broken down into individual channels by lepton flavor and number of jets, and summarized in Table 5.4. The obtained $t\bar{t}$ yield, i.e. the observed $t\bar{t}$ cross-section, is close to the expectations. The term 'Other Bkg' refers to Z+jets, single top, diboson, and $t\bar{t}$ dilepton events.

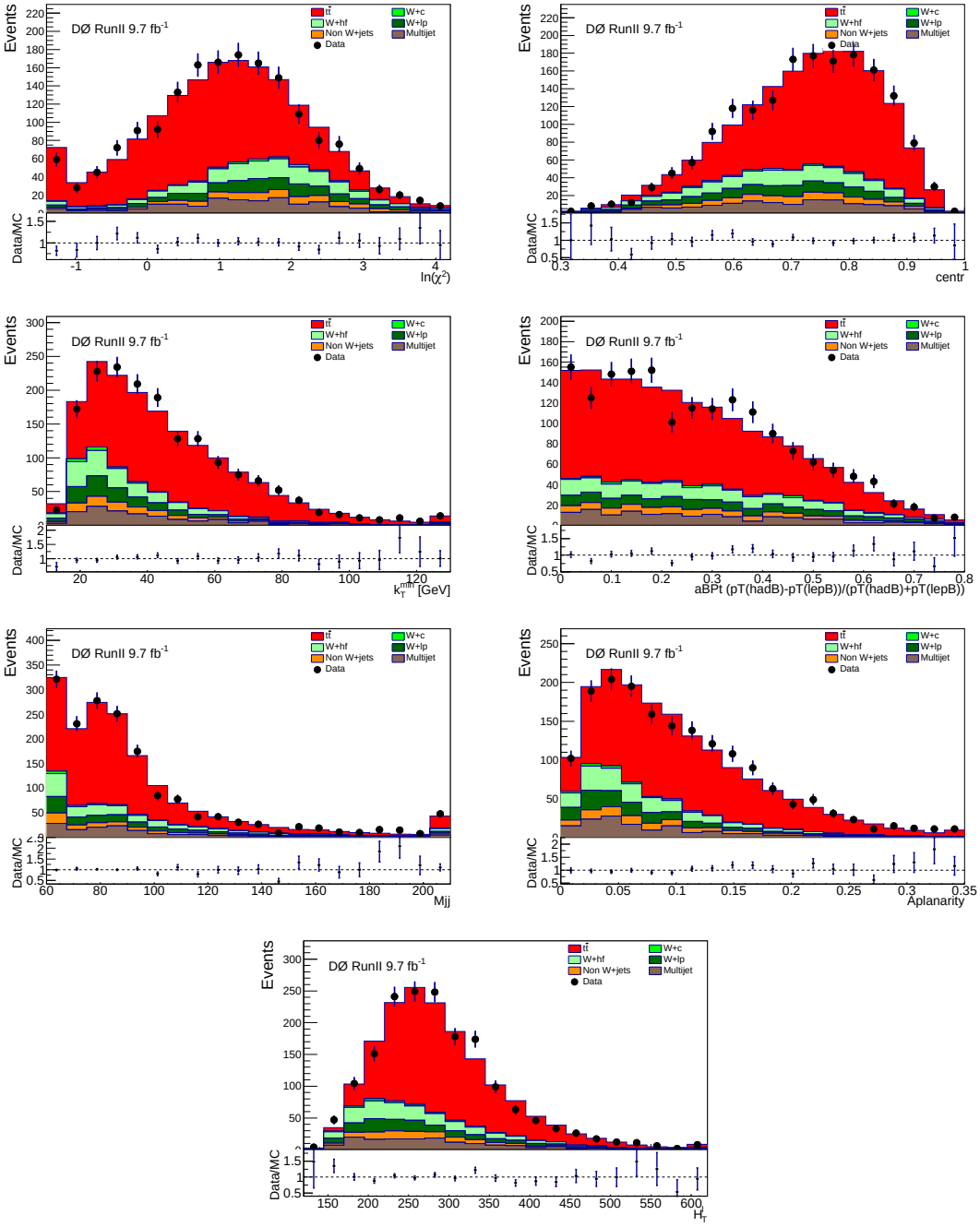

Figure 5.3: Control distributions of input variables for the kinematic discriminant: $\ln\chi^2$, centrality, k_T^{min}, $(p_T^{b_{\rm had}} - p_T^{b_{\rm lep}})/(p_T^{b_{\rm had}} + p_T^{b_{\rm lep}})$, M_{jj}, aplanarity, and H_T^l. The selection used is $e+ \geq 4$ jets and at least 1 b-tagged jet.

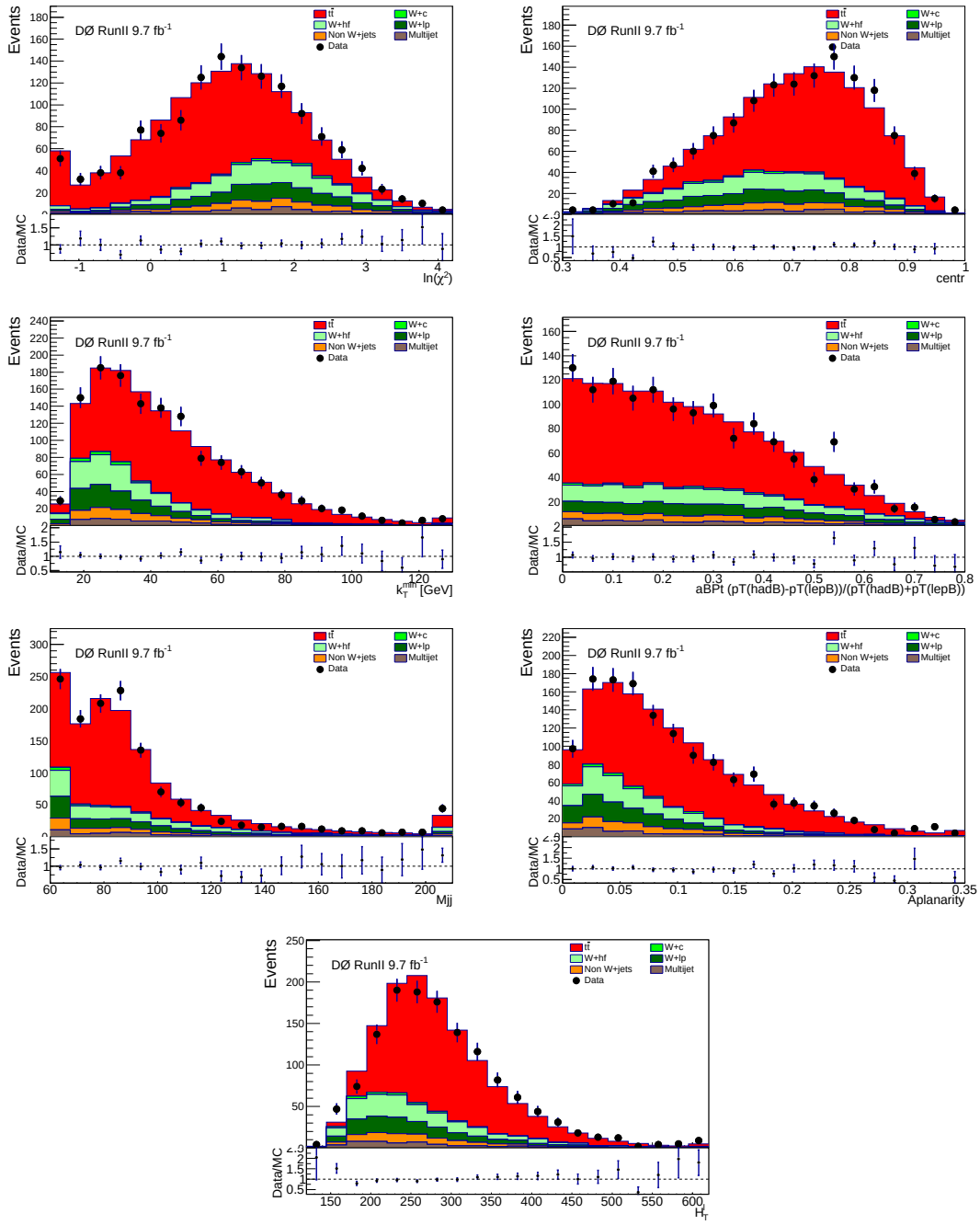

Figure 5.4: Control distributions of input variables for the kinematic discriminant: $\ln\chi^2$, centrality, k_T^{min}, $(p_T^{b_{\rm had}} - p_T^{b_{\rm lep}})/(p_T^{b_{\rm had}} + p_T^{b_{\rm lep}})$, M_{jj}, aplanarity, and H_T^l. The selection used is $\mu+ \geq 4$ jets and at least 1 b-tagged jet.

5.3.3 Correction to W+jets Background

The lepton angular distributions in W+jets events must be well modeled since they form the leading background, with especially significant contribution in the

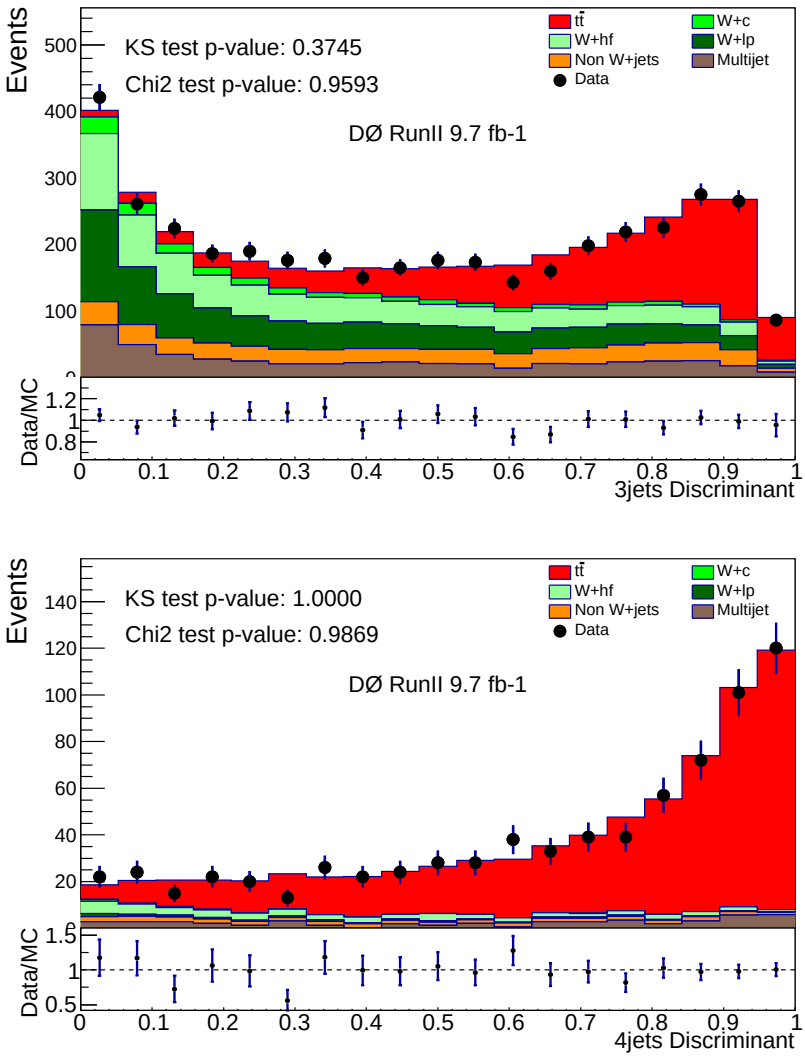

Figure 5.5: The likelihood discriminant distributions for selection e+3 jets (top) and $e+\geq 4$ jets (bottom) with at least 1 b-tagged jet. The p-values for χ^2 and KS tests are shown.

ℓ+3 jet sample. To reduce the dependence of the measurement on the simulated W+jets polarization, we therefore correct the simulated events in a control sample of ℓ+3 jet events with no b-tagged jets, as such events are dominated by W+jets production with more than 70%. This sample is not used for the polarization measurement. In the control sample, the $t\bar{t}$ MC events and background components other than W+jets are subtracted from events in data. The W+jets MC events are reweighted so that the $\cos\theta_{\ell,\hat{n}}$ distributions agree with those from the subtracted data in the control sample. The reweighting takes place in the relative asymmetry in polarization $|\cos\theta_{\ell,\hat{n}}|$ calculated for each pair of positive and negative bins as in

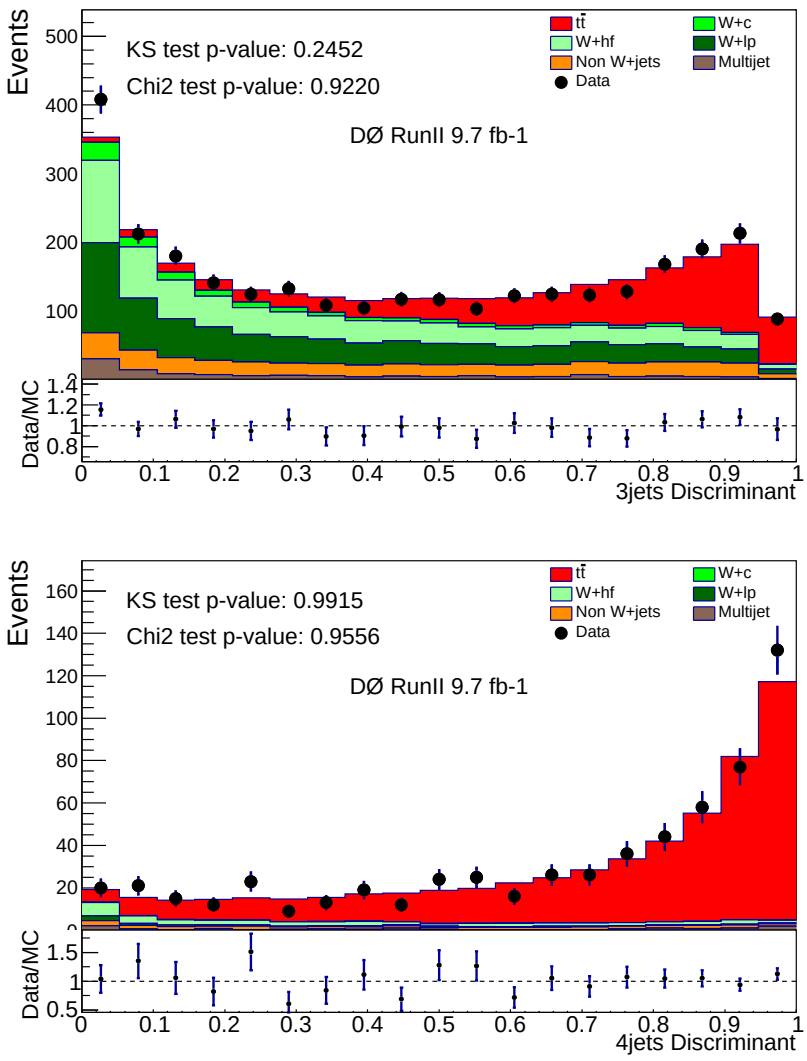

Figure 5.6: The likelihood discriminant distributions for selection μ+3 jets (top) and $\mu+\geq 4$ jets (bottom) with at least 1 b-tagged jet. The p-values for χ^2 and KS tests are shown.

Eq. (5.2). The asymmetries are fitted in order to correct the antisymmetric part of polarization in W+jets events using following weight

$$w = 1 + \alpha \cos\theta_{\ell,\hat{n}} + \beta \cos^3\theta_{\ell,\hat{n}}, \tag{5.4}$$

where α and β are parameters from fit to the relative asymmetry distribution. The process is iterative until the W+jets background shows the same distribution as subtracted data. This is shown for each of the three axes in Figures 5.7 (e + jets) and 5.8 (μ+ jets).

The correction to MC obtained from the control sample is propagated to the the measurement. The correction provided by this procedure is equal to change in

Channel	$k_{t\bar{t}}$(stat.)	$k_{W_{\rm lp}}$(stat.)	$k_{W_{\rm hf}}$(stat.)
e+3 jets	1.112 ± 0.068	0.974 ± 0.030	1.115 ± 0.134
μ+3 jets	1.037 ± 0.076	0.959 ± 0.025	1.169 ± 0.088
$e+ \geq 4$ jets	1.075 ± 0.051	0.882 ± 0.078	1.201 ± 0.085
$\mu+ \geq 4$ jets	1.052 ± 0.056	0.930 ± 0.074	1.198 ± 0.079

Table 5.3: Scale factors k from the sample composition fit for each selection channels studied, the e+3 jets, μ+3 jets, $e+ \geq 4$ jets, $\mu+ \geq 4$ jets. Uncertainties are statistical and propagated to the top quark polarization results as systematical uncertainties.

	3 jets		≥ 4 jets	
Source	e+jets	μ+jets	e+jets	μ+jets
W+lp	825 ± 12	739 ± 11	133 ± 3	120 ± 3
W+c	158 ± 2	131 ± 2	20 ± 1	17 ± 0
W+hf	758 ± 13	697 ± 10	186 ± 2	158 ± 1
Multijet	494 ± 7	128 ± 3	147 ± 4	49 ± 2
Other Bkg	446 ± 5	378 ± 2	87 ± 1	73 ± 1
$t\bar{t}$ signal	1200 ± 25	817 ± 20	1137 ± 24	904 ± 23
Sum	3881 ± 37	2890 ± 25	1710 ± 25	1321 ± 23
$t\bar{t}$ fitted cross-section	7.89 ± 0.11 pb			
$t\bar{t}$ SM expected cross-section	7.37 ± 0.39 pb [29]			
Data	3872	2901	1719	1352

Table 5.4: Sample composition and event yields after implementing the selection requirements and the maximum likelihood fit to kinematic distributions in data. Only statistical uncertainties are shown.

polarization by +0.047 along the beam axis, +0.011 for the transverse axis, and a negligible amount for the helicity axis[1]. This change is mainly due to the significant polarization in the W+jets events that is observed to be +0.18 along beam axis, −0.23 along helicity axis, and −0.02 along transverse axis. Other backgrounds count for polarization of +0.05 (beam axis), −0.30 (helicity axis), and +0.01 (transverse axis), but no specific correction is required as their contributions in the data sample are under 10%, and the large uncertainties on the respective corrections would have larger impact.

[1]That is true in the ℓ+jets channel, separately for e+jets and μ+jets there are significant corrections in the helicity axis, but when both channels are combined, the effects cancel themselves.

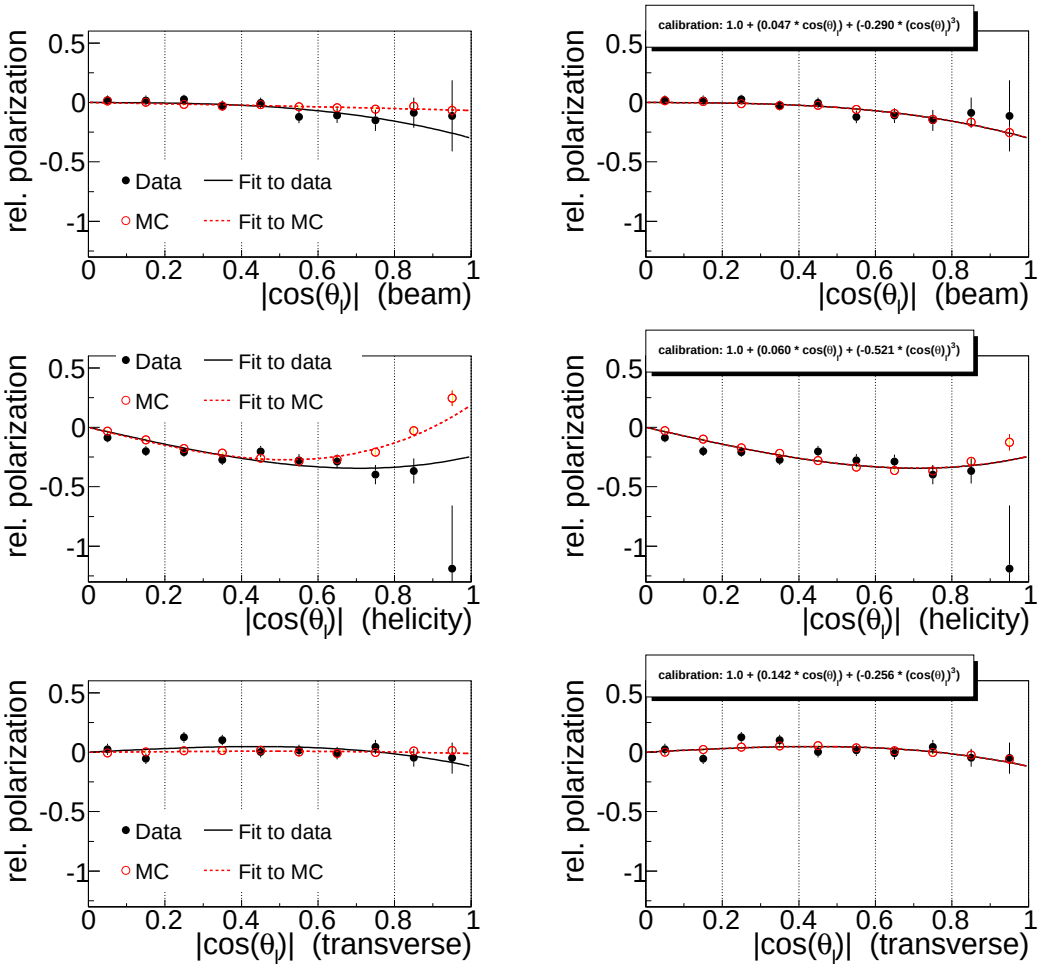

Figure 5.7: Corrections to the W+jets background in the e+jets control sample with 3 jets and 0 b-tagged jets. From the top: beam axis, helicity axis, and transverse axis. Left side shows fit to data subtracted by non-W background events and signal events (black) and fit to uncorrected W+jets simulation sample (red). Rights side shows the correction weight and distributions with the corrected W+jets simulation sample in red color.

5.3.4 Template Fit

To measure the polarization, a fit is performed to the reconstructed $\cos\theta_{\ell,\hat{n}}$ distribution using $t\bar{t}$ templates of $+1$ and -1 polarizations, and background templates normalized to the expected event yield. The signal templates arises from the $t\bar{t}$ MC sample generated with no polarization but reweighted to follow the expected double differential distribution [10]:

$$\frac{1}{\Gamma}\frac{d\Gamma}{d\cos\theta_1\cos\theta_2} = \frac{1}{4}(1 + \kappa_1 P_{\hat{n},1}\cos\theta_1 + \rho\kappa_2 P_{\hat{n},2}\cos\theta_2 - \kappa_1\kappa_2 C\cos\theta_1\cos\theta_2), \quad (5.5)$$

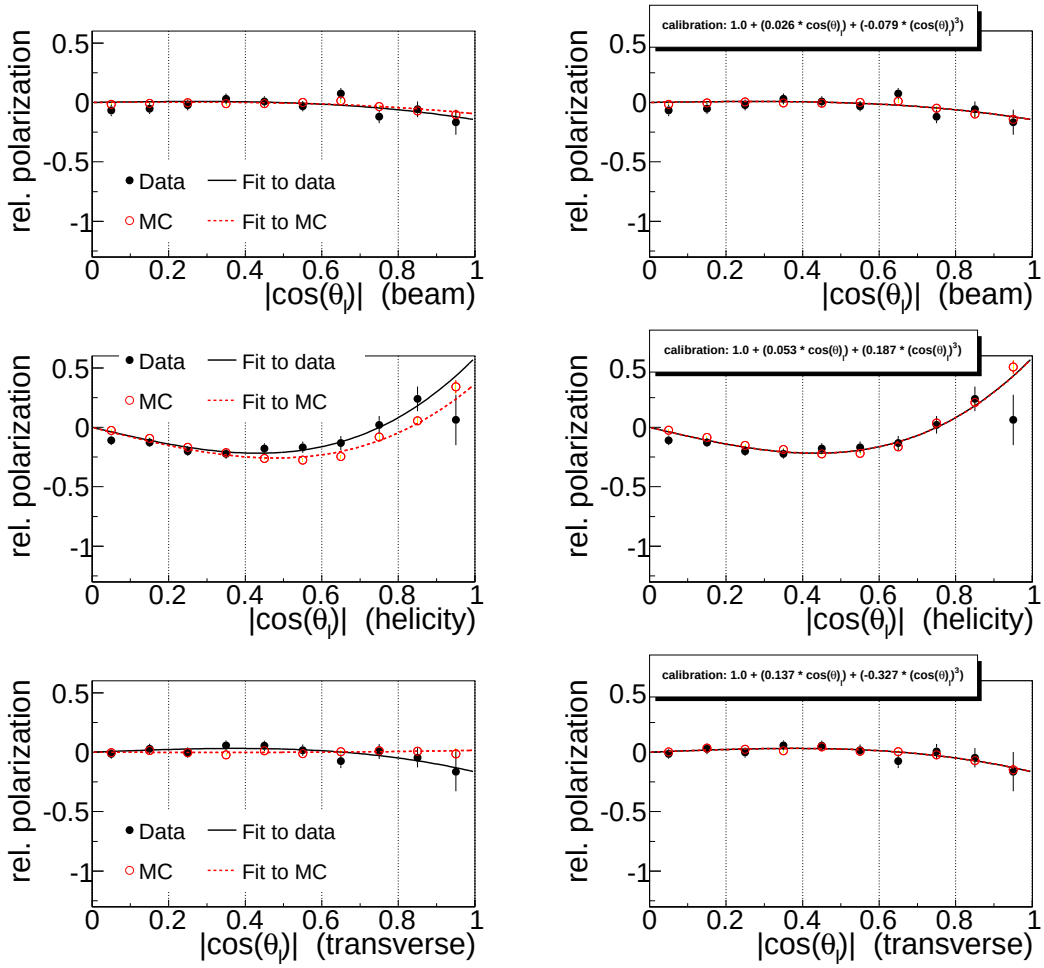

Figure 5.8: Corrections to the W+jets background in the μ+jets control sample with 3 jets and 0 b-tagged jets. From the top: beam axis, helicity axis, and transverse axis. Left side shows fit to data subtracted by non-W background events and signal events (black) and fit to uncorrected W+jets simulation sample (red). Rights side shows the correction weight and distributions with the corrected W+jets simulation sample in red color.

where indices 1 and 2 represent the t and $\bar{t}$ quark decay products (the leptons and down quarks, or their charge conjugates), κ is the spin-analyzing power, as described in Section 5.1 at Eq. (5.1), and C is the $t\bar{t}$ spin correlation coefficient for a given quantization axis. The SM predictions are used, $C = -0.368$ (helicity axis) and $C = 0.791$ (beam axis), both calculated at NLO in QCD and in electroweak couplings in Ref. [10]. The spin correlation factor is not known for the transverse axis, and thus we set $C = 0$. This approximation is tested and it was found that change in C by ± 1 has effect on the transverse polarization of $0.005 - 0.010$, which is assigned as systematic uncertainty. The choices of the C coefficient values have an impact on the BSM searches as various BSM models would change the SM value

of C. This has been investigated and the effect is small, well below the uncertainties of the measurement. The $P_{\hat{n},i}$ represents the polarization state we model (here $P_{\hat{n},i} = \pm 1$) along the chosen axis $\hat{n}$. In the SM, assuming CP invariance, the relative sign factor ρ takes the value $+1$ for the helicity axis and -1 for the beam and transverse axes [10, 94].

A simultaneous fit is performed for the eight samples defined according to lepton flavor (e or μ), lepton charge, and number of jets (3 or ≥ 4). The combinations of different samples, that enter the simultaneous fit, have been studied and this one was found to provide the lowest statistical uncertainty. The observed polarization is taken as $P = f_+ - f_-$, where $f_\pm$ are the fraction of events with $P = +1$ and -1 returned from the fit. The fit is instantiated through `TFractionFitter` class of ROOT. The distributions in the cosines of the polar angles of leptons from $t\bar{t}$ decay for all three axes are shown in Figure 5.9.

A previous measurement of top quark polarization and the forward-backward t and $\bar{t}$ asymmetry in dilepton final states [17] noted a correlation between these two measurements. This correlation is caused by acceptance and resolution effects in the kinematic reconstruction of the events. The same effect has been observed in in ℓ+jets final state. The dependence of the observed polarization on the forward-backward asymmetry, A_{FB}, is determined at the parton level using samples in which the t and $\bar{t}$ rapidity distributions are reweighted to accommodate the polarizations. This relation is

$$w = \frac{1 + A_{\mathrm{FB}} \cdot 2.53 \cdot \left(\tanh \frac{\Delta y}{1.95} + (\frac{\Delta y}{2.16})^3 \right)}{1 + 0.0501 \cdot 2.53 \cdot \left(\tanh \frac{\Delta y}{1.95} + (\frac{\Delta y}{2.16})^3 \right)}, \tag{5.6}$$

where A_{FB} is the NNLO SM calculation of $(9.5 \pm 0.7)\%$ [95], which is in good agreement with the recent result by the DØ experiment in lepton+jets channel of $(10.6 \pm 3.0)\%$ [96], and 0.0501 represents the nominal MC@NLO production-level A_{FB} of $(5.01 \pm 0.03)\%$. The correction is to cover the difference between the two values of the A_{FB}. The function in Eq. (5.6) was obtained in Ref. [17] by a fit in the simultaneous measurement and has been confirmed by observations in this measurement. The resulting correction is -0.030 for the polarization along the beam axis, less than 0.002 for the polarization along the helicity axis, and is negligible for the transverse polarization. The uncertainty on the expected A_{FB} is propagated to the measurement as a systematic uncertainty.

5.3.5 Verification of the Method

The fitting procedure and methodological approach are verified using pseudo-experiments for five values of polarization, and through a check of consistency with predictions, using the BSM models with non-zero generated longitudinal polarizations.

The pseudo-experiments, or ensemble testing, form ensembles consisting of events randomly selected from the signal MC templates of $P = +1$ and -1, according to

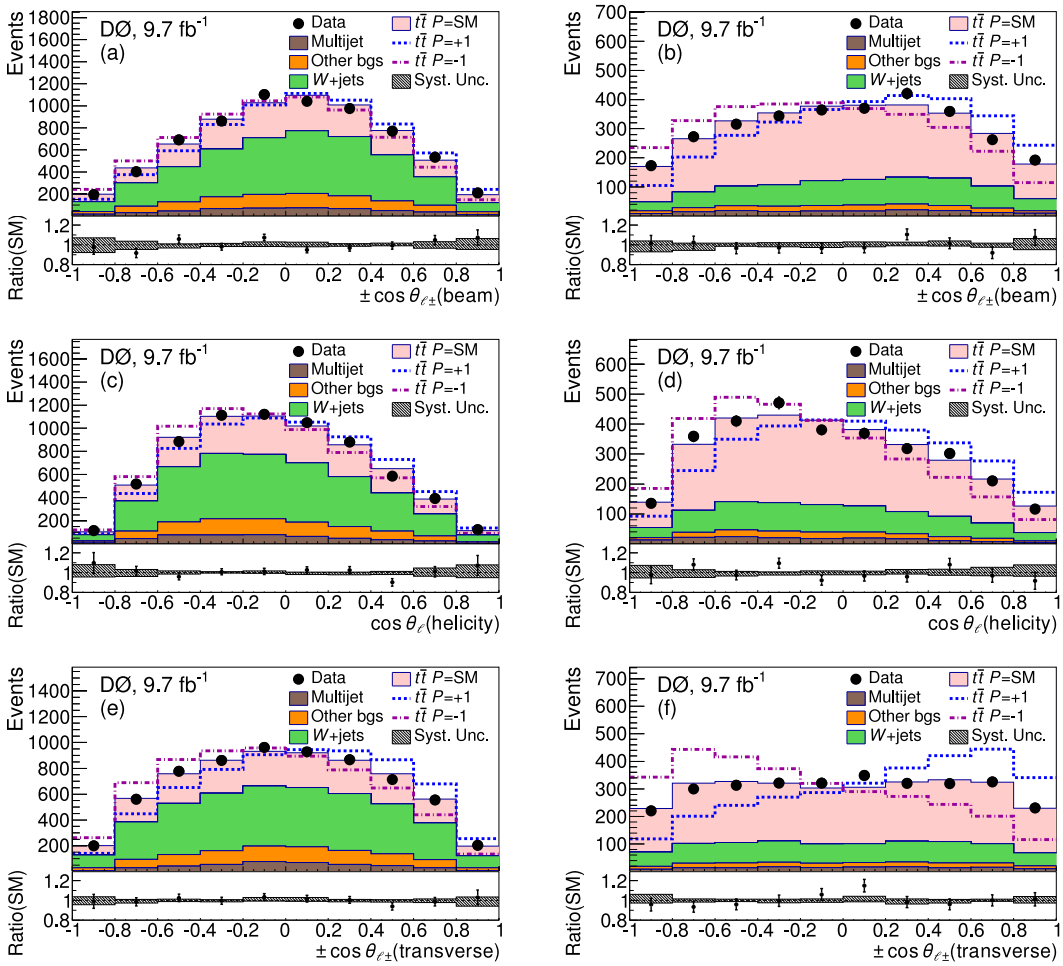

Figure 5.9: The ℓ+jets $\cos\theta$ distributions for data, expected backgrounds, and signal templates for $P = -1$, SM, and $+1$. Panels (a), (c), and (e) show ℓ+3 jet events; (b), (d), and (f) show $\ell+\geq 4$ jet events; (a) and (b) show distributions relative to the beam axis; (c) and (d) show distributions relative to the helicity axis; and (e) and (f) show distributions relative to the transverse axis. The hashed areas represent systematic uncertainties. The direction of the $\cos\theta$ axis is reversed for the ℓ^- events for beam and transverse spin quantization axes plots.

the sample composition. Five different mixing fractions are chosen to represent polarization of $-1, -0.5, 0, +0.5, +1$. For each mixing fraction point 1,000 ensembles are sampled, and the same template fit, as described in previous section, is repeated per ensemble.

The distributions of the results from the template fit are fitted with a Gaussian function, where the mean represents the polarization and the error estimates the expected statistical uncertainty. With results from ale five mixing fractions, the calibration curve is build. The pull, defined as $\frac{f_i - f_g}{\sigma_i}$, where i represents each mixing fraction and f_g is the generated value, is used to test the performance of ensemble

sampling using the pull mean and pull width. A non-biased samples are represented in the pull as Gaussian distributions with mean 0 and width 1. Expected uncertainty needs to be corrected for a non-unity width. The example results of the pseudo-experiments are shown in Figure 5.10 for the case of transverse polarization and $e+$ jets selection. The results for all three axes are summarized in Tables 5.5, 5.6, and 5.7, where the expected statistical uncertainties from ensemble tests, defined as $\frac{\text{meanerror}\times\text{pullwidth}}{\text{slope}}$, are shown. The expected statistical uncertainties show good agreement with the actual statistical uncertainties observed in the template fit with data. Note that pull width different from 1 can indicate over- or under-estimating of the statistical uncertainty and some small differences are observed although by definition of the template method, the results of ensemble testing should be very close to unity in pull width. This has been explained as the fit (`TFractionFitter`) does not work properly in bins with very low statistics, affecting both slope and pull width. This was case in few ensembles, but it was tested that this problem does not take place in the measurement with data as it occurred only in few ensembles with large polarization of $+1$ and -1.

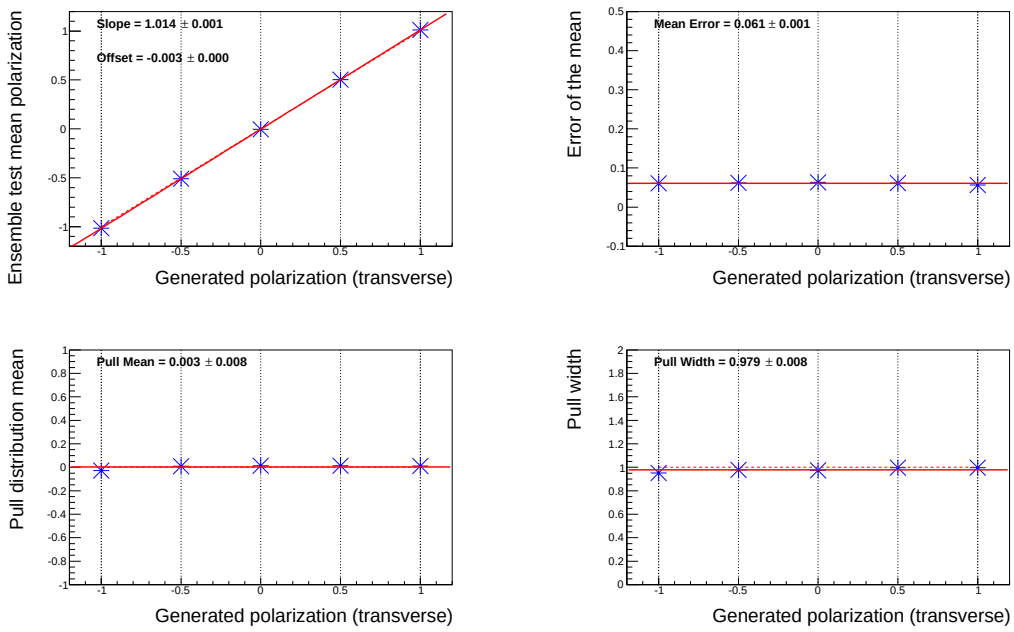

Figure 5.10: The pseudo-experiments with five 1,000 ensembles with different polarization showing distribution of mean (top left), mean error (top right), pull mean (bottom left), and pull width (bottom right). The plots are showing polarization along transverse axis in the e+jets final state.

To verify that the template method is sensitive to the non-zero polarization, we use MC samples that are generated with some finite non-zero top quark polarization, that were descibed in Section 4.2.4 and summarized in Table 5.8. This procedure

Helicity axis		
Ensemble test results	e+jets	μ+jets
Mean slope	1.035 ± 0.001	1.046 ± 0.003
Mean off-set	-0.004 ± 0.000	0.000 ± 0.002
Mean error	0.095 ± 0.001	0.111 ± 0.000
Pull mean	-0.001 ± 0.005	-0.007 ± 0.011
Pull width	0.988 ± 0.006	0.980 ± 0.009
Expected stat. uncertainty	0.094	0.109

Table 5.5: The pseudo-experiment results for polarization along helicity axis with the expected statistical uncertainty.

Beam axis		
Ensemble test results	e+jets	μ+jets
Mean slope	1.056 ± 0.003	1.027 ± 0.002
Mean off-set	-0.005 ± 0.002	0.001 ± 0.001
Mean error	0.117 ± 0.002	0.081 ± 0.001
Pull mean	0.006 ± 0.005	-0.004 ± 0.008
Pull width	0.987 ± 0.005	0.978 ± 0.009
Expected stat. uncertainty	0.115	0.079

Table 5.6: The pseudo-experiment results for polarization along beam axis with the expected statistical uncertainty.

Transverse axis		
Ensemble test results	e+jets	μ+jets
Mean slope	1.014 ± 0.001	1.023 ± 0.003
Mean off-set	-0.003 ± 0.000	0.000 ± 0.002
Mean error	0.061 ± 0.001	0.075 ± 0.001
Pull mean	0.003 ± 0.004	0.016 ± 0.014
Pull width	0.982 ± 0.005	0.977 ± 0.007
Expected stat. uncertainty	0.060	0.073

Table 5.7: The pseudo-experiment results for polarization along transverse axis with the expected statistical uncertainty.

is called the closure test. First, the generated polarization at the parton level (before any selection) is studied. This generated polarization is compared to the measured polarization, which is obtained by the template fit the same way as the measurement with data. Here, the data are substituted by the BSM signal MC of the respective model. The closure test is shown in Figure 5.11 for the polarization

along beam axis and in Figure 5.12 for the polarization along helicity axis. The values are summarized in Table 5.9 for the beam axis and in Table 5.10 for the helicity axis. Note that the uncertainties are only statistical obtained from limited statistics of the samples and as uncertainties from the template fit.

Model [79]	mass (GeV)	width (GeV)	$g_L(u)$	$g_R(u)$	$g_L(t)$	$g_R(t)$
Axi m200R	200	50	0	$0.5g_s$		
Axi m200A	200	50	$-0.4g_s$	$0.4g_s$		
Axi m200L	200	50	$0.5g_s$	0		
Axi m2000R	2000	960	0	$-0.8g_s$	0	$6g_s$
Axi m2000A	2000	1000	$0.6g_s$	$-0.6g_s$	$-4g_s$	$4g_s$
Z'	220	2.9	$0.7g_{Z'}$	$0.7g_{Z'}$		

Table 5.8: Overview of the parameters used in generation of the BSM models used to verify template fit. g_s is the strong coupling constant.

Model [79]	Beam generated	Beam measured
Axi m200R	0.135 ± 0.001	0.141 ± 0.009
Axi m200A	-0.002 ± 0.001	-0.007 ± 0.011
Axi m200L	-0.137 ± 0.001	-0.144 ± 0.009
Axi m2000R	0.081 ± 0.001	0.073 ± 0.010
Axi m2000A	-0.001 ± 0.001	-0.006 ± 0.011
Z'	-0.186 ± 0.001	-0.172 ± 0.013
MC@NLO	-0.004 ± 0.007	-0.005 ± 0.004
ALPGEN + PYTHIA	0.000 ± 0.006	-0.005 ± 0.003

Table 5.9: Comparison of generated and measured values of the polarization along beam axis. The uncertainties are only statistical.

The transverse polarization is not shown as it has not been generated in any of BSM models and therefore all the values are close to zero. We see a very good agreement in the beam axis and a small discrepancy in the helicity caused by one heavy right-handed axigluon model (Axi2000R). This is partly due to the physics at high $m_{t\bar{t}}$ that is not modeled very well by the MC@NLO. The high $m_{t\bar{t}}$ physics is modified by the heavy axigluon models. This is studied and added as systematic uncertainty to the polarization measurement. By considering various sources of systematic uncertainties in the closure test, this discrepancy is within uncertainties. Therefore, we observe the fitted polarizations and the model inputs in a good agreement, and the template methodology has been verified.

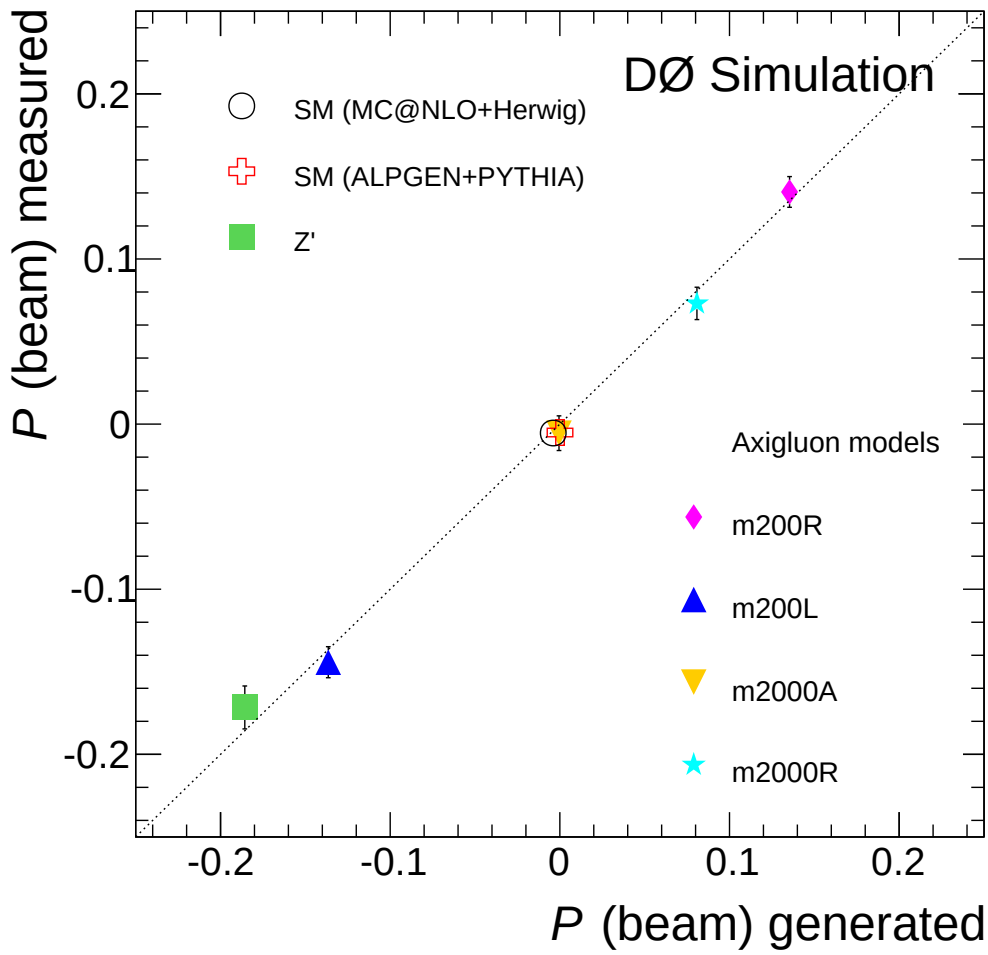

Figure 5.11: Closure test for the template method to measure polarization along the beam axis. The generated polarizations (at parton level) from different BSM and SM models are compared to their measured equivalent that is obtained the same way as polarization in data. The uncertainties are only statistical.

5.4 Systematic Uncertainties

Several categories of systematic uncertainties were evaluated using fully simulated events and assigned into following groups: uncertainties associated with jet reconstruction, jet energy measurement, b-tagging, modeling of background and signal events, parton distribution functions (PDFs), and uncertainties associated with procedures and assumptions made in the analysis.

The sources of systematic uncertainties belonging to the Jet reconstruction group are:

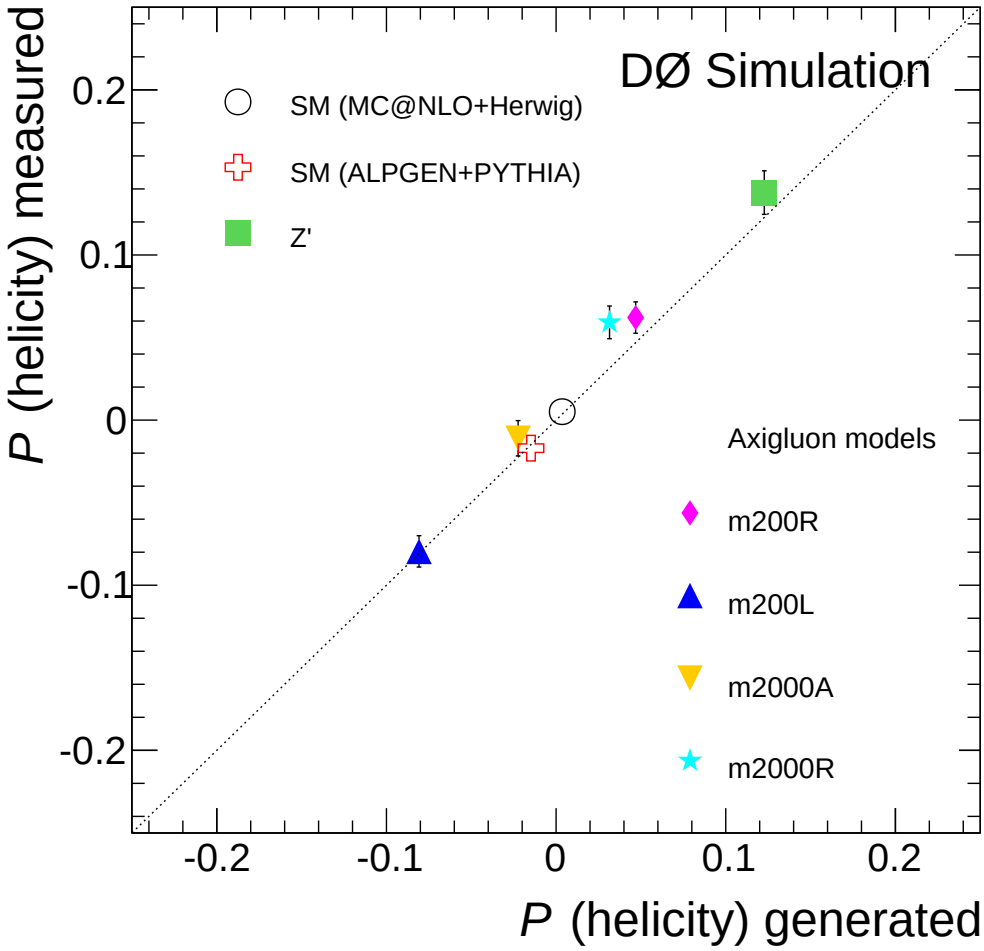

Figure 5.12: Closure test for the template method to measure polarization along the helicity axis. The generated polarizations (at parton level) from different BSM and SM models are compared to their measured equivalent that is obtained the same way as polarization in data. The uncertainties are only statistical.

- **Flavor-dependent jets response** - the flavor dependent jet corrections were described in Section 3.7.1. The uncertainty is evaluated by changing the correction value within its estimated uncertainty.
- **Jet identification efficiency** - uncertainty on the jet reconstruction and identification efficiency is determined by turning off the 'JetID' data/MC scale factor and symmetrized with respect to the nominal sample.
- **Vertex confirmation** - uncertainty on the efficiency of vertex confirmation in jet reconstruction is evaluated by changing the scale factor within its uncertainty. This uncertainty is only for Run IIb data as no vertex confirmation is required

Model [79]	Helicity generated	Helicity measured
Axi m200R	0.047 ± 0.001	0.062 ± 0.010
Axi m200A	-0.018 ± 0.001	-0.010 ± 0.011
Axi m200L	-0.081 ± 0.001	-0.080 ± 0.010
Axi m2000R	0.029 ± 0.001	0.059 ± 0.010
Axi m2000A	-0.022 ± 0.001	-0.011 ± 0.011
Z'	0.123 ± 0.001	0.138 ± 0.013
MC@NLO	0.004 ± 0.007	0.005 ± 0.004
ALPGEN + PYTHIA	-0.015 ± 0.006	-0.017 ± 0.003

Table 5.10: Comparison of generated and measured values of the polarization along helicity axis. The uncertainties are only statistical.

in Run IIa epoch.

Jet energy measurement is represented by:

- **Residual jet energy scale** - uncertainty associated with the overall JES is determined by varying the correction by one standard deviation of total uncertainties in data and MC added in quadrature.

- **Jet energy resolution** - uncertainty on the jet energy resolution is determined by changing the JER correction up and down by one standard deviation.

b-tagging uncertainties are:

- **b-tagging** - b-,c- and light quark jets scale factor uncertainties are varied by one standard deviation up and down according to values provided by BID group.

- **taggability** - taggability efficiency correction is varied by one standard deviation.

The Background modeling consists of:

- **Instantaneous luminosity** - the reweighting of the MC events to match the distribution of instantaneous luminosity in data is turned off and the difference to measurement with the reweighting turned on is assigned as uncertainty on instantaneous luminosity.

- **Trigger efficiency** - trigger efficiency is varied by one standard deviation up and down. The effect of this uncertainty is based on observations from Ref. [97], namely an overall trigger efficiency uncertainty of 5% for low p_T^{top} ($< 90\,\text{GeV}$) events and uncertainty of 2.5% for higher p_T^{top} ($> 90\,\text{GeV}$) events.

- **Lepton identification** - uncertainty on the lepton reconstruction and identification efficiency is determined by changing the LeptonID data/MC scale factors within their derived uncertainties by the ID groups.

- **Background normalization** - the overall normalization uncertainty on the backgrounds is calculated by taking into account the statistical uncertainties of individual backgrounds. For heavy flavor W+jets background, 12% of uncertainty is considered to the production rate [81]. This source is evaluated by taking the quadratic sum of individual variations from the central value.

- **Multijet background** - uncertainties on the lepton identification efficiency and fake rates that are used to estimate the multijet background using the Matrix Method are propagated to multijet background yields as described in Section 4.2.3. Also the shape with respect to the polarization is studied and assigned as systematic uncertainty.

- **Lepton momentum scale** - momentum scale of leptons is known with finite precision. To evaluate the impact of this effect the momentum scale is varied within one standard deviation.

- **W+jets correction** - the calibration to the W+jets background as described in Sec. 5.3.3 is source to systematic uncertainty, the scale factors are varied by their statistical uncertainties and added in quadrature.

- **MC template statistics** - the limited MC signal samples statistic is propagated to the measurements.

The Signal modeling sources are:

- **b-jet fragmentation** - evaluated using uncertainty on the reweighting of the b-fragmentation function from the default value to the value tuned to reproduce collider data.

- **Top quark mass** - the signal used in the measurement is simulated at top quark mass of 172.5 GeV. ALPGEN + PYTHIA samples generated with the top quark masses of 170 and 175 GeV are used to evaluate uncertainty on top quark mass dependence. The resulting difference is scaled to world top quark mass uncertainty of 0.76 GeV.

- **Alternative signal model** - two signal models, ALPGEN + PYTHIA and MC@NLO + HERWIG, are used in separate studies and the difference in polarization is estimated to represent the uncertainty on alternative signal modeling. This uncertainty stands for **Higher order QCD correction**, effect of QCD correction in signal modeling at different orders (LO/NLO), and for **Parton shower and hadronization modeling**, uncertainty on the choice of the parton shower and fragmentation model.

- **Initial/final state radiation** - different amounts of initial and final sate radiation in the simulated $t\bar{t}$ sample are evaluated using ALPGEN + PYTHIA samples with varied amounts of initial and final state radiation.

- **Color reconnection** - impact of the color reconnection of partons that evolve to hadrons is addressed by comparing two signal samples simulated by the ALPGEN + PYTHIA with the PERUGIA 2011 and PERUGIA 2011 noCR tunes.

- $m_{t\bar{t}}$ **modeling** - as found in Section 5.3.5, high $m_{t\bar{t}}$ events play an important role in the polarization measurement and therefore the nominal and template signal distribution of $m_{t\bar{t}}$, simulated by MC@NLO, is reweighted to the NNLO prediction from Ref. [98] and the polarizations recalculated. The difference to result with original sample is then taken as systematic uncertainty for $m_{t\bar{t}}$ modeling.

- $t\bar{t}$ **transverse momentum** - since the transverse momentum of the $t\bar{t}$ pair is not very well modeled as shown in Figure 5.13 (left side), a systematic uncertainty has been estimated by reweighting the MC $p_T^{t\bar{t}}$ distribution to the one observed in data (right side in Figure 5.13).

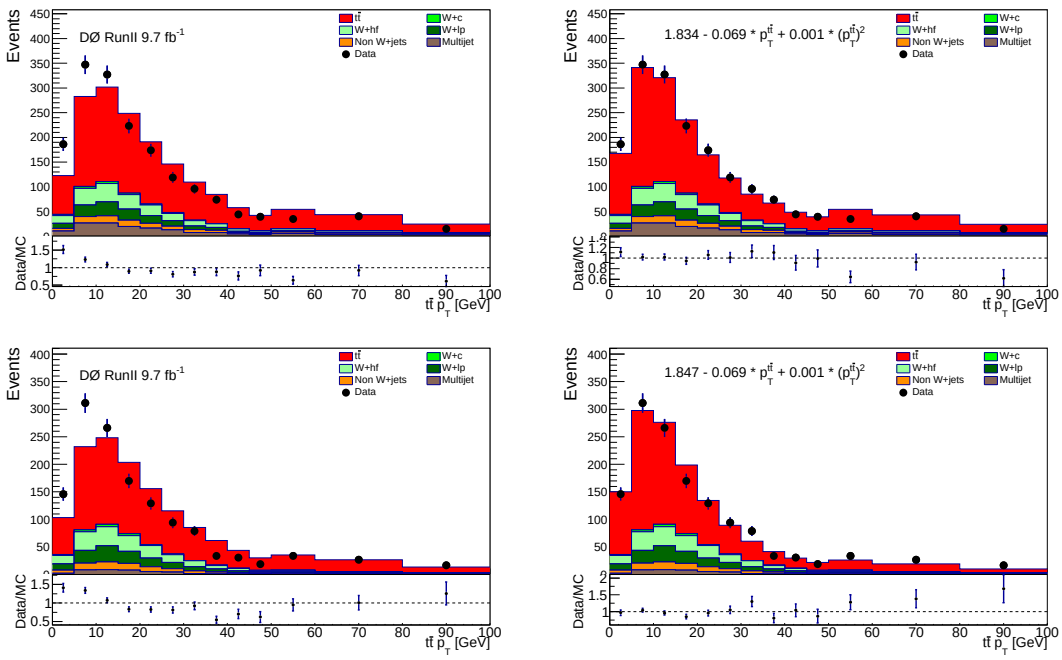

Figure 5.13: Transverse momentum of the $t\bar{t}$ pair, selection $e+ \geq 4$ jets (top), $\mu+ \geq 4$ jets (bottom) with at least 1 b-tag. The right side figures shows the same distribution after reweighting the MC $p_T^{t\bar{t}}$ distribution to the one observed in data using polynomial fit printed in the panels. This is propagated as systematic uncertainty of the measurement.

The **Parton distribution function** eigenvectors from the CTEQ6.1 PDFs are varied. In total, 20 up and down variations are defined relative to the nominal PDF of CTEQ6.1.

The Methodology represents following uncertainties associated with procedures and assumptions made in the analysis:

- A_{FB} **uncertainty** - unceratinty from the SM NNLO prediction in [95] is propagated as systematical uncertainty of the top polarization as the correlation between the two is assumed.
- **Sample composition** - the scale factors uncertainties from the sample composition fit are used to vary the number of events in MC samples and the respective uncertainty on polarization is calculated.
- **Spin correlation factor** - as mentioned in Section 5.3.4, the spin correlation factor C for transverse axis is varied by ± 1 to estimate uncertainty of our choice.

The uncertainties and the contributions from individual sources are summarized in Table 5.11.

5.5 Author Notes

This chapter describes the most essential part of this thesis, the method of the measurement itself. All the steps in the measurement of the top quark polarization in lepton+jets channel at DØ are described. As stated in the beginning of the chapter, this work has been thoroughly described by the Internal DØ Analysis Note [83] that was important document for the review process in the DØ collaboration, by the Conference Note [19] with the aim to make the result public in 2015; and by paper that has been recently published in the Physical Review D journal [84]. This has been my original work with the initial help from SungWoo Youn, and with many useful comments from the DØ collaboration members and especially from the DØ Top quark group. The methods described in each sections of this chapter are either completely original work or adapted and modified from previous DØ measurements. Top quark polarization has not been measured before at DØ with this method and in this channel (nor at the Tevatron Collider!).

I have tried to explain in more details procedures used in the analysis, the motivation and conclusion of additional studies. Through the time of the analysis, all the steps have been questioned and challenged by me and my colleagues in the Top quark group and in the DØ collaboration. This lead to the examination of every part of the analysis chain and provision of proofs that the method used, combination of variables chosen, or additional correction applied (or dismissed) are all reasonable. I have described the important cross-checks and studies, but many others are omitted in this thesis as are not essential to the description of the measurement and would increase the length of the document in a needless manner.

Source	Beam	Helicity	Transverse
Jet reconstruction			
Flavor-dependent jets response	±0.009	±0.008	±0.007
Jet identification efficiency	±0.001	±0.004	±0.003
Vertex confirmation	±0.004	±0.002	±0.004
Jet energy measurement			
Residual jet energy scale	±0.009	±0.022	±0.003
Jet energy resolution	±0.003	±0.005	±0.005
b tagging			
b tagging	±0.009	±0.014	±0.005
Background modeling			
Instantaneous luminosity	±0.000	±0.002	±0.002
Trigger efficiency	±0.002	±0.005	±0.001
Lepton identification	±0.006	±0.016	±0.002
Background normalization	±0.004	±0.003	±0.002
Multijet background	±0.001	±0.008	±0.002
Lepton momentum scale	±0.002	±0.008	±0.001
W+jets correction	±0.002	±0.003	±0.001
MC template statistics	±0.001	±0.001	±0.001
Signal modeling			
b-jet fragmentation	±0.001	±0.001	±0.000
Top quark mass	±0.002	±0.005	±0.003
Alternate signal	±0.009	±0.014	±0.003
Initial/final state radiation	±0.008	±0.003	±0.003
Color reconnection	±0.003	±0.007	±0.003
$m_{t\bar{t}}$ modeling	±0.005	±0.010	±0.000
$t\bar{t}$ transverse momentum	±0.005	±0.001	±0.002
Parton distribution functions			
PDFs	±0.013	±0.011	±0.003
Methodology			
A_{FB} uncertainty	±0.005	±0.000	±0.000
Sample composition	±0.012	±0.007	±0.004
Spin correlation factor	±0.000	±0.000	±0.008
Total systematic uncertainty	±0.030	±0.042	±0.017
Total statistical uncertainty	±0.046	±0.044	±0.030
Total uncertainty	±0.055	±0.061	±0.035

Table 5.11: Uncertainties in the top quark polarization measurement along the three axes. The numbers indicate difference in polarization when the measurement is repeated using alternative modeling, after applying uncertainties from the employed methods, or from assumptions made in the measurement.

Chapter 6
Results

In this Chapter, the measured polarizations for the three spin quantization axes are shown. The measurement has been done separately for lepton flavor (e and μ), lepton/top quark charge (ℓ^+ and ℓ^-), and number of jets. The results by lepton flavor are shown in Table 6.1 with only statistical uncertainties listed. A tension between $e+$ jets and $\mu+$ jets results is observed in the helicity and transverse axes. A study has been performed on this and after including systematic uncartainties, the difference is ≈ 2.3 standard deviations with accounting for the correlation between the systematic uncertainties of the two selections. A similar effect was previously observed by different measurements in the $\ell+$ jets channel at the DØ experiment, for example [96, 97]. Therefore, we assume this difference is mainly a statistical fluctuation and partly because of the difficulties in the reconstruction of the helicity axis.

Axis	e+jets	μ+jets	ℓ+jets
Beam	$+0.041 \pm 0.075$	$+0.112 \pm 0.064$	$+0.070 \pm 0.046$
Helicity	-0.239 ± 0.062	$+0.061 \pm 0.072$	-0.102 ± 0.044
Transverse	-0.049 ± 0.046	$+0.136 \pm 0.049$	$+0.040 \pm 0.030$

Table 6.1: Measured top quark polarizations from the $t\bar{t}$ e+jets, μ+jets, and ℓ+jets channels along the beam, helicity, and transverse axes. The listed uncertainties are only statistical.

In this measurement, the mean polarizations of the top and antitop quarks are expected to be identical because of the CP conservation. This can be verified by measuring ℓ^++jets, and ℓ^-+jets channels separately as shown in Table 6.2. Reasonable agreement within uncertainties is observed. Final test is to check if results according to the number of jets is consistent. This is shown in Table 6.2 with reasonable agreement.

Axis	ℓ^++jets	ℓ^-+jets	ℓ+jets
Beam	$+0.117 \pm 0.068$	$+0.026 \pm 0.070$	$+0.070 \pm 0.046$
Helicity	-0.151 ± 0.067	-0.043 ± 0.066	-0.102 ± 0.044
Transverse	$+0.040 \pm 0.045$	$+0.039 \pm 0.044$	$+0.040 \pm 0.030$

Table 6.2: Measured top quark polarizations from the $t\bar{t}$ ℓ^++jets, ℓ^++jets, and ℓ+jets channels along the beam, helicity, and transverse axes. The listed uncertainties are only statistical.

Axis	ℓ+3jets	ℓ+ $\geq$4jets	ℓ+jets
Beam	$+0.106 \pm 0.066$	$+0.039 \pm 0.056$	$+0.070 \pm 0.046$
Helicity	-0.051 ± 0.066	-0.115 ± 0.058	-0.102 ± 0.044
Transverse	-0.041 ± 0.049	$+0.068 \pm 0.040$	$+0.040 \pm 0.030$

Table 6.3: Measured top quark polarizations from the $t\bar{t}$ ℓ+3jets, ℓ+ $\geq$4jets, and ℓ+jets channels along the beam, helicity, and transverse axes. The listed uncertainties are only statistical.

6.1 Combination with Dilepton Measurement

The DØ Collaboration has previously measured the polarization along the beam axis in the dilepton final state [17] to be $P = 0.072 \pm 0.113$ in simultaneous measurement with the A_{FB} and $P = 0.113 \pm 0.093$ if the SM A_{FB} is assumed. For combination with this measurement in the ℓ+jets final state, the result assuming the SM NNLO A_{FB} of 9.5% is used. The uncertainties of the two measurements are studied for correlations. We consider uncertainties to be either correlated (1) or not correlated (0). Table 6.4 summarizes the correlation between uncertainties for the two measurements. As the dilepton measurement is dominated by statistical uncertainity, which is uncorrelated to ℓ+jets, as the selections are orthogonal, the overall correlation is only 5%. The dilepton and ℓ+jets measurements are consistent with the probability of 70% given by the χ^2 test. We combine the two using the Best Linear Unbiased Estimate (BLUE) method [99, 100]. The combination is a weighted average of the input measurements, the dilepton measurement was given weight of 0.25 and the ℓ+jets measurement weight of 0.75. The combination yields a top quark polarization along the beam axis of

$$P = 0.081 \pm 0.048(\text{stat.} + \text{syst.}). \tag{6.1}$$

Sources of uncertainties (groups)	ℓ+jets uncertainty	dilepton uncertainty	Correlation
Signal modeling (+ PDFs)	0.019	0.009	1.00
$b-$quark ID and tagging	0.009	0.004	1.00
Jet modeling	0.014	0.004	1.00
Background modeling	0.007	0.009	0.00
Method/Calibration/ Sample composition	0.015	0.012	0.00
Systematics uncertainty	0.030	0.019	0.48
Statistical uncertainty	0.046	0.091	0.00
Total	0.055	0.093	0.05

Table 6.4: Uncertainties and correlations for the combination of top quark polarization measurements along beam axis in the ℓ+jets and dilepton final states.

6.2 Final Results

The measured polarizations for the three spin quantization axes are shown in Table 6.5. Results on the longitudinal polarizations are visually presented in Figure 6.1, where comparison to SM predictions and several BSM models is shown. The correlations between uncertainties of the two measurements are studied in order to provide the error ellipses in the two-dimensional graph. The systematical uncertainties are considered either 100% or −100% correlated depending of the relative sign of the observed variations, resulting to correlation of 61%. The correlation for statistical uncertainties was estimated using the Jackknife resampling method, so-called grouped or delete-k Jackknife method [101]. This method is based on repeating the measurement multiple times, each time with different blocks of events removed from the sample, i.e. $N = kn_b$, where N is the original data sample, k is the block size and n_b the number of blocks. Therefore we perform n_b measurements with $(N - k)$ events. The number of data events is 9844 in total, as seen in Table 5.4. Thus, the k is chosen to be 214 and thus 46 measurements are performed to estimate the correlation. The correlation between the statistical uncertainties is then estimated to be 7%. Overall correlation of the uncertainties of the two measurements of longitudinal polarizations is 27%.

6.3 Author Notes

The results between e+jets and μ+jets are in tension, but already some other measurement in this channel at DØ observed significant differences in results of top quark properties from the electron and muon selections of ℓ+jets. There are some possible explanations: the largest difference is in the helicity axis, where we

Axis	Measured polarization	SM prediction
Beam	$+0.070 \pm 0.055$	-0.002
Beam - DØ comb.	$+0.081 \pm 0.048$	-0.002
Helicity	-0.102 ± 0.061	-0.004
Transverse	$+0.040 \pm 0.035$	$+0.011$

Table 6.5: Measured top quark polarizations from the $t\bar{t}$ ℓ+jet channel along the beam, helicity, and transverse axes. And the combined polarization for beam axis with the dilepton result by DØ. The total uncertainties are obtained by adding the statistical and systematic uncertainties in quadrature.

have to rely strongly on the top-antitop reconstruction, which is not perfect. The electron and muons are different in the view of the detector (calorimeter vs. muon system), reconstruction, selection, which might be a factor in favor for statistical fluctuation that has been observed to be at level of 2.3σ.

The transverse polarization, measured for the first time in $t\bar{t}$ production, is in very good agreement with SM prediction. For the longitudinal polarizations, a small discrepancy is observed as shown in Figure 6.1. It is less than 2 standard deviations, however. At this point, the only conclusion is that the results are in agreement with SM and the inconsistency is a result of a statistical fluctuation. Unfortunately, the DØ was shut down in 2011 and there will be no more data to continue with in this measurement. The agreement with the dilepton result for the polarization along beam axis is excellent and I was able to provide combination, which is the DØ and Tevatron legacy result in the preferable axis for the Tevatron energy.

The results have been presented at 2015 and 2016 editions of International Workshop on Top Quark Physics [102] with positive feedback from the top quark community. Especially the transverse polarization, as it was measured for the first time, was accepted as a good achievement among the theoretical and experimental physicists. The 2015 Young Scientific Forum presentation was published in the Proceedings, Ref. [18], while the 2016 edition has Proceedings in preparation.

This is my last "note" and if you managed to read this far - thank you! You are either opponent of this work and I appreciate your thorough reading, or you are interested in this topic and that means my work had some meaning. *Merci.*

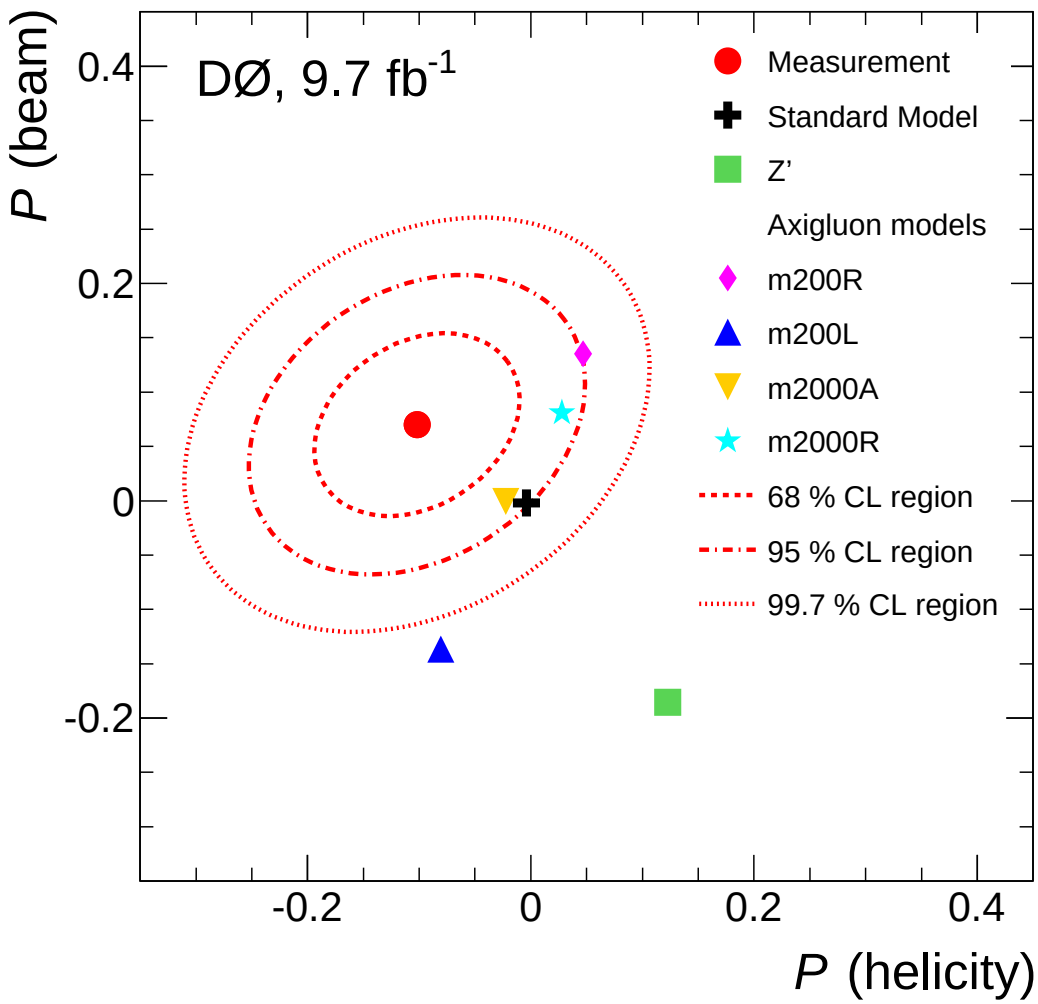

Figure 6.1: Two dimensional visualization of the longitudinal top quark polarizations in the ℓ+jets final state measured along the beam and helicity axes compared with the SM and the BSM models described in the text. In this case, the m200A model is not shown as it is indistinguishable from m2000A model. The correlation of the two measurement uncertainties is 27%.

Chapter 7
Conclusion

To conclude, this thesis presents measurement of the top quark polarization in the $t\bar{t}$ production in $p\bar{p}$ collisions at $\sqrt{s} = 1.96$ TeV along several spin-quantization axes. The polarizations are consistent with the Standard Model (SM) predictions. The transverse polarization is measured for the first time. The longitudinal polarizations, along the beam and helicity axes, are summarized in Figure 6.1 and compared to the SM and several beyond SM models. The results are compatible with SM and with several axigluons models, while the light left-handed axigluon (m200L) and Z' models are excluded with more than 99.7% probability.

These are the most precise measurements of the top quark polarization in $p\bar{p}$ collisions and the legacy measurements from the Tevatron Collider. The Tevatron Collider and DØ detector were shut down in September 2011 and there will be no more data from $p\bar{p}$ collisions to continue with this measurement. The polarization along helicity axis has been already measured by the LHC experiments and with more data and higher energies of the colliding beams, there will be more results on this topic. The beam axis is disfavored at the LHC as two colliding protons are indistinguishable in the definition of the axis and the result from this thesis might be the final word on polarization along beam axis until new collider with oppositely charged beams starts its operation. On the other hand, I believe that transverse polarization is a feasible measurement at the LHC and it is important to perform this measurement to get the confirmation of the first measurement presented here and to improve the precision to see possible effects of new physics on transverse polarization as shown in Ref. [88].

Top quark polarization has been a missing piece in the quark properties measurements from the Tevatron Collider for a long time. The measurement described in this thesis provides final answer to this property and to new physics searches in the $t\bar{t}$ events from $p\bar{p}$. Although, there has been no indication for new physics, it is an important confirmation of the SM and it provides better understanding the top quark. Searches and measurements will continue at the LHC, where apart from polarization in $t\bar{t}$ production also the polarization in single top quark production is a beneficial measurement with great potential for the future.

Bibliography

[1] S. Abachi *et al.* (D0 Collaboration), *Observation of the top quark*, Phys. Rev. Lett. **74**, 2632 (1995).

[2] F. Abe *et al.* (CDF Collaboration), *Observation of top quark production in $\bar{p}p$ collisions*, Phys. Rev. Lett. **74**, 2626 (1995).

[3] G. Aad *et al.* (ATLAS Collaboration), *Observation of a new particle in the search for the Standard Model Higgs boson with the ATLAS detector at the LHC*, Phys. Lett. B **716**, 1 (2012); S. Chatrchyan *et al.* (CMS Collaboration), *Observation of a new boson at a mass of 125 GeV with the CMS experiment at the LHC*, Phys. Lett. B **716**, 30 (2012).

[4] K. Kodama *et al.* (DONUT Collaboration), *Observation of tau neutrino interactions*, Phys. Lett. B **504**, 218 (2001).

[5] M. Kobayashi and T. Maskawa, *CP Violation in the Renormalizable Theory of Weak Interaction*, Prog. Theor. Phys. **49**, 652 (1973).

[6] A. Czarnecki, M. Jezabek and J. H. Kuhn, *Lepton Spectra From Decays of Polarized Top Quarks*, Nucl. Phys. B **351**, 70 (1991).

[7] R. H. Dalitz and G. R. Goldstein, *The Decay and polarization properties of the top quark*, Phys. Rev. D **45**, 1531 (1992).

[8] G. L. Kane, G. A. Ladinsky and C. P. Yuan, *Using the Top Quark for Testing Standard Model Polarization and CP Predictions*, Phys. Rev. D **45**, 124 (1992).

[9] W. Bernreuther, A. Brandenburg and P. Uwer, *Transverse polarization of top quark pairs at the Tevatron and the large hadron collider*, Phys. Lett. B **368**, 153 (1996).

[10] W. Bernreuther and Z.-G. Si, *Distributions and correlations for top quark pair production and decay at the Tevatron and LHC*, Nucl. Phys. B **837**, 90 (2010).

[11] V. M. Abazov et al. (D0 Collaboration), *Forward-backward asymmetry in top quark-antiquark production*, Phys. Rev. D **84**, 112005 (2011).

[12] T. Aaltonen *et al.* (CDF Collaboration), *Evidence for a Mass Dependent Forward-Backward Asymmetry in Top Quark Pair Production*, Phys. Rev. D **83**, 112003 (2011).

[13] G. Aad *et al.* (ATLAS Collaboration), *Measurement of Top Quark Polarization in Top-Antitop Events from Proton-Proton Collisions at* $\sqrt{s}$ *= 7 TeV Using the ATLAS Detector*, Phys. Rev. Lett. **111**, 232002 (2013).

[14] S. Chatrchyan *et al.* (CMS Collaboration), *Measurements of* $t\bar{t}$ *spin correlations and top-quark polarization using dilepton final states in pp collisions at* $\sqrt{s}$ *= 7 TeV*, Phys. Rev. Lett. **112**, 182001 (2014); V. Khachatryan *et al.* (CMS Collaboration), *Measurements of* $t\bar{t}$ *spin correlations and top quark polarization using dilepton final states in pp collisions at* $\sqrt{s}$ *= 8 TeV*, Phys. Rev. D **93**, 052007 (2016).

[15] J. A. Aguilar-Saavedra, *Portrait of a colour octet*, JHEP **1408**, 172 (2014); J. A. Aguilar-Saavedra, *Missing Top Properties*, in Proceedings of the 7th International Workshop on Top Quark Physics, Cannes, France, 2014 (unpublished).

[16] D. Choudhury, R. M. Godbole, S. D. Rindani and P. Saha, *Top polarization, forward-backward asymmetry and new physics*, Phys. Rev. D **84**, 014023 (2011).

[17] V. M. Abazov *et al.* (D0 Collaboration), *Simultaneous Measurement of Forward-Backward Asymmetry and Top Polarization in Dilepton Final States from* $t\bar{t}$ *Production at the Tevatron*, Phys. Rev. D **92**, 052007 (2015).

[18] K. Augsten, *Measurement of top quark polarization with the D0 detector*, PoS TOP **2015**, 032 (2016).

[19] V. M. Abazov *et al.* (D0 Collaboration) *Measurement of top quark polarization in the lepton+jets final state*, DØ Conference Note 6471 (2015), http://www-d0.fnal.gov/Run2Physics/WWW/results/prelim/TOP/T107

[20] Y. Fukuda *et al.* (Super-Kamiokande Collaboration), *Measurements of the solar neutrino flux from Super-Kamiokande's first 300 days*, Phys. Rev. Lett. **81**, 1158 (1998) Erratum: [Phys. Rev. Lett. **81**, 4279 (1998)].

[21] K. A. Olive *et al.* (Particle Data Group Collaboration), *Review of Particle Physics*, Chin. Phys. C **38**, 090001 (2014) and (2015) update..

[22] F. Englert and R. Brout, *Broken Symmetry and the Mass of Gauge Vector Mesons*, Phys. Rev. Lett. **13**, 321 (1964).

[23] P. W. Higgs, *Broken Symmetries and the Masses of Gauge Bosons*, Phys. Rev. Lett. **13**, 508 (1964).

[24] (ATLAS and CDF and CMS and D0 Collaborations), *First combination of Tevatron and LHC measurements of the top-quark mass*, arXiv:1403.4427 [hep-ex].

[25] A. Quadt, *Top quark physics at hadron colliders*, Eur. Phys. J. C **48**, 835 (2006).

[26] R. Kehoe, M. Narain and A. Kumar, *Review of Top Quark Physics Results*, Int. J. Mod. Phys. A **23**, 353 (2008).

[27] F. Deliot and D. A. Glenzinski, *Top Quark Physics at the Tevatron*, Rev. Mod. Phys. **84**, 211 (2012).

[28] M. Cristinziani and M. Mulders, *Top-quark physics at the Large Hadron Collider*, arXiv:1606.00327 [hep-ex].

[29] N. Kidonakis, *NNNLO soft-gluon corrections for the top-antitop pair production cross section*, Phys. Rev. D **90**, no. 1, 014006 (2014).

[30] V. M. Abazov *et al.* (D0 Collaboration), *Measurement of the inclusive $t\bar{t}$ production cross section in $p\bar{p}$ collisions at $\sqrt{s} = 1.96$ TeV and determination of the top quark pole mass*, arXiv:1605.06168 [hep-ex].

[31] N. Kidonakis, *NNLL resummation for s-channel single top quark production*, Phys. Rev. D **81**, 054028 (2010).

[32] N. Kidonakis, *Next-to-next-to-leading-order collinear and soft gluon corrections for t-channel single top quark production*, Phys. Rev. D **83**, 091503 (2011).

[33] M. Czakon, P. Fiedler and A. Mitov, *Total Top-Quark Pair-Production Cross Section at Hadron Colliders Through $O(\alpha_S^4)$*, Phys. Rev. Lett. **110**, 252004 (2013).

[34] V. M. Abazov *et al.* (D0 Collaboration), *Measurements of single top quark production cross sections and $|V_{tb}|$ in $p\bar{p}$ collisions at $\sqrt{s} = 1.96$ TeV*, Phys. Rev. D **84**, 112001 (2011).

[35] V. M. Abazov *et al.* (D0 Collaboration), *Precision measurement of the ratio $B(t \to Wb)/B(t \to Wq)$ and Extraction of V_{tb}*, Phys. Rev. Lett. **107**, 121802 (2011).

[36] J. Gao, C. S. Li and H. X. Zhu, *Top Quark Decay at Next-to-Next-to Leading Order in QCD*, Phys. Rev. Lett. **110**, no. 4, 042001 (2013).

[37] V. M. Abazov *et al.* (D0 Collaboration), *An Improved determination of the width of the top quark*, Phys. Rev. D **85**, 091104 (2012).

[38] V. M. Abazov *et al.* (D0 Collaboration), *Measurement of Spin Correlation between Top and Antitop Quarks Produced in $p\bar{p}$ Collisions at $\sqrt{s}$ = 1.96 TeV*, Phys. Lett. B **757**, 199 (2016).

[39] G. Aad *et al.* (ATLAS Collaboration), *Measurements of spin correlation in top-antitop quark events from proton-proton collisions at $\sqrt{s} = 7$ TeV using the ATLAS detector*, Phys. Rev. D **90**, no. 11, 112016 (2014).

[40] V. M. Abazov *et al.* (D0 Collaboration), *Precision measurement of the top-quark mass in lepton+jets final states*, Phys. Rev. D **91**, no. 11, 112003 (2015).

[41] *Fermilab Tevatron website*, http://www.fnal.gov/pub/science/accelerator/

[42] C. D. Curtis, G. M. Lee, C. W. Owen, C. W. Schmidt and W. M. Smart, *Linac H- Beam Operation And Uses At Fermilab*, IEEE Trans. Nucl. Sci. **26**, 3760 (1979); C. W. Schmidt, *The Fermilab 400 MeV Linac Upgrade*, Proc. 1993 Part. Acc. Conf., May, 1993, Washington D.C., IEEE Cat. No. 93CH3279-7, p1655.

[43] E. Hubbard *et al.*, Fermilab Technical Memo No. TM-405, 1973; *Fermilab Linac Upgrade Conceptual Design*, Fermilab Memo, Fermilab-LU-Conceptual Design, 1989.

[44] *The Fermilab Main Injector Technical Design Handbook*, FERMILAB-DESIGN-1994-01.

[45] Fermilab Beams Division, *RunII Handbook*, http://www-bd.fnal.gov/runII/index.html

[46] G. Jackson, *The Fermilab recycler ring technical design report. Rev. 1.2*, FERMILAB-TM-1991, FERMILAB-DESIGN-1996-04.

[47] R. R. Wilson, *The Tevatron*, Phys. Today **30N10**, 23 (1977).

[48] V. M. Abazov *et al.* (D0 Collaboration), *The Upgraded D0 Detector*, Nucl. Instrum. Methods Phys. Res. Sec. A **565**, 463 (2006).

[49] S. N. Ahmed *et al.* (D0 Collaboration), *The D0 Silicon Microstrip Tracker*, Nucl. Instrum. Meth. A **634**, 8 (2011).

[50] V. M. Abazov *et al.* (D0 Collaboration), *The muon system of the Run II D0 detector*, Nucl. Instrum. Methods Phys. Res. Sec. A **552**, 372 (2005).

[51] A. Khanov, *HTF: histogramming method for finding tracks. The algorithm description*, DØ Note 3778 (2000).

[52] R. Fruhwirth, *Application of Kalman filtering to track and vertex fitting*, Nucl. Instrum. Meth. A **262**, 444 (1987).

[53] A. Schwartzman, C. Tully, *Primary vertex reconstruction by means of adaptive vertex fitting*, DØ Note 4918 (2005).

[54] A. Schwartzman, M. Narain, *Probabilistic Primary Vertex Selection*, DØ Note 4042 (2002).

[55] A. Schwartzman, M. Narain, *Secondary Vertex Reconstruction using the Kalman Filter*, DØ note 3908 (2001); A. Schwartzman, M. Narain, *b quark jet identification via Secondary Vertex Reconstruction*, DØ note 4080 (2003); Y. Peters, H. Greenlee, A. Haas, A. Schwartzman, *Optimization of the Secondary Vertex Tagger in p17*, DØ note 5265 (2006).

[56] A. Abdesselam, *Comparison of H-Matrices for electron identification in D0 Run II*, DØ Note 3745 (2000).

[57] V. M. Abazov *et al.* (D0 Collaboration), *Electron and Photon Identification in the D0 Experiment*, Nucl. Instrum. Meth. A **750**, 78 (2014).

[58] V. M. Abazov *et al.* (D0 Collaboration), *Muon reconstruction and identification with the Run II D0 detector*, Nucl. Instrum. Meth. A **737**, 281 (2014).

[59] G. C. Blazey *et al.*, *Run II jet physics*, hep-ex/0005012.

[60] E. Busato, B. Andrieu, *Jet Algorithms in D0 RunII Software: Description and User's Guide*, DØ Note 4457 (2004).

[61] V. M. Abazov *et al.* (D0 Collaboration), *Improved b quark jet identification at the D0 experiment*, Nucl. Instrum. Meth. A **763**, 290 (2014).

[62] *DØ Final RunIIa Jet Energy Scale*, http://www-d0.fnal.gov/phys_id/jes/public_RunIIa/ .

[63] A. Hocker *et al.*, *TMVA, the Toolkit for Multivariate Data Analysis with ROOT*, PoS ACAT, 040 (2007).

[64] V. M. Abazov *et al.* (D0 Collaboration), *Jet energy scale determination in the D0 experiment*, Nucl. Instrum. Methods Phys. Res. Sec. A **763**, 442 (2014).

[65] B. Abbott *et al.* (D0 Collaboration), *Determination of the absolute jet energy scale in the D0 calorimeters*, Nucl. Instrum. Meth. A **424**, 352 (1999).

[66] T. Guillemin, J.-F. Grivaz, *JSSR for Run IIb*, DØ Note 6063 (2010).

[67] A. Bhatti *et al.* (CDF Collaboration), *Determination of the jet energy scale at the collider detector at Fermilab*, Nucl. Instrum. Meth. A **566**, 375 (2006).

[68] Z. Ye, M. Wang, G. Gutierrez, *Measurement of the Top Quark Mass in the Lepton+Jets Channel Using the Matrix Element Method on 3.6 fb-1 fb D0 RunII Data*, DØ Note 5877 (2009).

[69] Z. Ye, S. Atkins, K. Augsten, S. Evstyukhin, A. Juste, M. Wang, *Correction for the MC-Data Difference in the Jet Response at D0*, DØ Note 6143 (2011); Z. Ye, S. Atkins, K. Augsten, S. Evstyukhin, A. Juste, M. Wang, *Correction for the MC-Data Difference in the Jet Response at D0 for Run IIB*, DØ Note 6144 (2011); K. Augsten, Z. Ye, *Correction for the MC-Data Difference in the Jet Response at D0 for Run IIB*, DØ Note 6368 (2013).

[70] *DØ Top Triggers*, http://www-d0.fnal.gov/Run2Physics/top/d0_private/wg/triggers/triggers.html

[71] S. Frixione and B. R. Webber, *Matching NLO QCD computations and parton shower simulations*, JHEP **0206** (2002) 029; S. Frixione *et al.*, *Matching NLO QCD and parton showers in heavy flavour production*, JHEP **0308** (2003) 007.

[72] M. L. Mangano, M. Moretti, F. Piccinini, R. Pittau and A. D. Polosa, ALPGEN, *a generator for hard multiparton processes in hadronic collisions*, JHEP **0307**, 001 (2003).

[73] T. Sjostrand, S. Mrenna and P. Z. Skands, *PYTHIA 6.4 Physics and Manual*, JHEP **0605**, 026 (2006).

[74] E. Boos *et al.* (CompHEP Collaboration), *CompHEP 4.4: Automatic computations from Lagrangians to events*, Nucl. Instrum. Meth. A **534**, 250 (2004).

[75] G. Corcella *et al.*, HERWIG *6: An Event generator for hadron emission reactions with interfering gluons (including supersymmetric processes)*, JHEP **0101**, 010 (2001).

[76] J. Pumplin, *et al.*, *New generation of parton distributions with uncertainties from global QCD analysis*, JHEP **0207** (2002) 012.

[77] R. Brun and F. Carminati, CERN Program Library Long Writeup W5013 (1993) (unpublished).

[78] V. M. Abazov *et al.* (D0 Collaboration), *Measurement of the $t\bar{t}$ production cross section in $p\bar{p}$ collisions at $\sqrt{s} = 1.96$ TeV using secondary vertex b tagging*, Phys. Rev. D **74**, 112004 (2006).

[79] A. Carmona *et al.*, *From Tevatron's top and lepton-based asymmetries to the LHC*, JHEP **1407**, 005 (2014).

[80] J. Alwall *et al.*, *The automated computation of tree-level and next-to-leading order differential cross sections, and their matching to parton shower simulations*, JHEP **1407**, 079 (2014).

[81] K. Augsten, V. Bazterra, O. Brandt, A. Garcia-Bellido, A. Jung, B. Lee, D. Meister, A. Schukin, Y.-T. Tsai , *Selection of single and double top Events in the Lepton+jets Channel with 9.7 fb^{-1}*, DØ Note 6308 (2013).

[82] V. M. Abazov *et al.* (D0 Collaboration), *Measurement of the forward-backward asymmetry in the distribution of leptons in $t\bar{t}$ events in the lepton+jets channel*, Phys. Rev. D **90**, 072001 (2014).

[83] K. Augsten, S. Youn , *Measurement of the top quark polarization in the lepton+jets final state*, DØ Note 6457 (2015).

[84] V. M. Abazov *et al.* (D0 Collaboration), *Measurement of top quark polarization in $t\bar{t}$ lepton+jets final states*, submitted to: Phys.Rev.Lett., arXiv:1607.07627 [hep-ex].

[85] S. Fajfer, J. F. Kamenik and B. Melic, *Discerning New Physics in Top-Antitop Production using Top Spin Observables at Hadron Colliders*, JHEP **1208**, 114 (2012).

[86] W. Bernreuther, M. Fücker and Z.-G. Si, *Weak interaction corrections to hadronic top quark pair production: Contributions from quark-gluon and b anti-b induced reactions*, Phys. Rev. D **78**, 017503 (2008); W. Bernreuther and Z.-G. Si, unpublished e-mail communication.

[87] A. Brandenburg, Z.-G. Si and P. Uwer, *QCD corrected spin analyzing power of jets in decays of polarized top quarks*, Phys. Lett. B **539** (2002) 235.

[88] M. Baumgart and B. Tweedie, *Transverse Top Quark Polarization and the $t\bar{t}$ Forward-Backward Asymmetry*, J. High Energy Phys. **1308** (2013) 072.

[89] V. M. Abazov *et al.* (D0 Collaboration), *Measurement of Leptonic Asymmetries and Top Quark Polarization in $t\bar{t}$ Production*, Phys. Rev. D **87**, 011103 (2013).

[90] V. Khachatryan *et al.* (CMS Collaboration), *Measurement of top quark polarisation in t-channel single top quark production*, JHEP **1604**, 073 (2016).

[91] B. A. Betchart, R. Demina and A. Harel, *Analytic solutions for neutrino momenta in decay of top quarks*, Nucl. Instrum. Meth. A **736**, 169 (2014).

[92] R. Demina, A. Harel and D. Orbaker, *Reconstructing $t\bar{t}$ events with one lost jet*, Nucl. Instrum. Methods Phys. Res. Sec. A **788**, 128 (2015).

[93] V. M. Abazov *et al.* (D0 Collaboration), *Measurement of the $t\bar{t}$ production cross section in $p\bar{p}$ collisions at $\sqrt{s}$=1.96 TeV using kinematic characteristics of lepton + jets events*, Phys. Rev. D **76**, 092007 (2007).

[94] W. Bernreuther, *Top quark physics at the LHC*, J. Phys. G **35**, 083001 (2008).

[95] M. Czakon, P. Fiedler and A. Mitov, *Resolving the Tevatron Top Quark Forward-Backward Asymmetry Puzzle: Fully Differential Next-to-Next-to-Leading-Order Calculation*, Phys. Rev. Lett. **115**, 052001 (2015).

[96] V. M. Abazov *et al.* (D0 Collaboration), *Measurement of the forward-backward asymmetry in top quark-antiquark production in $p\bar{p}$ collisions using the lepton+jets channel*, Phys. Rev. D **90**, 072011 (2014).

[97] V. M. Abazov *et al.* (D0 Collaboration), *Measurement of differential $t\bar{t}$ production cross sections in $p\bar{p}$ collisions*, Phys. Rev. D **90**, 092006 (2014).

[98] M. Czakon, P. Fiedler, D. Heymes and A. Mitov, *NNLO QCD predictions for fully-differential top-quark pair production at the Tevatron*, JHEP **1605**, 034 (2016).

[99] L. Lyons, D. Gibaut and P. Clifford, *How to Combine Correlated Estimates of a Single Physical Quantity*, Nucl. Instrum. Meth. A **270**, 110 (1988).

[100] A. Valassi, *Combining correlated measurements of several different physical quantities*, Nucl. Instrum. Meth. A **500**, 391 (2003).

[101] B. Efron, *The jackknife, the bootstrap and other resampling plans*, Philadelphia: Society for industrial and applied mathematics (1982).

[102] *8th International Workshop on Top Quark Physics*, http://http://top2015.infn.it/ ; *9th International Workshop on Top Quark Physics*, http://http://top2016.particle.cz/ .

Appendix A
Control Plots

Additional control distributions are shown in this Section. Figures A.1–A.3 represent the input variables for the likelihood discriminant used in the sample composition fit and Figures A.4 and A.5 show the illustration of the sample composition fit on the discriminant distribution.

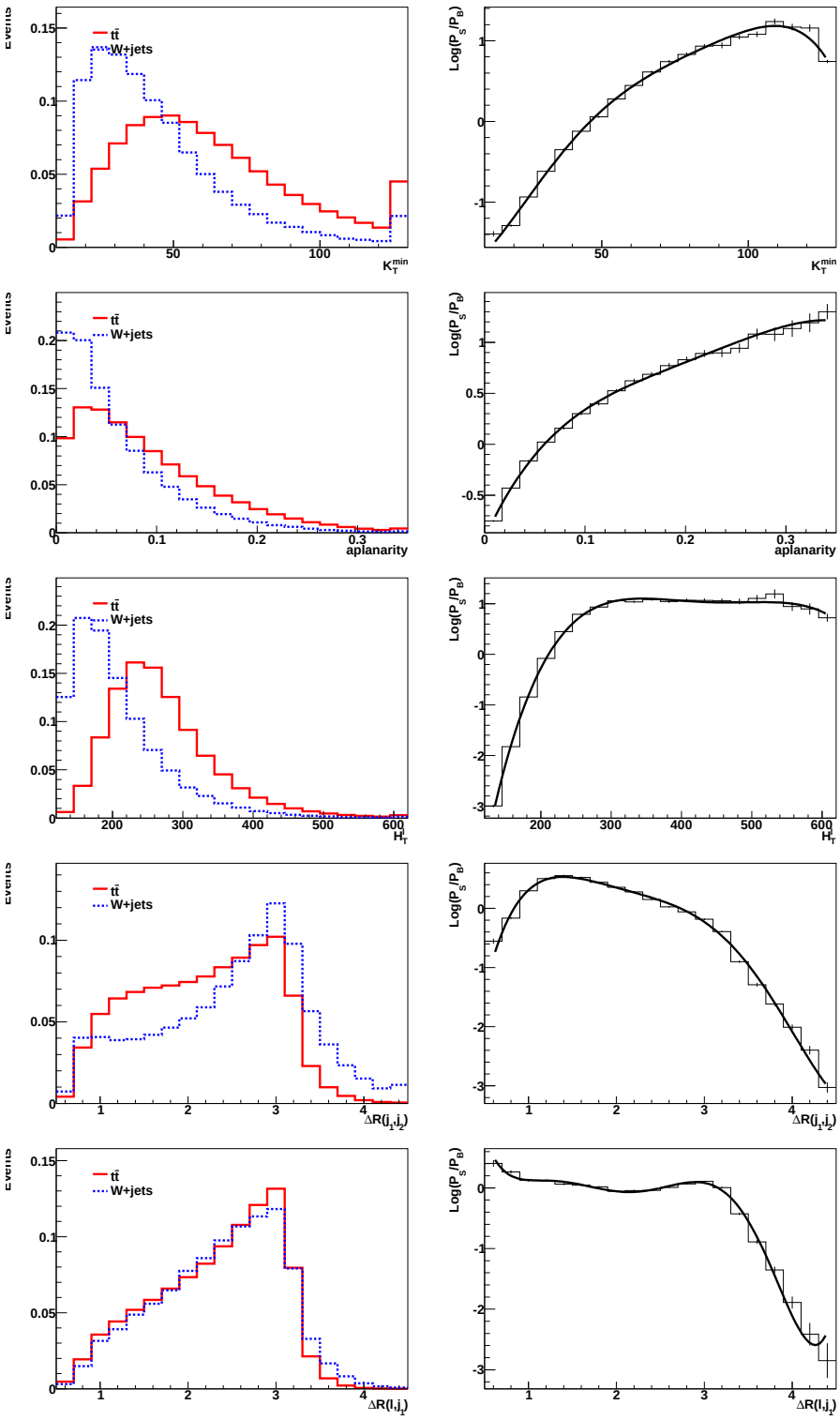

Figure A.1: Distributions of input variables the likelihood discriminant in the $e+3$ jets channel. Distributions of $t\bar{t}$ signal (red solid line) and W+jets background (blue dashed line) are on the left and the right side shows polynomial fit on the logarithms of the ratios of the signal and background events.

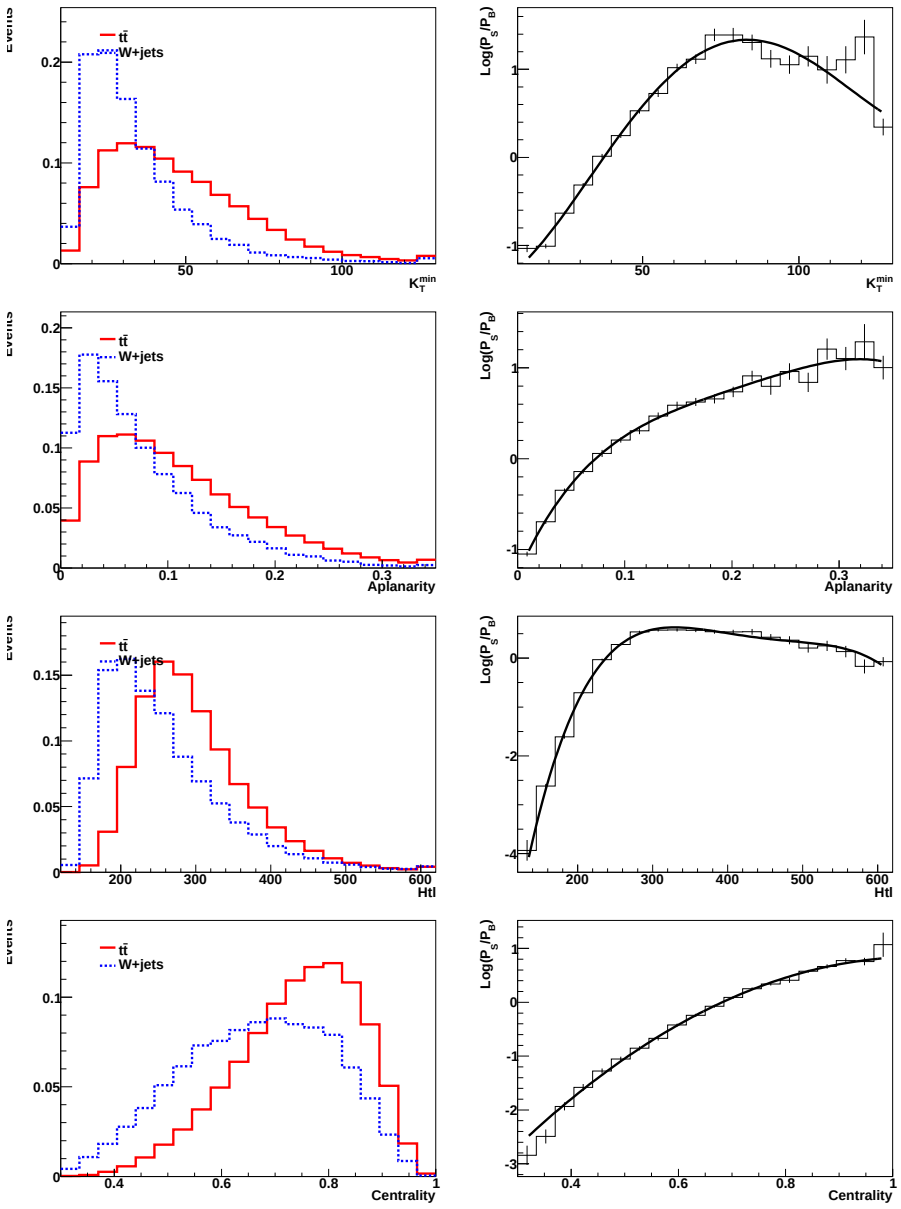

Figure A.2: Distributions of input variables the likelihood discriminant in the $e+ \geq 4$ jets channel. Distributions of $t\bar{t}$ signal (red solid line) and W+jets background (blue dashed line) are on the left and the right side shows polynomial fit on the logarithms of the ratios of the signal and background events.

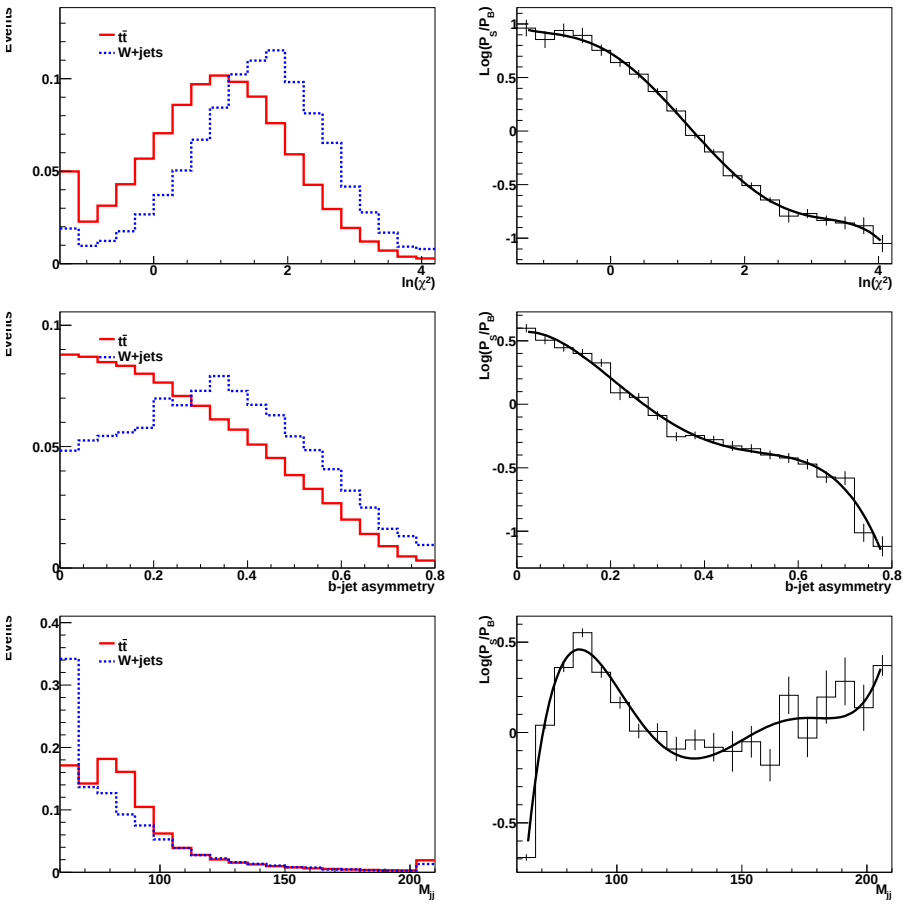

Figure A.3: Distributions of input variables the likelihood discriminant in the $e+ \geq 4$ jets channel. Distributions of $t\bar{t}$ signal (red solid line) and W+jets background (blue dashed line) are on the left and the right side shows polynomial fit on the logarithms of the ratios of the signal and background events.

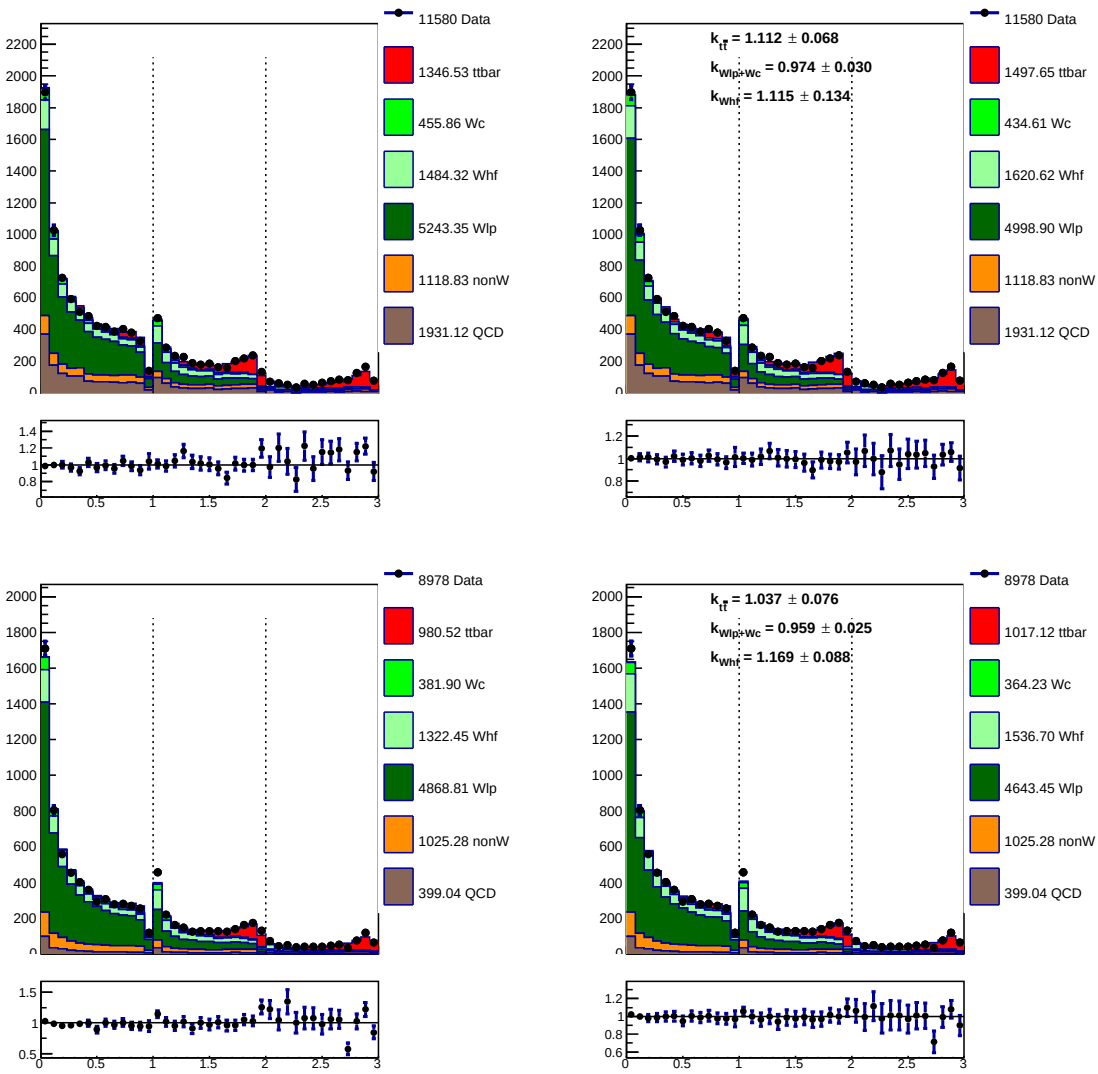

Figure A.4: The likelihood discriminant distributions in the $e+3$ jets (top) and $\mu+4$ jets (bottom) channels, before (left) and after (right) the sample composition fit. The evaluated k-factors are shown on the right. The dashed lines divide the plot to the three selections with 0, 1, ≥ 2 b-tagged jets.

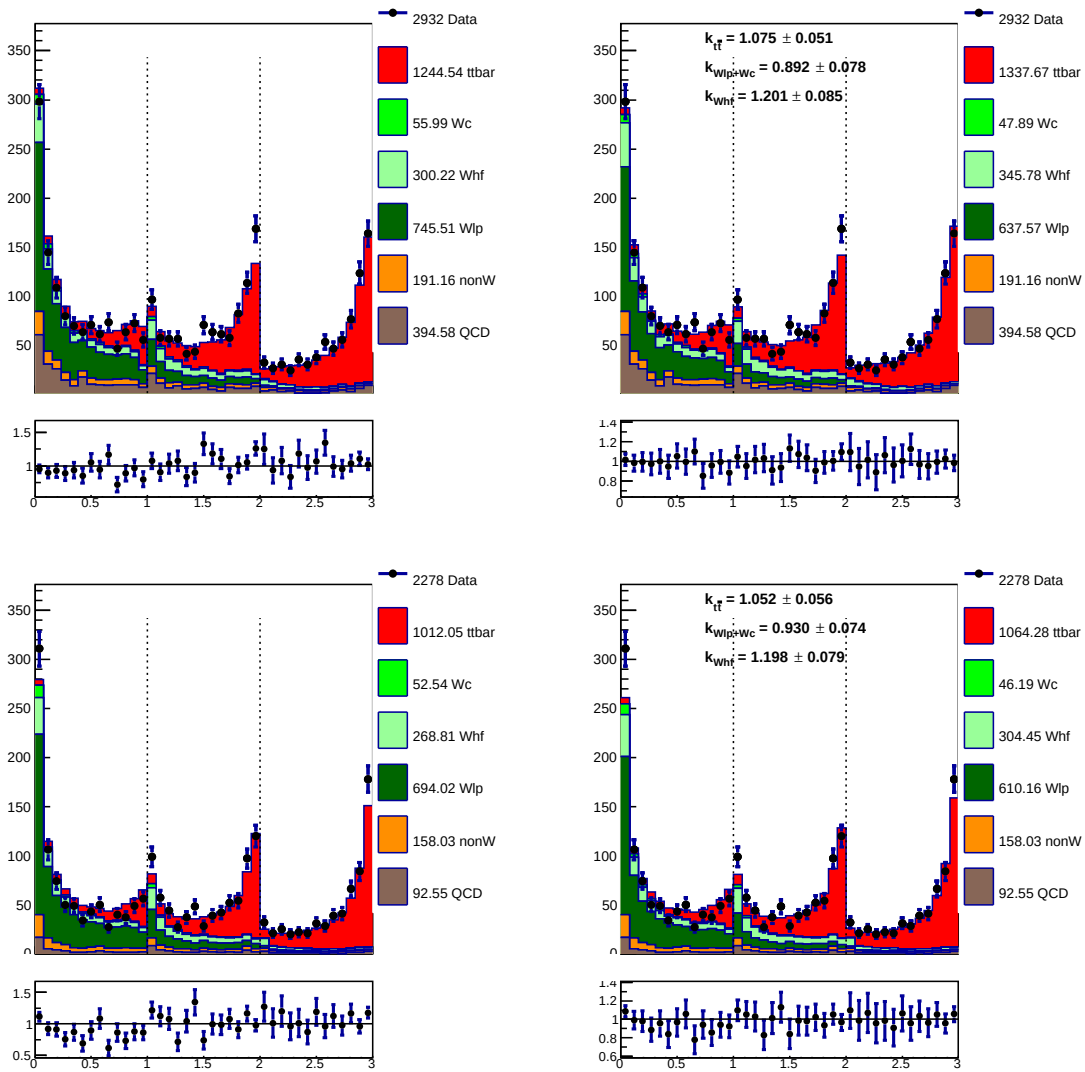

Figure A.5: The likelihood discriminant distributions in the $e+ \geq 4$ jets (top) and $\mu+ \geq 4$ jets (bottom) channels, before (left) and after (right) the sample composition fit. The evaluated k-factors are shown on the right. The dashed lines divide the plot to the three selections with 0, 1, ≥ 2 b-tagged jets.

Appendix B

Journal Paper

Following pages are the included paper, published in the Physical Review D (Rapid Communication) journal, about the top quark polarization, the topic of this thesis and the main output of this measurement.

FERMILAB-PUB-16-284-E

Measurement of top quark polarization in $t\bar{t}$ lepton+jets final states

V.M. Abazov,[31] B. Abbott,[67] B.S. Acharya,[25] M. Adams,[46] T. Adams,[44] J.P. Agnew,[41] G.D. Alexeev,[31] G. Alkhazov,[35] A. Alton[a],[56] A. Askew,[44] S. Atkins,[54] K. Augsten,[7] V. Aushev,[38] Y. Aushev,[38] C. Avila,[5] F. Badaud,[10] L. Bagby,[45] B. Baldin,[45] D.V. Bandurin,[74] S. Banerjee,[25] E. Barberis,[55] P. Baringer,[53] J.F. Bartlett,[45] U. Bassler,[15] V. Bazterra,[46] A. Bean,[53] M. Begalli,[2] L. Bellantoni,[45] S.B. Beri,[23] G. Bernardi,[14] R. Bernhard,[19] I. Bertram,[39] M. Besançon,[15] R. Beuselinck,[40] P.C. Bhat,[45] S. Bhatia,[58] V. Bhatnagar,[23] G. Blazey,[47] S. Blessing,[44] K. Bloom,[59] A. Boehnlein,[45] D. Boline,[64] E.E. Boos,[33] G. Borissov,[39] M. Borysova[l],[38] A. Brandt,[71] O. Brandt,[20] M. Brochmann,[75] R. Brock,[57] A. Bross,[45] D. Brown,[14] X.B. Bu,[45] M. Buehler,[45] V. Buescher,[21] V. Bunichev,[33] S. Burdin[b],[39] C.P. Buszello,[37] E. Camacho-Pérez,[28] B.C.K. Casey,[45] H. Castilla-Valdez,[28] S. Caughron,[57] S. Chakrabarti,[64] K.M. Chan,[51] A. Chandra,[73] E. Chapon,[15] G. Chen,[53] S.W. Cho,[27] S. Choi,[27] B. Choudhary,[24] S. Cihangir[‡],[45] D. Claes,[59] J. Clutter,[53] M. Cooke[k],[45] W.E. Cooper,[45] M. Corcoran,[73] F. Couderc,[15] M.-C. Cousinou,[12] J. Cuth,[21] D. Cutts,[70] A. Das,[72] G. Davies,[40] S.J. de Jong,[29,30] E. De La Cruz-Burelo,[28] F. Déliot,[15] R. Demina,[63] D. Denisov,[45] S.P. Denisov,[34] S. Desai,[45] C. Deterre[c],[41] K. DeVaughan,[59] H.T. Diehl,[45] M. Diesburg,[45] P.F. Ding,[41] A. Dominguez,[59] A. Dubey,[24] L.V. Dudko,[33] A. Duperrin,[12] S. Dutt,[23] M. Eads,[47] D. Edmunds,[57] J. Ellison,[43] V.D. Elvira,[45] Y. Enari,[14] H. Evans,[49] A. Evdokimov,[46] V.N. Evdokimov,[34] A. Fauré,[15] L. Feng,[47] T. Ferbel,[63] F. Fiedler,[21] F. Filthaut,[29,30] W. Fisher,[57] H.E. Fisk,[45] M. Fortner,[47] H. Fox,[39] J. Franc,[7] S. Fuess,[45] P.H. Garbincius,[45] A. Garcia-Bellido,[63] J.A. García-González,[28] V. Gavrilov,[32] W. Geng,[12,57] C.E. Gerber,[46] Y. Gershtein,[60] G. Ginther,[45] O. Gogota,[38] G. Golovanov,[31] P.D. Grannis,[64] S. Greder,[16] H. Greenlee,[45] G. Grenier,[17] Ph. Gris,[10] J.-F. Grivaz,[13] A. Grohsjean[c],[15] S. Grünendahl,[45] M.W. Grünewald,[26] T. Guillemin,[13] G. Gutierrez,[45] P. Gutierrez,[67] J. Haley,[68] L. Han,[4] K. Harder,[41] A. Harel,[63] J.M. Hauptman,[52] J. Hays,[40] T. Head,[41] T. Hebbeker,[18] D. Hedin,[47] H. Hegab,[68] A.P. Heinson,[43] U. Heintz,[70] C. Hensel,[1] I. Heredia-De La Cruz[d],[28] K. Herner,[45] G. Hesketh[f],[41] M.D. Hildreth,[51] R. Hirosky,[74] T. Hoang,[44] J.D. Hobbs,[64] B. Hoeneisen,[9] J. Hogan,[73] M. Hohlfeld,[21] J.L. Holzbauer,[58] I. Howley,[71] Z. Hubacek,[7,15] V. Hynek,[7] I. Iashvili,[62] Y. Ilchenko,[72] R. Illingworth,[45] A.S. Ito,[45] S. Jabeen[m],[45] M. Jaffré,[13] A. Jayasinghe,[67] M.S. Jeong,[27] R. Jesik,[40] P. Jiang[‡],[4] K. Johns,[42] E. Johnson,[57] M. Johnson,[45] A. Jonckheere,[45] P. Jonsson,[40] J. Joshi,[43] A.W. Jung[o],[45] A. Juste,[36] E. Kajfasz,[12] D. Karmanov,[33] I. Katsanos,[59] M. Kaur,[23] R. Kehoe,[72] S. Kermiche,[12] N. Khalatyan,[45] A. Khanov,[68] A. Kharchilava,[62] Y.N. Kharzheev,[31] I. Kiselevich,[32] J.M. Kohli,[23] A.V. Kozelov,[34] J. Kraus,[58] A. Kumar,[62] A. Kupco,[8] T. Kurča,[17] V.A. Kuzmin,[33] S. Lammers,[49] P. Lebrun,[17] H.S. Lee,[27] S.W. Lee,[52] W.M. Lee,[45] X. Lei,[42] J. Lellouch,[14] D. Li,[14] H. Li,[74] L. Li,[43] Q.Z. Li,[45] J.K. Lim,[27] D. Lincoln,[45] J. Linnemann,[57] V.V. Lipaev[‡],[34] R. Lipton,[45] H. Liu,[72] Y. Liu,[4] A. Lobodenko,[35] M. Lokajicek,[8] R. Lopes de Sa,[45] R. Luna-Garcia[g],[28] A.L. Lyon,[45] A.K.A. Maciel,[1] R. Madar,[19] R. Magaña-Villalba,[28] S. Malik,[59] V.L. Malyshev,[31] J. Mansour,[20] J. Martínez-Ortega,[28] R. McCarthy,[64] C.L. McGivern,[41] M.M. Meijer,[29,30] A. Melnitchouk,[45] D. Menezes,[47] P.G. Mercadante,[3] M. Merkin,[33] A. Meyer,[18] J. Meyer[i],[20] F. Miconi,[16] N.K. Mondal,[25] M. Mulhearn,[74] E. Nagy,[12] M. Narain,[70] R. Nayyar,[42] H.A. Neal,[56] J.P. Negret,[5] P. Neustroev,[35] H.T. Nguyen,[74] T. Nunnemann,[22] J. Orduna,[70] N. Osman,[12] A. Pal,[71] N. Parashar,[50] V. Parihar,[70] S.K. Park,[27] R. Partridge[e],[70] N. Parua,[49] A. Patwa[j],[65] B. Penning,[40] M. Perfilov,[33] Y. Peters,[41] K. Petridis,[41] G. Petrillo,[63] P. Pétroff,[13] M.-A. Pleier,[65] V.M. Podstavkov,[45] A.V. Popov,[34] M. Prewitt,[73] D. Price,[41] N. Prokopenko,[34] J. Qian,[56] A. Quadt,[20] B. Quinn,[58] P.N. Ratoff,[39] I. Razumov,[34] I. Ripp-Baudot,[16] F. Rizatdinova,[68] M. Rominsky,[45] A. Ross,[39] C. Royon,[8] P. Rubinov,[45] R. Ruchti,[51] G. Sajot,[11] A. Sánchez-Hernández,[28] M.P. Sanders,[22] A.S. Santos[h],[1] G. Savage,[45] M. Savitskyi,[38] L. Sawyer,[54] T. Scanlon,[40] R.D. Schamberger,[64] Y. Scheglov,[35] H. Schellman,[69,48] M. Schott,[21] C. Schwanenberger,[41] R. Schwienhorst,[57] J. Sekaric,[53] H. Severini,[67] E. Shabalina,[20] V. Shary,[15] S. Shaw,[41] A.A. Shchukin,[34] O. Shkola,[38] V. Simak,[7] P. Skubic,[67] P. Slattery,[63] G.R. Snow,[59] J. Snow,[66] S. Snyder,[65] S. Söldner-Rembold,[41] L. Sonnenschein,[18] K. Soustruznik,[6] J. Stark,[11] N. Stefaniuk,[38] D.A. Stoyanova,[34] M. Strauss,[67] L. Suter,[41] P. Svoisky,[74] M. Titov,[15] V.V. Tokmenin,[31] Y.-T. Tsai,[63] D. Tsybychev,[64] B. Tuchming,[15] C. Tully,[61] L. Uvarov,[35] S. Uvarov,[35] S. Uzunyan,[47] R. Van Kooten,[49] W.M. van Leeuwen,[29] N. Varelas,[46] E.W. Varnes,[42] I.A. Vasilyev,[34] A.Y. Verkheev,[31] L.S. Vertogradov,[31] M. Verzocchi,[45] M. Vesterinen,[41] D. Vilanova,[15] P. Vokac,[7] H.D. Wahl,[44] M.H.L.S. Wang,[45] J. Warchol,[51] G. Watts,[75] M. Wayne,[51] J. Weichert,[21] L. Welty-Rieger,[48] M.R.J. Williams[n],[49] G.W. Wilson,[53] M. Wobisch,[54] D.R. Wood,[55] T.R. Wyatt,[41] Y. Xie,[45] R. Yamada,[45] S. Yang,[4] T. Yasuda,[45] Y.A. Yatsunenko,[31] W. Ye,[64] Z. Ye,[45] H. Yin,[45] K. Yip,[65] S.W. Youn,[45] J.M. Yu,[56]

J. Zennamo,[62] T.G. Zhao,[41] B. Zhou,[56] J. Zhu,[56] M. Zielinski,[63] D. Zieminska,[49] and L. Zivkovic[p14]
(The D0 Collaboration*)

[1]*LAFEX, Centro Brasileiro de Pesquisas Físicas, Rio de Janeiro, Rio de Janeiro 22290, Brazil*
[2]*Universidade do Estado do Rio de Janeiro, Rio de Janeiro, Rio de Janeiro 20550, Brazil*
[3]*Universidade Federal do ABC, Santo André, São Paulo 09210, Brazil*
[4]*University of Science and Technology of China, Hefei 230026, People's Republic of China*
[5]*Universidad de los Andes, Bogotá, 111711, Colombia*
[6]*Charles University, Faculty of Mathematics and Physics, Center for Particle Physics, 116 36 Prague 1, Czech Republic*
[7]*Czech Technical University in Prague, 116 36 Prague 6, Czech Republic*
[8]*Institute of Physics, Academy of Sciences of the Czech Republic, 182 21 Prague, Czech Republic*
[9]*Universidad San Francisco de Quito, Quito 170157, Ecuador*
[10]*LPC, Université Blaise Pascal, CNRS/IN2P3, Clermont, F-63178 Aubière Cedex, France*
[11]*LPSC, Université Joseph Fourier Grenoble 1, CNRS/IN2P3, Institut National Polytechnique de Grenoble, F-38026 Grenoble Cedex, France*
[12]*CPPM, Aix-Marseille Université, CNRS/IN2P3, F-13288 Marseille Cedex 09, France*
[13]*LAL, Univ. Paris-Sud, CNRS/IN2P3, Université Paris-Saclay, F-91898 Orsay Cedex, France*
[14]*LPNHE, Universités Paris VI and VII, CNRS/IN2P3, F-75005 Paris, France*
[15]*CEA Saclay, Irfu, SPP, F-91191 Gif-Sur-Yvette Cedex, France*
[16]*IPHC, Université de Strasbourg, CNRS/IN2P3, F-67037 Strasbourg, France*
[17]*IPNL, Université Lyon 1, CNRS/IN2P3, F-69622 Villeurbanne Cedex, France and Université de Lyon, F-69361 Lyon CEDEX 07, France*
[18]*III. Physikalisches Institut A, RWTH Aachen University, 52056 Aachen, Germany*
[19]*Physikalisches Institut, Universität Freiburg, 79085 Freiburg, Germany*
[20]*II. Physikalisches Institut, Georg-August-Universität Göttingen, 37073 Göttingen, Germany*
[21]*Institut für Physik, Universität Mainz, 55099 Mainz, Germany*
[22]*Ludwig-Maximilians-Universität München, 80539 München, Germany*
[23]*Panjab University, Chandigarh 160014, India*
[24]*Delhi University, Delhi-110 007, India*
[25]*Tata Institute of Fundamental Research, Mumbai-400 005, India*
[26]*University College Dublin, Dublin 4, Ireland*
[27]*Korea Detector Laboratory, Korea University, Seoul, 02841, Korea*
[28]*CINVESTAV, Mexico City 07360, Mexico*
[29]*Nikhef, Science Park, 1098 XG Amsterdam, Netherlands*
[30]*Radboud University Nijmegen, 6525 AJ Nijmegen, Netherlands*
[31]*Joint Institute for Nuclear Research, Dubna 141980, Russia*
[32]*Institute for Theoretical and Experimental Physics, Moscow 117259, Russia*
[33]*Moscow State University, Moscow 119991, Russia*
[34]*Institute for High Energy Physics, Protvino, Moscow region 142281, Russia*
[35]*Petersburg Nuclear Physics Institute, St. Petersburg 188300, Russia*
[36]*Institució Catalana de Recerca i Estudis Avançats (ICREA) and Institut de Física d'Altes Energies (IFAE), 08193 Bellaterra (Barcelona), Spain*
[37]*Uppsala University, 751 05 Uppsala, Sweden*
[38]*Taras Shevchenko National University of Kyiv, Kiev, 01601, Ukraine*
[39]*Lancaster University, Lancaster LA1 4YB, United Kingdom*
[40]*Imperial College London, London SW7 2AZ, United Kingdom*
[41]*The University of Manchester, Manchester M13 9PL, United Kingdom*
[42]*University of Arizona, Tucson, Arizona 85721, USA*
[43]*University of California Riverside, Riverside, California 92521, USA*
[44]*Florida State University, Tallahassee, Florida 32306, USA*
[45]*Fermi National Accelerator Laboratory, Batavia, Illinois 60510, USA*
[46]*University of Illinois at Chicago, Chicago, Illinois 60607, USA*
[47]*Northern Illinois University, DeKalb, Illinois 60115, USA*
[48]*Northwestern University, Evanston, Illinois 60208, USA*
[49]*Indiana University, Bloomington, Indiana 47405, USA*
[50]*Purdue University Calumet, Hammond, Indiana 46323, USA*
[51]*University of Notre Dame, Notre Dame, Indiana 46556, USA*
[52]*Iowa State University, Ames, Iowa 50011, USA*
[53]*University of Kansas, Lawrence, Kansas 66045, USA*
[54]*Louisiana Tech University, Ruston, Louisiana 71272, USA*
[55]*Northeastern University, Boston, Massachusetts 02115, USA*
[56]*University of Michigan, Ann Arbor, Michigan 48109, USA*
[57]*Michigan State University, East Lansing, Michigan 48824, USA*

[58]University of Mississippi, University, Mississippi 38677, USA
[59]University of Nebraska, Lincoln, Nebraska 68588, USA
[60]Rutgers University, Piscataway, New Jersey 08855, USA
[61]Princeton University, Princeton, New Jersey 08544, USA
[62]State University of New York, Buffalo, New York 14260, USA
[63]University of Rochester, Rochester, New York 14627, USA
[64]State University of New York, Stony Brook, New York 11794, USA
[65]Brookhaven National Laboratory, Upton, New York 11973, USA
[66]Langston University, Langston, Oklahoma 73050, USA
[67]University of Oklahoma, Norman, Oklahoma 73019, USA
[68]Oklahoma State University, Stillwater, Oklahoma 74078, USA
[69]Oregon State University, Corvallis, Oregon 97331, USA
[70]Brown University, Providence, Rhode Island 02912, USA
[71]University of Texas, Arlington, Texas 76019, USA
[72]Southern Methodist University, Dallas, Texas 75275, USA
[73]Rice University, Houston, Texas 77005, USA
[74]University of Virginia, Charlottesville, Virginia 22904, USA
[75]University of Washington, Seattle, Washington 98195, USA

(Dated: July 27, 2016)

We present a measurement of top quark polarization in $t\bar{t}$ pair production in $p\bar{p}$ collisions at $\sqrt{s} = 1.96\,\text{TeV}$ using data corresponding to $9.7\,\text{fb}^{-1}$ of integrated luminosity recorded with the D0 detector at the Fermilab Tevatron Collider. We consider final states containing a lepton and at least three jets. The polarization is measured through the distribution of lepton angles along three axes: the beam axis, the helicity axis, and the transverse axis normal to the $t\bar{t}$ production plane. This is the first measurement of top quark polarization at the Tevatron using lepton+jet final states and the first measurement of the transverse polarization in $t\bar{t}$ production. The observed distributions are consistent with standard model predictions of nearly no polarization.

I. INTRODUCTION

The standard model (SM) predicts that top quarks produced at the Tevatron collider are almost unpolarized, while models beyond the standard model (BSM) predict enhanced polarizations [1]. The top quark polarization $P_{\hat{n}}$ can be measured in the top quark rest frame through the angular distributions of the top quark decay products relative to some chosen axis $\hat{n}$ [2],

$$\frac{1}{\Gamma}\frac{d\Gamma}{d\cos\theta_{i,\hat{n}}} = \frac{1}{2}(1 + P_{\hat{n}}\kappa_i\cos\theta_{i,\hat{n}}), \qquad (1)$$

where i is the decay product (lepton, quark, or neutrino), κ_i is its spin-analyzing power (≈ 1 for charged leptons, 0.97 for d-type quarks, -0.4 for b-quarks, and -0.3 for neutrinos and u-type quarks [3]), and $\theta_{i,\hat{n}}$ is the angle between the direction of the decay product i and the quantization axis $\hat{n}$. The mean polarizations of the top and antitop quarks are expected to be identical because of CP conservation. The $P_{\hat{n}}$ can be obtained from the asymmetry of the $\cos\theta$ distribution

$$A_{P,\hat{n}} = \frac{N(\cos\theta_{i,\hat{n}} > 0) - N(\cos\theta_{i,\hat{n}} < 0)}{N(\cos\theta_{i,\hat{n}} > 0) + N(\cos\theta_{i,\hat{n}} < 0)}, \qquad (2)$$

where $N(x)$ is the number of events passing the requirement x and the polarization is then $P_{\hat{n}} = 2A_{P,\hat{n}}$. The quantization axes are defined in the $t\bar{t}$ rest frame, while the decay product directions are defined after successively boosting the particles to the $t\bar{t}$ rest frame and then to the parent top quark rest frame. We measure the polarization along three quantization axes: (i) the **beam axis** $\hat{n}_p$, given by the direction of the proton beam [2]; (ii) the **helicity axis** $\hat{n}_h$, given by the direction of the parent top or antitop quark; and the (iii) **transverse axis** $\hat{n}_T$, given as perpendicular to the production plane defined by the proton and parent top quark directions, i.e., $\hat{n}_p \times \hat{n}_t$ (or by $\hat{n}_p \times -\hat{n}_{\bar{t}}$ for the antitop quark) [4, 5].

The D0 Collaboration published a short study of the top quark polarization along the helicity axis in $p\bar{p}$ collisions as part of the measurement of angular asymmetries of leptons [6], but no measured value was presented. Recently, the D0 Collaboration measured the top quark polarization along the beam axis in $t\bar{t}$ final states with two leptons [7], finding it to be consistent with the SM. The ATLAS and CMS collaborations measured the top quark

*with visitors from [a]Augustana College, Sioux Falls, SD 57197, USA, [b]The University of Liverpool, Liverpool L69 3BX, UK, [c]Deutshes Elektronen-Synchrotron (DESY), Notkestrasse 85, Germany, [d]CONACyT, M-03940 Mexico City, Mexico, [e]SLAC, Menlo Park, CA 94025, USA, [f]University College London, London WC1E 6BT, UK, [g]Centro de Investigacion en Computacion - IPN, CP 07738 Mexico City, Mexico, [h]Universidade Estadual Paulista, São Paulo, SP 01140, Brazil, [i]Karlsruher Institut für Technologie (KIT) - Steinbuch Centre for Computing (SCC), D-76128 Karlsruhe, Germany, [j]Office of Science, U.S. Department of Energy, Washington, D.C. 20585, USA, [k]American Association for the Advancement of Science, Washington, D.C. 20005, USA, [l]Kiev Institute for Nuclear Research (KINR), Kyiv 03680, Ukraine, [m]University of Maryland, College Park, MD 20742, USA, [n]European Orgnaization for Nuclear Research (CERN), CH-1211 Geneva, Switzerland, [o]Purdue University, West Lafayette, IN 47907, USA, and [p]Institute of Physics, Belgrade, Belgrade, Serbia. ‡Deceased.

polarization along the helicity axis in pp collisions, and the results are consistent with no polarization [8, 9]. The polarization at the Tevatron and LHC are expected to be different because of the difference in the initial states, which motivates the measurement of the polarizations in Tevatron data [10, 11]. For beam and transverse axes, the top quark polarizations in $p\bar{p}$ collisions are expected to be larger than those for pp [2, 4], therefore offering greater sensitivity to BSM models with nonzero polarization.

The longitudinal polarizations along the beam and helicity axes at the Tevatron collider are predicted by the SM to be $(-0.19 \pm 0.05)\%$ and $(-0.39 \pm 0.04)\%$ [12], respectively, while the transverse polarization is estimated to be $\approx 1.1\%$ [5]. Observation of a significant departure from the expected value would be evidence for BSM contributions to the top quark polarization [1].

We present a measurement of top quark polarization in ℓ+jets final states of $t\bar{t}$ production using data collected with the D0 detector [13], corresponding to an integrated luminosity of $9.7\,\mathrm{fb}^{-1}$ of $p\bar{p}$ collisions at $\sqrt{s} = 1.96\,\mathrm{TeV}$. The lepton is most sensitive to the polarization and is easily identified. We therefore examine the angular distribution of leptons. After selecting the events in the ℓ+jets final state, we perform a kinematic fit to reconstruct the lepton angles relative to the various axes. The resulting distributions are fitted with mixtures of signal templates with $+1$ and -1 polarizations to extract the observed values. The down-type quark has an analyzing power close to unity, but its identification is difficult. It is therefore not used in the measurement. However, to gain statistical precision we use reweighted Monte Carlo (MC) down-type quark distributions in forming signal event templates.

II. EVENT SELECTION

Each top quark of the $t\bar{t}$ pair decays into a b quark and a W boson with nearly 100% probability, leading to a $W^+W^-b\bar{b}$ final state. In ℓ+jets events, one of the W bosons decays leptonically and the other into quarks that evolve into jets. The trigger selects ℓ+jets events with at least one lepton, electron (e) or a muon (μ). The efficiency of the trigger is 95% or 80% for $t\bar{t}$ events containing reconstructed e or μ candidates, respectively. This analysis requires the presence of one isolated e [14] or μ [15] with transverse momentum $p_T > 20\,\mathrm{GeV}$ and physics pseudorapidity [16] $|\eta| < 1.1$ or $|\eta| < 2$, respectively. In addition, leptons are required to originate from within 1 cm of the primary $p\bar{p}$ interaction vertex (PV) in the coordinate along the beam axis. Accepted events must have a reconstructed PV within 60 cm of the center of the detector along the beam axis. Furthermore, we require an imbalance in transverse momentum $\not{p}_\mathrm{T} > 20\,\mathrm{GeV}$, expected from the undetected neutrino. Jets are reconstructed using an iterative cone algorithm [17] with a cone parameter of $R = 0.5$. Jet energies are corrected to the particle level using calibrations from studies of exclusive γ+jet, Z+jet, and dijet events [18]. These calibrations account for differences in the detector response to jets originating from gluons, b quarks, and u, d, s, or c quarks. We require at least three jets with $p_T > 20\,\mathrm{GeV}$ within $|\eta| < 2.5$, and $p_T > 40\,\mathrm{GeV}$ for the jet of highest p_T. At least one jet per event is required to be identified as originating from a b quark (b tagged) through the use of a multivariate algorithm [19]. In μ+jets events, upper limits are required on the transverse mass of the reconstructed W boson [20] of $M_T^W < 250\,\mathrm{GeV}$ and $\not{p}_\mathrm{T} < 250\,\mathrm{GeV}$ to remove events with misreconstructed muon p_T. Additional selections are applied to reduce backgrounds in muon events, and to suppress contributions from multijet production. A detailed description of these requirements can be found in Ref. [21]. In addition, we require the curvature of the track associated with the lepton to be well measured to reduce lepton charge misidentification.

III. SIGNAL AND BACKGROUND SAMPLES

We simulate $t\bar{t}$ events at the next-to-leading-order (NLO) in perturbative QCD with the MC@NLO event generator version 3.4 [22] and at the leading-order (LO) with ALPGEN event generator version 2.11 [23]. Parton showering, hadronization, and modeling of the underlying event are performed with HERWIG [24] for MC@NLO events and with PYTHIA 6.4 [25] for ALPGEN events. The detector response is simulated using GEANT3 [26]. To model the effects of multiple $p\bar{p}$ interactions, the MC events are overlaid with events from random $p\bar{p}$ collisions with the same luminosity distribution as the data. The main background to the $t\bar{t}$ signal is W+jets events, where the W boson is produced via the electroweak interaction together with additional partons from QCD radiation. The W+jets final state can be split into four subsamples according to parton flavor, $Wb\bar{b}$ + jets, $Wc\bar{c}$ + jets, Wc+jets, and W+light jets, where light refers to gluons, u, d, or s quarks. The W+jets background is modeled with ALPGEN and PYTHIA [23, 25], as is the background from Z+jets events. Other background processes include WW, WZ, and ZZ diboson productions simulated using PYTHIA, and single top quark electroweak production simulated using COMPHEP [27]. The multijet background, where a jet is misidentified as an isolated lepton, is estimated from the data using the matrix method [21, 28]. We use six different BSM models [29] to study modified $t\bar{t}$ production: one Z' boson model and five axigluon models with different axigluon masses and couplings (m200R, m200L, m200A, m2000R, and m2000A, where L, R, and A refer to left-handed, right-handed, and axial couplings, and numbers are the particle masses in GeV). Some additional axigluon models such as m2000L are not simulated as they are excluded by other measurements of top quark properties. The BSM events are generated with LO MADGRAPH 5 [30] interfaced to PYTHIA

for parton evolution.

IV. ANALYSIS METHOD

A constrained kinematic χ^2 fit is used to associate the observed leptons and jets with the individual top quarks using a likelihood term for each jet-to-quark assignment, as described in Ref. [31]. We assume the four jets with largest p_T to originate from $t\bar{t}$ decay in events with more than four jets. The algorithm includes a technique that reconstructs events with a lepton and only three jets [32]. The addition of the three-jet sample almost doubles the signal sample as shown in Table I. In our analysis, all possible assignments of jets to final state quarks are considered and weighted by the χ^2 probability of each kinematic fit and by the b tagging probability.

To determine the sample composition, we construct a kinematic discriminant based on the approximate likelihood ratio of expectations for $t\bar{t}$ and W+jets events [33]. The input variables are chosen to achieve good separation between $t\bar{t}$ and W+jets events, and required to be well modeled and not strongly correlated with one another or with the lepton polar angles used in the measurement. Sets of input variables are selected independently for the ℓ+3 jet and the $\ell+\geq 4$ jet events, each in three subchannels according to the number of b tagged jets: 0, 1, ≥ 2. The channels without b tagged jets are used to determine the sample composition and background calibration, not to measure the polarization.

The input variables used for the ℓ+3 jet kinematic discriminant are $k_T^{min}= \min(p_{T,a}, p_{T,b}) \cdot \Delta R_{ab}$, where $\Delta R_{ab} = \sqrt{(\eta_a - \eta_b)^2 + (\phi_a - \phi_b)^2}$ is the angular distance between the two closest jets (a and b), $\min(p_{T,a}, p_{T,b})$ represents the smaller transverse momentum of the two jets, and the ϕ are their azimuths in radians; aplanarity $A = 3/2\lambda_3$, where λ_3 is the smallest eigenvalue of the normalized momentum tensor; H_T^ℓ, which is the scalar sum of the p_T of the jets and lepton; ΔR between the leading jet and the next-to-leading jet; and ΔR between the lepton and the leading jet.

The input variables for the $\ell+\geq 4$ jet discriminant are k_T^{min}; aplanarity; H_T^ℓ; centrality, $C = H_T/H$, where H_T is the scalar sum of all jet p_T values and H is the scalar sum of all jet energies; the lowest χ^2 among the different kinematic fit solutions in each event; $(p_T^{b_{\rm had}} - p_T^{b_{\rm lep}})/(p_T^{b_{\rm had}} + p_T^{b_{\rm lep}})$, the relative p_T difference between $b_{\rm lep}$, the b jet candidate from the $t \to b\ell\nu$ decay, and $b_{\rm had}$, the b jet candidate from the $t \to bqq'$ decay; and m_{jj}, the invariant mass of the two jets corresponding to the $W \to q\bar{q}'$ decay.

The sample composition is determined from a simultaneous maximum-likelihood fit to the kinematic discriminant distributions. The W+jets background is normalized separately for the heavy-flavor contribution ($Wb\bar{b}$ + jets and $Wc\bar{c}$ + jets) and for the light-parton contribution (Wc + jets and W+light jets). The sample composition after implementing the selections, and fitting the maximum likelihood to data, is broken down into individual channels by lepton flavor and number of jets, and summarized in Table I. The obtained $t\bar{t}$ yield is close to the expectations.

	3 jets		≥ 4 jets	
Source	e+jets	μ+jets	e+jets	μ+jets
W+jets	1741 ± 26	1567 ± 15	339 ± 3	295 ± 3
Multijet	494 ± 7	128 ± 3	147 ± 4	49 ± 2
Other Bkg	446 ± 5	378 ± 2	87 ± 1	73 ± 1
$t\bar{t}$ signal	1200 ± 25	817 ± 20	1137 ± 24	904 ± 23
Sum	3881 ± 37	2890 ± 25	1710 ± 25	1321 ± 23
Data	3872	2901	1719	1352

TABLE I: Sample composition and event yields after implementing the selection requirements and the maximum-likelihood fit to kinematic distributions in data. Only statistical uncertainties are shown.

The lepton angular distributions in W+jets events must be well modeled since these events form the leading background, especially in the ℓ+3 jet sample. We therefore use a control sample of ℓ+3 jet events without b tagged jets, as such events are dominated by W+jets production with $> 70\%$ contribution. This sample is not used for the polarization measurement. We reweight the W+jets MC events so that the $\cos\theta_{\ell,\hat{n}}$ distributions agree with those for the control events in data with $t\bar{t}$ and other background components subtracted. We use the relative polarization asymmetry defined as $[N_j(\cos\theta_{l,\hat{n}}) - N_{-j}(\cos\theta_{l,\hat{n}})]/[N_j(\cos\theta_{l,\hat{n}}) + N_{-j}(\cos\theta_{l,\hat{n}})]$, where j refers to bins of $\cos\theta_{\ell,\hat{n}}$ values between 0 and 1 and $-j$ refers to bins between -1 and 0. The distributions of simulated W+jets events and subtracted data are shown in Fig. 1. The correction to MC obtained from the control sample is applied to the background templates used in our signal extraction. The corrections are 0.047 ± 0.002 for polarization along the beam axis, 0.011 ± 0.001 for the transverse axis, and a negligible amount for the helicity axis. The uncertainties are propagated to the measurement as a systematic uncertainty of the background modeling. We observe the W+jets events to have polarization, calculated as in Eq. (2), of $+0.18$ along the beam axis, -0.23 along the helicity axis, and -0.02 along the transverse axis. Other backgrounds give polarizations of $+0.05$ (beam axis), -0.30 (helicity axis), and $+0.01$ (transverse axis).

To measure the polarization, a fit is performed to the reconstructed $\cos\theta_{\ell,\hat{n}}$ distribution using $t\bar{t}$ templates of $+1$ and -1 polarizations, and background templates normalized to the expected event yield. The signal templates arise from the $t\bar{t}$ MC sample generated with no polarization but reweighted to follow the expected double differential distribution [2],

$$\frac{1}{\Gamma}\frac{d\Gamma}{d\cos\theta_1 \cos\theta_2} = \frac{1}{4}(1 + \kappa_1 P_{\hat{n},1}\cos\theta_1 + \\ + \rho\kappa_2 P_{\hat{n},2}\cos\theta_2 - \kappa_1\kappa_2 C\cos\theta_1\cos\theta_2), \quad (3)$$

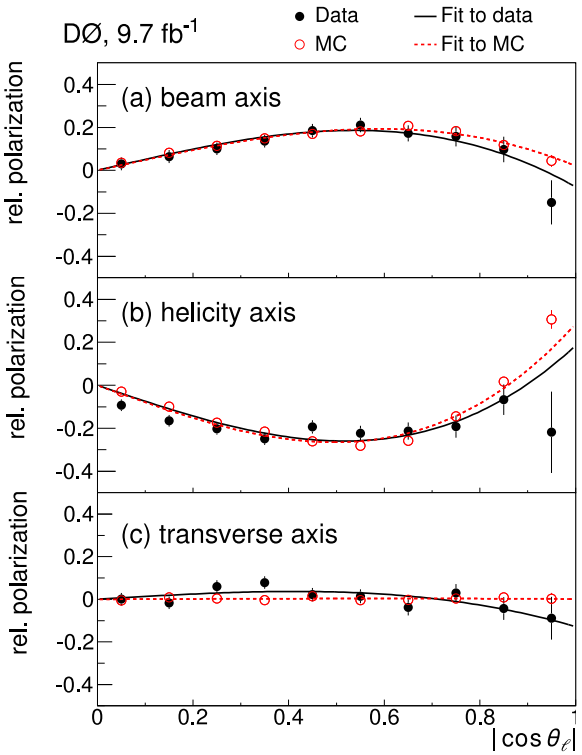

FIG. 1: The simulated W+jets events before correction and data with $t\bar{t}$ and other than W+jets background components subtracted compared in $\cos\theta_{\ell,\hat{n}}$ distributions in the ℓ+3 jet and no b tagged jet control sample.

where indices 1 and 2 represent the t and $\bar{t}$ quark decay products (the leptons and down quarks, or their charge conjugates), κ is the spin-analyzing power, and C is the $t\bar{t}$ spin correlation coefficient for a given quantization axis. We use the SM values $C = -0.368$ (helicity axis) and $C = 0.791$ (beam axis), both calculated at NLO in QCD and in electroweak couplings in Ref. [2]. The spin correlation factor is not known for the transverse axis, and thus we set $C = 0$ and assign a systematic uncertainty by varying the choice of this factor. The $P_{\hat{n},i}$ represents the polarization state we model (here $P_{\hat{n},i} = \pm 1$) along the chosen axis $\hat{n}$. In the SM, assuming CP invariance, $P_{\hat{n},1} = P_{\hat{n},2}$ and gives the relative sign factor ρ a value of $+1$ for the helicity axis and -1 for the beam and transverse axes [2].

A simultaneous fit is performed for the eight samples defined according to lepton flavor (e or μ), lepton charge, and number of jets (3 or ≥ 4). The observed polarization is taken as $P = f_+ - f_-$, where $f_\pm$ are the fraction of events with $P = +1$ and -1 returned from the fit. The fitting procedure and methodological approach are verified using pseudoexperiments for five values of polarization, and through a check of consistency with predictions, using the BSM models with nonzero generated longitudinal polarizations. The fitted polarizations and the model inputs are in good agreement, as shown in Fig. 2 for the polarizations along the beam axis, thus verifying our template methodology. The distributions in the cosine of the polar angle of leptons from $t\bar{t}$ decay for all three axes are shown in Fig. 3.

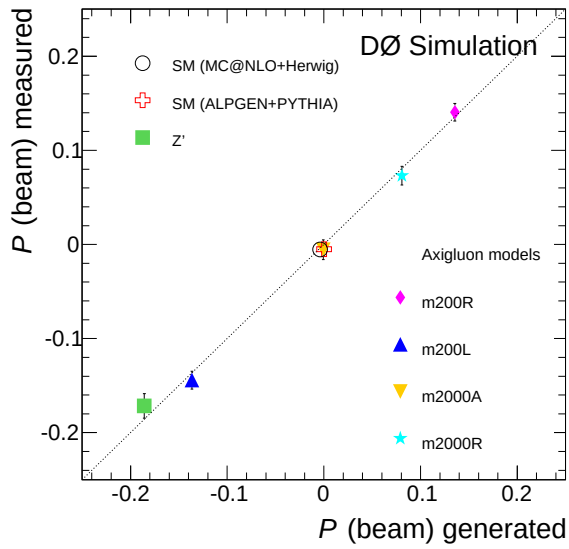

FIG. 2: Comparison of measured and generated polarizations along the beam axis for the SM and several non-SM models. The uncertainties are statistical.

A previous measurement of top quark polarization and the forward-backward t and $\bar{t}$ asymmetry in dilepton final states [7] noted a correlation between these two measurements. This correlation is caused by acceptance and resolution effects in the kinematic reconstruction of the events. We determine the dependence of the observed polarization on the forward-backward asymmetry at the parton level, $A_{\rm FB}$, using samples in which the t and $\bar{t}$ rapidity distributions are reweighted to accommodate the polarizations. We then use a correction for the difference between the nominal MC@NLO production-level $A_{\rm FB}$ of $(5.01 \pm 0.03)\%$ and the next-to-next-to-leading-order (NNLO) calculation [34] of $(9.5 \pm 0.7)\%$. The observed correction is -0.030 for the polarization along the beam axis, less than 0.002 for the polarization along the helicity axis, and is negligible for the transverse polarization. The uncertainty on the expected $A_{\rm FB}$ is propagated to the measurement as part of the methodology systematic uncertainty.

V. SYSTEMATIC UNCERTAINTIES

We have evaluated several categories of systematic uncertainties using fully simulated events: uncertainties associated with jet reconstruction, jet energy measurement, b tagging, the modeling of background and signal events, PDFs, and procedures and assumptions made in the analysis. The sources of systematic uncertainties and their

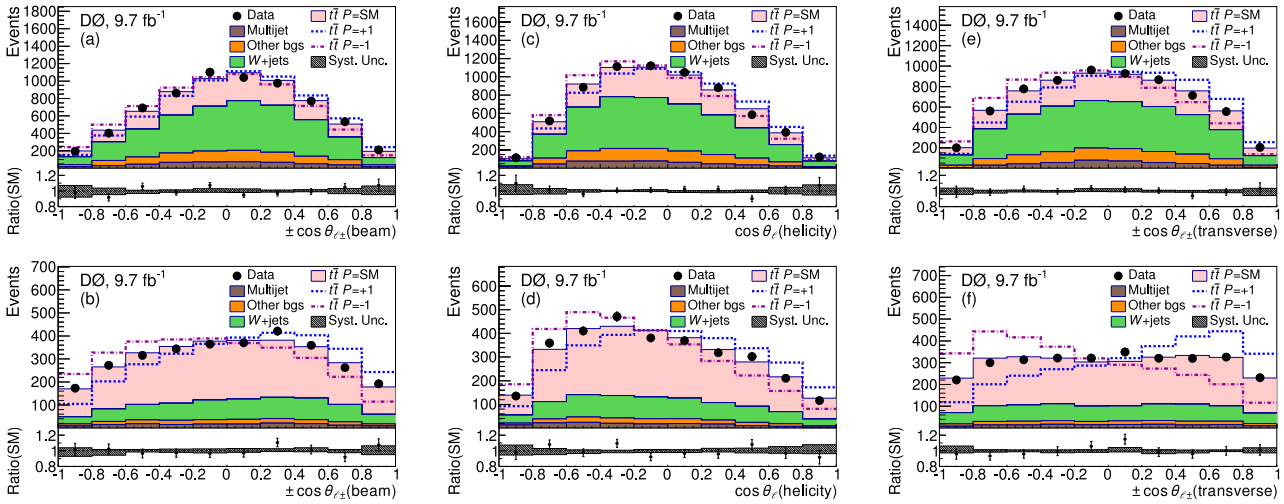

FIG. 3: The combined e+jets and μ+jets $\cos\theta$ distributions for data, expected backgrounds, and signal templates for $P = -1$, SM, and $+1$. Panels (a), (c), and (e) show ℓ+3 jet events; (b), (d), and (f) show $\ell+ \geq 4$ jet events; (a) and (b) show distributions relative to the beam axis; (c) and (d) show distributions relative to the helicity axis; and (e) and (f) show distributions relative to the transverse axis. The hashed areas represent systematic uncertainties. The direction of the $\cos\theta$ axis is reversed for the ℓ^- events for beam and transverse spin-quantization axes plots.

contributions are listed in Table II and added in quadrature for the total uncertainty. Details about the evaluation of the uncertainties can be found in Refs. [21, 31]. Additionally, we assign an uncertainty in modeling the invariant mass of the $t\bar{t}$ system ($m_{t\bar{t}}$) based on the difference in $m_{t\bar{t}}$ distributions in our signal MC and the NNLO predictions [35].

Source	Beam	Helicity	Transverse
Jet reconstruction	±0.010	±0.008	±0.008
Jet energy measurement	±0.010	±0.023	±0.006
b tagging	±0.009	±0.014	±0.005
Background modeling	±0.007	±0.021	±0.004
Signal modeling	±0.016	±0.020	±0.008
PDFs	±0.013	±0.011	±0.003
Methodology	±0.013	±0.007	±0.009
Total systematic uncertainty	±0.030	±0.042	±0.017
Statistical uncertainty	±0.046	±0.044	±0.030
Total uncertainty	±0.055	±0.061	±0.035

TABLE II: Summary of the uncertainties in the measured top quark polarization along three axes. The systematic uncertainty source indicates the difference in polarization when the measurement is repeated using alternative modeling, after applying uncertainties from the employed methods, or from assumptions made in the measurement. The uncertainties are added in quadrature to form groups of systematic sources and the total uncertainty.

VI. RESULTS

The measured polarizations for the three spin-quantization axes are shown in Table III. Results on the longitudinal polarizations are presented in Fig. 4 and compared to SM predictions and several of the BSM models discussed previously. The measurement along the beam axis is consistent with the previous D0 result in the dilepton channel [7], $P = 0.113 \pm 0.093$. We estimate the correlation between this result for the beam axis and that of Ref. [7] to be 5%. The combination using the method of Refs. [36, 37] yields a top quark polarization along the beam axis $P = 0.081 \pm 0.048$.

Axis	Measured polarization	SM prediction
Beam	$+0.070 \pm 0.055$	-0.002
Beam - D0 comb.	$+0.081 \pm 0.048$	-0.002
Helicity	-0.102 ± 0.061	-0.004
Transverse	$+0.040 \pm 0.035$	$+0.011$

TABLE III: Measured top quark polarization from the $t\bar{t}$ ℓ+jet channel along the beam, helicity, and transverse axes, and the combined polarization for beam axis with the dilepton result by the D0 Collaboration denoted as *Beam - D0 comb.*. The total uncertainties are obtained by adding the statistical and systematic uncertainties in quadrature.

VII. CONCLUSION

In summary, we measure the top quark polarization for $t\bar{t}$ production in $p\bar{p}$ collisions at $\sqrt{s} = 1.96$ TeV along sev-

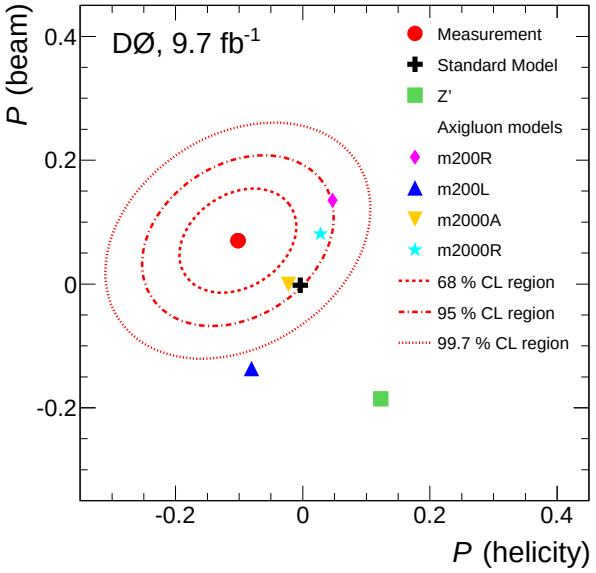

FIG. 4: Two-dimensional visualization of the longitudinal top quark polarizations in the ℓ+jets channel measured along the beam and helicity axes compared with the SM and the BSM models described in the text. In this case, the m200A model is not shown as it is indistinguishable from m2000A model. The correlation of the two measurement uncertainties is 27%.

eral spin-quantization axes. The polarizations are consistent with SM predictions. The transverse polarization is measured for the first time. These are the most precise measurements of top quark polarization in $p\bar{p}$ collisions.

VIII. ACKNOWLEDGMENTS

We express our appreciation to Helen Edwards for her role in designing and building the Tevatron, and her oversight of the D0 detector project in its early days. We thank R. M. Godbole and W. Bernreuther for enlightening discussions. We thank the staffs at Fermilab and collaborating institutions, and acknowledge support from the Department of Energy and National Science Foundation (USA); Alternative Energies and Atomic Energy Commission and National Center for Scientific Research/National Institute of Nuclear and Particle Physics (France); Ministry of Education and Science of the Russian Federation, National Research Center "Kurchatov Institute" of the Russian Federation, and Russian Foundation for Basic Research (Russia); National Council for the Development of Science and Technology and Carlos Chagas Filho Foundation for the Support of Research in the State of Rio de Janeiro (Brazil); Department of Atomic Energy and Department of Science and Technology (India); Administrative Department of Science, Technology and Innovation (Colombia); National Council of Science and Technology (Mexico); National Research Foundation of Korea (Korea); Foundation for Fundamental Research on Matter (Netherlands); Science and Technology Facilities Council and The Royal Society (United Kingdom); Ministry of Education, Youth and Sports (Czech Republic); Bundesministerium für Bildung und Forschung (Federal Ministry of Education and Research) and Deutsche Forschungsgemeinschaft (German Research Foundation) (Germany); Science Foundation Ireland (Ireland); Swedish Research Council (Sweden); China Academy of Sciences and National Natural Science Foundation of China (China); and Ministry of Education and Science of Ukraine (Ukraine).

[1] S. Fajfer, J. F. Kamenik and B. Melic, *Discerning New Physics in Top-Antitop Production using Top Spin Observables at Hadron Colliders*, J. High Energy Phys. 08 (2012) 114.

[2] W. Bernreuther and Z.-G. Si, *Distributions and correlations for top quark pair production and decay at the Tevatron and LHC*, Nucl. Phys. **B837**, 90 (2010).

[3] A. Brandenburg, Z.-G. Si and P. Uwer, *QCD corrected spin analyzing power of jets in decays of polarized top quarks*, Phys. Lett. B **539**, 235 (2002).

[4] W. Bernreuther, A. Brandenburg and P. Uwer, *Transverse polarization of top quark pairs at the Tevatron and the large hadron collider*, Phys. Lett. B **368**, 153 (1996).

[5] M. Baumgart and B. Tweedie, *Transverse Top Quark Polarization and the $t\bar{t}$ Forward-Backward Asymmetry*, J. High Energy Phys. 08 (2013) 072.

[6] V. M. Abazov *et al.* (D0 Collaboration), *Measurement of Leptonic Asymmetries and Top Quark Polarization in $t\bar{t}$ Production*, Phys. Rev. D **87**, 011103 (2013).

[7] V. M. Abazov *et al.* (D0 Collaboration), *Simultaneous Measurement of Forward-Backward Asymmetry and Top Polarization in Dilepton Final States from $t\bar{t}$ Production at the Tevatron*, Phys. Rev. D **92**, 052007 (2015).

[8] G. Aad *et al.* (ATLAS Collaboration), *Measurement of Top Quark Polarization in Top-Antitop Events from Proton-Proton Collisions at $\sqrt{s}$ = 7 TeV Using the ATLAS Detector*, Phys. Rev. Lett. **111**, 232002 (2013).

[9] S. Chatrchyan *et al.* (CMS Collaboration), *Measurements of $t\bar{t}$ spin correlations and top-quark polarization using dilepton final states in pp collisions at $\sqrt{s}$ = 7 TeV*, Phys. Rev. Lett. **112**, 182001 (2014); V. Khachatryan *et al.* (CMS Collaboration), *Measurements of $t\bar{t}$ spin correlations and top quark polarization using dilepton final states in pp collisions at $\sqrt{s}$ = 8 TeV*, Phys. Rev. D **93**,

052007 (2016).

[10] J. A. Aguilar-Saavedra, *Portrait of a colour octet*, J. High Energy Phys. 08 (2014) 172; J. A. Aguilar-Saavedra, in Proceedings of the 7th International Workshop on Top Quark Physics, Cannes, France, 2014 (unpublished).

[11] D. Choudhury, R. M. Godbole, S. D. Rindani and P. Saha, *Top polarization, forward-backward asymmetry and new physics*, Phys. Rev. D **84**, 014023 (2011).

[12] W. Bernreuther, M. Fücker and Z.-G. Si, *Weak interaction corrections to hadronic top quark pair production: Contributions from quark-gluon and b anti-b induced reactions*, Phys. Rev. D **78**, 017503 (2008); W. Bernreuther and Z.-G. Si (private communication).

[13] V. M. Abazov *et al.* (D0 Collaboration), *The Upgraded D0 Detector*, Nucl. Instrum. Methods Phys. Res. Sec. A **565**, 463 (2006); R. Angstadt *et al.*, *The layer 0 inner silicon detector of the D0 experiment*, Nucl. Instrum. Methods Phys. Res., Sect. A **622**, 298 (2010); V. M. Abazov *et al.* (D0 Collaboration), *The muon system of the Run II D0 detector*, Nucl. Instrum. Methods Phys. Res., Sect. A **552**, 372 (2005).

[14] V. M. Abazov *et al.* (D0 Collaboration), *Electron and Photon Identification in the D0 Experiment*, Nucl. Instrum. Methods Phys. Res., Sect. A **750**, 78 (2014).

[15] V. M. Abazov *et al.* (D0 Collaboration), *Muon reconstruction and identification with the Run II D0 detector*, Nucl. Instrum. Methods Phys. Res., Sect. A **737**, 281 (2014).

[16] The pseudorapidity is defined as $\eta = -\ln[\tan(\theta/2)]$, where θ is the measured polar angle of an object.

[17] G. C. Blazey *et al.*, hep-ex/0005012.

[18] V. M. Abazov *et al.* (D0 Collaboration), *Jet energy scale determination in the D0 experiment*, Nucl. Instrum. Methods Phys. Res., Sect. A **763**, 442 (2014).

[19] V. M. Abazov *et al.* (D0 Collaboration), *Improved b quark jet identification at the D0 experiment*, Nucl. Instrum. Methods Phys. Res., Sect. A **763**, 290 (2014).

[20] J. Smith, W. L. van Neerven and J. A. M. Vermaseren, *The Transverse Mass and Width of the W Boson*, Phys. Rev. Lett. **50**, 1738 (1983).

[21] V. M. Abazov *et al.* (D0 Collaboration), *Measurement of differential $t\bar{t}$ production cross sections in $p\bar{p}$ collisions*, Phys. Rev. D **90**, 092006 (2014).

[22] S. Frixione and B. R. Webber, *Matching NLO QCD computations and parton shower simulations*, J. High Energy Phys. 06 (2002) 029; S. Frixione, P. Nason, and B. R. Webber, *Matching NLO QCD and parton showers in heavy flavour production*, J. High Energy Phys. 08 (2003) 007.

[23] M. L. Mangano, M. Moretti, F. Piccinini, R. Pittau and A. D. Polosa, ALPGEN*, a generator for hard multiparton processes in hadronic collisions*, J. High Energy Phys. 07 (2003) 001.

[24] G. Corcella, I. G. Knowles, G. Marchesini, S. Moretti, K. Odagiri, P. Richardson, M. H. Seymour, and B. R. Webber, HERWIG *6: An Event generator for hadron emission reactions with interfering gluons (including supersymmetric processes)*, J. High Energy Phys. 01 (2001) 010.

[25] T. Sjøstrand, S. Mrenna, and P. Skands, PYTHIA *6.4 physics and manual*, J. High Energy Phys. 05 (2006) 026.

[26] R. Brun and F. Carminati, Geant: Detector description and simulation tool, CERN Program Library Long Writeup W5013 (1993) (unpublished).

[27] E. Boos, V. Bunichev, M. Dubinin, L. Dudko, V. Edneral, V. Ilyin, A. Kryukov, V. Savrin, A. Semenov, and A. Sherstnev (CompHEP Collaboration), *CompHEP 4.4: Automatic computations from Lagrangians to events*, Nucl. Instrum. Methods Phys. Res., Sect. A **534**, 250 (2004).

[28] V. M. Abazov *et al.* (D0 Collaboration), *Measurement of the $t\bar{t}$ production cross section in $p\bar{p}$ collisions at $\sqrt{s}$ =* 1.96 TeV *using secondary vertex b tagging*, Phys. Rev. D **74**, 112004 (2006).

[29] A. Carmona, M. Chala, A. Falkowski, S. Khatibi, M. M. Najafabadi, G. Perez, and J. Santiago, *From Tevatron's top and lepton-based asymmetries to the LHC*, J. High Energy Phys. 07 (2014) 005.

[30] J. Alwall, R. Frederix, S. Frixione, V. Hirschi, F. Maltoni, O. Mattelaer, H.-S. Shao, T. Stelzer, P. Torrielli, and M. Zaro, *The automated computation of tree-level and next-to-leading order differential cross sections, and their matching to parton shower simulations*, J. High Energy Phys. 07 (2014) 079.

[31] V. M. Abazov *et al.* (D0 Collaboration), *Measurement of the forward-backward asymmetry in top quark-antiquark production in $p\bar{p}$ collisions using the lepton+jets channel*, Phys. Rev. D **90**, 072011 (2014).

[32] R. Demina, A. Harel and D. Orbaker, *Reconstructing $t\bar{t}$ events with one lost jet*, Nucl. Instrum. Methods Phys. Res., Sect. A **788**, 128 (2015).

[33] V. M. Abazov *et al.* (D0 Collaboration), *Measurement of the $t\bar{t}$ production cross section in $p\bar{p}$ collisions at $\sqrt{s}$=1.96 TeV using kinematic characteristics of lepton + jets events*, Phys. Rev. D **76**, 092007 (2007).

[34] M. Czakon, P. Fiedler and A. Mitov, *Resolving the Tevatron Top Quark Forward-Backward Asymmetry Puzzle: Fully Differential Next-to-Next-to-Leading-Order Calculation*, Phys. Rev. Lett. **115**, 052001 (2015).

[35] M. Czakon, P. Fiedler, D. Heymes and A. Mitov, *NNLO QCD predictions for fully-differential top-quark pair production at the Tevatron*, J. High Energy Phys. 05 (2016) 034.

[36] L. Lyons, D. Gibaut and P. Clifford, *How to Combine Correlated Estimates of a Single Physical Quantity*, Nucl. Instrum. Methods Phys. Res., Sect. A **270**, 110 (1988).

[37] A. Valassi, *Combining correlated measurements of several different physical quantities*, Nucl. Instrum. Methods Phys. Res., Sect. A **500**, 391 (2003).